Structural Characterization and Impedance Spectroscopy of Substituted, Fused-Ring Organic Semiconductors

by

Charles Michael Shaw

A dissertation submitted in partial fulfillment
of the requirements for the degree of
Doctor of Philosophy
(Macromolecular Science and Engineering)
in The University of Michigan
2011

Doctoral Committee:

Professor David C. Martin, Co-Chair
Professor Adam J. Matzger, Co-Chair
Professor L. Jay Guo
Associate Professor Max Shtein

© Charles Michael Shaw 2011
All Rights Reserved

In memory of my grandfathers: George, James and Wayne

ACKNOWLEDGEMENTS

I wish to first acknowledge my thesis adviser, David C. Martin, for his years of teaching, guidance and discussions essential to my graduate work. I also thank the rest of my committee—professors Adam J. Mazger, L. Jay Guo and Max Shtein—for their valuable feedback and constructive criticism.

I gratefully acknowledge the assistance of Conan Weiland, Jeff Hendricks, Sarah Spanninga, Arthur Lee-Feldman, Joe Elliott, Jihua Chen, Katie Feldman, Bakhtyar Ali, Roy Miller, Brett Guralnick and Jinglin Liu for their contributions numerous and varied. I must especially thank Laura Povlich for her myriad contributions—nearly as numerous and varied as my own—to the work contained herein.

The research groups of Adam Matzger at the University of Michigan and Anton Jákli at Kent State University deserve special mention. Many thanks to Xinnan Zhang and Lidaris San Miguel Rivera, Antek Wong-Foy, William Porter and Geetha Nair.

I would also like to thank George Hebert and Twitter for teaching me to say more with less. Also John Roos and the Gerstacker Basement Coffee Club for keeping me awake through it all.

To my family—Mom, Dad, Wheezer, Smallz and Grandma (both of you)—my sincerest thanks for your many years of support and encouragement. And to my wonderful wife, Stephanie: I couldn't have done it without you.

TABLE OF CONTENTS

DEDICATION ii

ACKNOWLEDGEMENTS iii

LIST OF FIGURES viii

LIST OF TABLES xv

LIST OF APPENDICES xvi

LIST OF ABBREVIATIONS xvii

ABSTRACT xix

CHAPTER

I. Introduction 1

1.1 The Modern Transistor 1
1.2 Structure and Performance for Organic TFTs 2
1.3 Liquid Crystals 3
1.4 The Interface Layer 4
1.5 Thienoacenes 6
1.6 Dissertation Outline 8

II. Crystal and Thin-Film Structure of Alkyl-Substituted Pentathienoacenes 10

2.1 Introduction 10
2.1.1 Chapter Overview 11
2.2 Results & Discussion 11
2.2.1 Crystal Structure 11
2.2.2 Thin Films 16
2.3 Conclusions 21
2.4 Materials & Methods 23

2.4.1 Materials 23
2.4.2 Powder X-ray Diffraction 24
2.4.3 Unit Cell Parameter Determination 24
2.4.4 Molecular Modeling 25
2.4.5 Thin Film Deposition 26
2.4.6 Optical Microscopy 26
2.4.7 Scanning Electron Microscopy 27
2.4.8 Thin Film X-ray Diffraction 27
2.4.9 Electron Diffraction 27
2.5 Acknowledgements 27

III. Thermotropic Phase Transitions of Alkyl-Substituted Pentathienoacenes 28

3.1 Introduction 28
3.1.1 Chapter Overview 29
3.2 Results & Discussion 30
3.2.1 Liquid Crystal Texture Identification 30
3.2.2 Ferroelectricty 31
3.2.3 C12 High Temperature Crystallography 31
3.2.4 C8 High Temperature Crystallography 35
3.2.5 Solid State Roughening Transition 38
3.2.6 Annealing 39
3.3 Conclusions 44
3.4 Materials & Methods 47
3.4.1 Materials 47
3.4.2 Liquid Crystal ID *via* Variable Temperature Polarized Optical Microscopy 47
3.4.3 Ferroelectricity 48
3.4.4 Variable Temperature X-ray Diffraction 48
3.4.5 Side-Chain Melting *via* Variable Temperature Polarized Optical Microscopy 49
3.4.6 Scanning Electron Microscopy 49
3.5 Acknowledgements 50

IV. Electron Flux Induced Phase Transitions of Alkyl-Substituted Pentathienoacenes 51

4.1 Introduction 51
4.1.1 Critical Dose 53
4.1.2 Chapter Overview 53
4.2 Results & Discussion 54
4.2.1 Dynamic Diffraction of C8 54
4.2.2 Dynamic Diffraction of C12 63
4.3 Conclusions 65

4.4 Materials & Methods 66
4.4.1 Materials 66
4.4.2 Film Casting 66
4.4.3 Collection of Diffraction Patterns 67
4.4.4 Analysis of Diffraction Patterns 67
4.5 Acknowledgements 68

V. Impedance Spectroscopy of Triisopropylsilyl Pentacene Thin Film Transistors 69

5.1 Introduction 69
5.1.1 Chapter Overview 71
5.2 Results & Discussion 72
5.2.1 Optical Crystallography 72
5.2.2 DC Operating Characteristics 73
5.2.3 AC Operating Characteristics 74
5.2.4 Equivalent Circuit Modeling 78
5.2.5 Implications for Transport 80
5.2.6 DC Mobility From Impedance Data 82
5.3 Conclusions 83
5.4 Materials & Methods 84
5.4.1 Materials 84
5.4.2 Substrates 85
5.4.3 Film Deposition 85
5.4.4 Optical Microscopy 86
5.4.5 Electronic Testing 86
5.4.6 DC Operating Characteristics 87
5.4.7 AC Operating Characteristics 87
5.4.8 Impedance Analysis 88
5.5 Acknowledgements 89

VI. Impedance Spectroscopy of Poly(2,5-bis(3-alkylthiophen-2-yl)thieno[3,2-b]thiophene) Thin Film Transistors 90

6.1 Introduction 90
6.1.1 Chapter Overview 91
6.2 Results & Discussion 92
6.2.1 Film Structure 92
6.2.2 DC & AC Operating Characteristics 92
6.2.3 Variable-Temperature AC Operating Characteristics of Doped PBTTT 95
6.2.4 Variable Temperature Impedance Spectroscopy of Annealed PBTTT 100
6.3 Conclusions 104
6.4 Materials & Methods 105

6.4.1 Materials . . . 105
6.4.2 Substrates . . . 105
6.4.3 Polymer Deposition . . . 106
6.4.4 X-ray Diffraction . . . 106
6.4.5 Electronic Testing . . . 107
6.4.6 Operating Characteristics . . . 107
6.4.7 Variable Temperature Impedance Spectroscopy . . . 108
6.4.8 Impedance Analysis . . . 109
6.5 Acknowledgements . . . 110

VII. Conclusions and Future Directions . . . 111

7.1 Results of Work . . . 111
7.1.1 Crystal Structure and Thin Film Morphology of Alkyl-Substituted Thienoacenes . . . 111
7.1.2 Thermal Transitions of Substituted Thienoacenes . . . 112
7.1.3 Electron-Beam Induced Transitions in Substituted Thienoacenes . . . 113
7.1.4 Impedance Spectroscopy of TIPS-Pentacene Thin Film Transistors . . . 114
7.1.5 Variable Temperature Impedance Spectroscopy of PBTTT Thin Film Transistors . . . 115
7.2 Possible Future Directions . . . 116
7.2.1 Substituted Thienoacene Thin Film Transistors . . . 116
7.2.2 Electron Flux Induced Phase Transition . . . 116
7.2.3 Extended Range Impedance Spectroscopy . . . 116

APPENDICES . . . 118

BIBLIOGRAPHY . . . 123

LIST OF FIGURES

Figure

1.1 T5 combines the chemical stability gains of thiophene over acene rings while maintaining the rigid planarity of Pn 7

1.2 T5 substituted with solubilizing alkyl groups. R = C_8H_{17} or $C_{12}H_{25}$. 7

2.1 Atomic positions of C8 molecules predicted by molecular modeling inside unit cells determined from powder XRD. View directions are [010] (left) and [100] (right) 13

2.2 Atomic positions of C12 molecules predicted by molecular modeling inside unit cells determined from powder XRD. View directions are [010] (left) and [100] (right) 14

2.3 Simulated C8 (top) and C12 (bottom) unit cells as viewed on [001]. Alkyl substitutions hidden to permit view of T5 cores. T5 cores lie essentially parallel to (210) in C8 and ($2\bar{1}0$) in C12, as indicated by red lattice planes in these figures. π-stacking is thus along [210] for C8 and [$2\bar{1}0$] for C12. 15

2.4 POM of C8 films grown from 0.1% by weight solutions in toluene. All films grown at room temperature. Films grown with quick (≈30 minutes) evaporation (top) show small crystals with poorly realized needle and tablet habit. Films with slow (≈8 hours) evaporation (middle) showing large crystals and both habits. Large but rough crystals of both habits from suspension crystallization (bottom). 17

2.5 SEM of slowly grown C8 crystals showing slow growth in [001]. . . . 18

2.6 Thin film XRD of C8 films. All films grown at room temperature. Quickly grown films (upper left) showing strong texturing of ($00l$) parallel to substrate despite fast solvent evaporation. Slowly grown, needle habit crystals (upper right) showing rotation of crystal stacks. Suspension crystallized needles (lower left) showing very strong texturing. Miller indices for observed spots (lower right) 20

2.7 POM and XRD of slowly grown C12 thin films. POM of C12 showing tabular habit and large crystal size (left) and XRD showing strong texturing of ($00l$) parallel to the substrate (right). 22

2.8 Representative ED patterns of a) C8 and b) C12 thin films exhibiting the same strong texturing observed *via* XRD. Zone axis for both patterns is nominally [001] 22

3.1 C8 exhibiting the fan texture (left) in a planar alignment cell and Schlieren texture (right) in a homeotropic alignment cell. The combination of these two textures identify this phase as smectic C . . . 30

3.2 C12 exhibiting the Schlieren texture in a cell with untreated glass. Disclinations of strength $|S| = 1$ exclusively are observed, identifying this phase as smectic C. 31

3.3 Polarization of C8 in the smectic C phase (left) in planar alignment and as an isotropic melt (right). Both show only molecular polarization response and no indication of ferroelectricity, consistent with the smectic C identification. 32

3.4 VT-XRD of C12 at room temperature (upper left) with $c = 3.89$ nm, at 95°C (upper right) after the "side chain melting" transition with c reduced by 22.9%, and at 160 °C (lower-left) in the smectic C phase with 3.20 nm layer spacing 33

3.5 VT-XRD of C8 at room temperature (upper left) exhibiting the room temperature and frozen-in elevated temperature phase, at 85 °C (upper right) after the "side chain melting" transition and loss of the room temperature phase and at 174 °C (lower left) in the smectic C phase with 2.63 nm layer spacing 36

3.6 1D VT-XRD of C8 before and after the "side chain melting" transition. The peaks corresponding to ($00l$)s reported in Chapter II all decrease in intensity above the transition temperature, while the intensity of the other peaks—the high temperature ($00l$)s—increase above this temperature 37

3.7 VT-POM of C8 crystals before (top) and after (bottom) macroscopic roughening induced by the unit cell contraction at 85 °C. 40

3.8 VT-POM of C12 crystals before (left) and after (right) macroscopic roughening induced by the unit cell contraction at 95 °C. 41

3.9 SEM of C8 crystals before (left) and after (right) macroscopic roughening induced by the unit cell contraction at 85 °C. 41

3.10 VT-POM of C8 showing the development of large cracks after cooling through the full phase sequence. 43

3.11 When interdigitated substitutions—such as those on PBTTT—contract by a distance δ, the unit cell contracts by δ 44

3.12 When stacked substitutions—such as those on C8 or C12—contract by a distance δ, the unit cell contracts by 2δ. This substitution stacking explains the large unit cell contraction exhibited by C8 and C12 and likely explains the cracking behavior 45

4.1 Characteristic fading behavior of ED patterns of C8 under electron flux. At zero dose, samples are highly crystalline with many diffraction spots. Under modest dose (≈ 10 mC/cm^2), odd ($h00$)s disappear indicating formation of twofold screw symmetry on a. Continued exposure results in amorphization characterized by a critical dose of 15.2 ± 2.4 mC/cm^2, though this fading slows at ≈ 30 mC/cm^2. This intermediately ordered phase slowly amorphizes with a critical dose of 52 ± 15 mC/cm^2. 55

4.2 Simulated ED pattern of unsubstituted T5 from data published by *Zhang et al.* (2005). Systematic absences denoted by $\times$. Unsubstituted T5 exhibits the same twofold screw axis on the nominal edge-to-edge packing direction observed in C8 only after modest electron dose. Evidently, preferential degradation of C8 substitutions leads to adoption of symmetry possessed by the unsubstituted variant. . . . 57

4.3 Electron-flux induced fading of C8 ED pattern with higher per-frame exposure time, showing the expansion of the lattice in a and the contraction in b. After sufficient dose ($\approx 2Q_c$), these large diffraction spots quickly fade away, leaving behind small, sharp spots. The sharp spots occupy nearly the same diffraction space locations as the original ($hk0$)s. 59

4.4 Lattice parameter values vs. electron dose for the initial phase (a_1 and b_1) and residual phase (a_2 and b_2). a_1 expands to a maximal value of 1.22 nm before fading as C8 converts to the next phase. b_1 contracts to a minimum of 0.41 nm before converting to the next phase. 60

4.5 Normalized intensity ($I_{(hkl)}(Q)/I^0_{(hkl)}$) vs. dimensionless dose (Q/Q_c) for C8 and C12. The clear breakpoint in decay time at $\approx 2\times$ the critical dose for C8 shows a transition from one predominant disordering mechanism to another. C12, by comparison, shows no breakpoint and amorphizes directly. Curves offset to permit comparison. 61

4.6 Visualization of the transition from the rigidly ordered, as-cast phase to the intermediately ordered phase induced by electron flux. With so few diffraction spots, the intermediately ordered phase is best understood as smoothly varying density fluctuations rather than precisely defined atomic positions. 62

4.7 Characteristics fading of C12 ED patterns under electron flux. At zero dose, samples are highly crystalline with many diffraction spots. As observed with C8, light dose ($\approx$ 10 mC/cm^2) results in formation of twofold screw symmetry in a. Under continued flux, amorphization occurs with a critical dose of 13.3 $\pm$ 1.4 mC/cm^2. In contrast to C8, no long-lived, intermediately ordered phase is observed. 64

5.1 POM of TIPS TFTs used for DC and AC analysis. Channel length is 25 µm. Transistors A and B, exhibiting the best and worst DC behavior, respectively, are highlighted in further analysis. 72

5.2 Histograms of TIPS crystal misorientation from transistors A and B. Transistor A shows a broad distribution of crystal alignments, though a pronounced mode at the high-performance 0° misalignment. Transistor B shows a narrower distribution, though concentrated about a non-ideal mode of 65° 73

5.3 DC operating characteristics for TIPS transistors A and B from Figure 5.1. Devices fabricated on 250 nm SiO_2 with 25 µm × 12 mm channel. Transistor A shows modest mobility and low off current. Transistor B shows low mobility and low off current. 74

5.4 Interpolated transfer characteristics for transistors A and B. Transistor A shows good transfer characteristics and modest mobility, while transistor B shows non-ideal transfer behavior at low V_{DS} and poor mobility. 75

5.5 Hysteresis curves for transistors A and B at V_{GS} = -40 V and -V_{DS} from 0–60 V. Transistor A shows a 0.2 V shift; transistor B shows a shift of 2.5 V 75

5.6 Experimental setup for collection of AC operating characteristics. Various gate-source biases are applied to control free charge in the TFT channel, while a small AC probe signal is applied to the drain-source terminal to probe dynamic charge transport. DC biases may also be applied to the drain-source terminals if V_{DS} = 0 V TFT behavior is nonlinear. 76

5.7 AC operating characteristics of transistors A and B. Characteristics show two features: the tail of the peak from the stage at high frequency, and a single relaxation peak at lower frequency. This peak shows strong dependence on both gate bias and sample. As gate bias increases, peak frequency increases while its impedance magnitude decreases. Transistor A, with high mobility, shows more dramatic variation in impedance. Relaxation frequencies indicated in Z'' plots. Best fit curves are the results of equivalent circuit fitting, described in Section 5.2.4 77

5.8 Equivalent circuit model for TIPS TFTs. The parallel resistor-capacitor pair (R and C) produce the sample behavior; the parallel resistor-CPE pair (R_S, CPE_S) models the behavior of the stability resistor, sample probes, leads, *etc.* 79

5.9 Physical meaning for the resistor and capacitor from the equivalent circuit fits. The gate-bias-dependent resistor, R, represents the channel where hole concentration, p—and thus resistance—is determined by gate bias. The capacitor, C, represents the parallel plate capacitors formed by the gate insulator, gate electrode and source/drain electrodes. 80

6.1 XRD of C12-PBTTT TFTs before and after annealing for 10 minutes at 150 °C. Annealed samples show dramatic increases in crystallinity, as evidenced by the 3× increase in diffracted intensity. Peaks are (001), (002) and (003). Measured d-spacing is 1.92 nm, in agreement with *Chabinyc et al.* (2007b). Peaks offset vertically to permit comparison. 93

6.2 Operating characteristics of as-cast and annealed PBTTT TFTs. As-cast TFTs contain a large dopant concentration, and thus display poor off current. Annealed/de-doped TFTs show very low off current but low mobility, likely due to residual chemical defects introduced by dopants. Devices fabricated on 250 nm SiO_2 with 25 µm × 12 mm channel. 94

6.3 Transfer characteristics for as-cast and annealed devices. As-cast devices show large threshold voltage (≈50 V). Annealed/de-doped devices show poor mobility but low off current. 94

6.4 AC Operating characteristics for as-cast devices. The limited influence of gate bias on impedance magnitude and peak position is the result of the poor field effect observed in Figures 6.2 and 6.3. Fitted data are from best-fit Voigt models to the data. 95

6.5 AC operating characteristics for annealed devices. Devices show improved field effect over as-cast devices, though poor mobility limits the gate bias modulation of channel conductance. Fitted data are from best-fit Voigt models to the measured data. Data to 10^{-2} Hz extrapolated using the equivalent circuit model. The Z' behavior at low frequency is magnified at bottom-left to resolve individual impedance curves. 96

6.6 Experimental setup for collection of AC operating characteristics and VT-IS spectra. 96

6.7 Equivalent circuit model for PBTTT TFTs. A Voigt element fit accurately represents the AC response of these devices before and after annealing and as a function of temperature. R_s describes contributions from instrumentation, as discussed in Section 6.4.8 97

6.8 VT-IS spectra from as-cast PBTTT TFTs. Devices show strong dependence of impedance on temperature. This temperature dependence is manifest as a temperature dependence of channel conductance. Fit data from equivalent circuit modeling. 98

6.9 Arrhenius plot of $G(T) = 1/R(T)$ for as-cast PBTTT TFTs from equivalent circuit data. The slope, -2496 K = -$\Delta E_T/k$. The trap energy calculated from these data is 215 meV. 101

6.10 VT-IS spectra from annealed PBTTT TFTs. Devices show strong dependence of impedance on temperature. This temperature dependence is manifest as a temperature dependence of channel conductance. Fit data from equivalent circuit modeling. Data to 10^{-2} Hz extrapolated from equivalent circuit model. The Z' behavior at low frequency is magnified at bottom-left to resolve individual impedance curves. Data from 70 and 110 °C omitted for clarity of the figure. . 102

6.11 Arrhenius plot of $G(T) = 1/R(T)$ for annealed PBTTT TFTs from equivalent circuit data. The trap energy calculated from these data is 127 meV. 103

LIST OF TABLES

Table

2.1 Lattice parameters for C8 and C12 derived from powder XRD . . . 12

5.1 Fitted equivalent circuit parameters for transistors A and B. Fit resistor, R, shows strong dependence on gate bias. Capacitance, however, increases $< 0.2\%/\mathrm{V}$ of gate bias. 80

5.2 Mobility values calculated from AC operating characteristics. Such mobility values are similar to DC-derived results when low frequency impedance is saturated. Values tend to be higher than DC-derived values when low frequency impedance is not saturated, likely due to poor measurement of the low frequency limit by DC methods. Note that V_T for transistor A is 1.86 V, permitting calculation of mobility at $V_{GS} = 0$. 84

6.1 Fit parameters R and C from equivalent circuit modeling of VT-IS of doped PBTTT TFTs. C shows essentially no variation with temperature while R decreases exponentially with increasing temperature. 98

6.2 Fit parameters R and C from fitting a Voigt model to VT-IS data for annealed/de-doped PBTTT TFTs. C shows an insensitivity to temperature, while R shows exponential dependence on T. 101

B.1 Experimental parameters for IS of TIPS TFTs 120

B.2 Experimental parameters for IS of PBTTT TFTs 120

LIST OF APPENDICES

Appendix

A. Heating Stage Construction and Modification 119

B. Experimental Parameters for Impedance Spectroscopy of TIPS and PBTTT 120

C. Special Concerns for Impedance Spectroscopy of Organic Thin Film Transistors 121

LIST OF ABBREVIATIONS

AC alternating current

AFM atomic force microscopy

C8 Dioctyl pentathienoacene

C12 didodecyl pentathienoacene

CL cathodoluminescence

CPE constant phase element

CVD chemical vapor deposition

DC direct current

DMA Dynamic mechanical analysis

DSC differential scanning calorimetry

ED electron diffraction

EM electromagnetic

ESEM environmental scanning electron microscope

FET field-effect transistors

FIB focused ion beam

GI grazing incidence

IS impedance spectroscopy

ITO indium tin oxide

LC liquid crystal

OTS octadecyltrichlorosilane

P3HT poly(3-hexyl thiophene)

PBO poly(p-phenylene-2,6-benzobisoxazole)

PBTTT poly(2,5-bis(3-alkylthiophen-2-yl)thieno[3,2-b]thiophene)

PE poly(ethylene)

Pn pentacene

POM Polarized optical microscopy

PTFE poly(tetrafluoroethylene)

PVDF poly(vinylidene fluoride)

SAM self-assembled monolayers

SEM scanning electron microscopy

SNR signal-to-noise ratio

STM Scanning tunneling microscopy

T5 pentathienoacene

TEM transmission electron microscopy

TFT thin film transistors

TIPS triisopropylsilyl pentacene

VT-IS variable temperature impedance spectroscopy

VT-POM variable temperature polarized optical microscopy

VT-XRD variable temperature X-ray diffraction

XRD X-ray diffraction

ABSTRACT

Structural Characterization and Impedance Spectroscopy of Substituted, Fused-Ring Organic Semiconductors

by

Charles Michael Shaw

Co-Chairs: David C. Martin and Adam J. Matzger

Organic materials present a number of advantages over silicon that make them ideal candidates for modest performance devices like active matrix backplanes and RFID tags. The work detailed here describes both structural characterization of promising new materials, as well as the adaptation of impedance spectroscopy techniques to the study of organic transistors. Unit cells and solution casting behavior for dioctyl- and didodecyl-pentathienoacene are presented. Dioctyl pentathienoacene has an orthorhombic lattice with parameters a = 1.15 nm, b = 0.43 nm and c = 3.05 nm. Didodecyl pentathienoacene has an monoclinic lattice with parameters $\gamma = 92.2°$, a = 1.10 nm, b = 0.42 nm and c = 3.89 nm. Additionally, thermotropic phase behavior is detailed. Both materials exhibit a "side chain melting" transition—characterized by a dramatic unit cell contraction of more than 20%—and smectic C liquid crystal phases. The side chain melting transition shows similarity to phase transitions elicited by exposing these materials to high energy electron flux. In both cases, disorder in the substitutions results in new phases for these materials. Dioctyl-pentathienoacene also exhibits a unique phase, which is intermediately ordered and

shows a threefold increase in critical dose over the as-cast phase. Impedance spectroscopy of triisopropylsilyl pentacene transistors suggests these devices are well fit by a Voigt model equivalent circuit. The gate bias dependent resistor represents the channel conductance and the capacitor represents the drain-gate and source-gate capacitances. This in turn suggests that conduction occurs through delocalized states available in ordered regions, with disordered regions contributing localized, immobile states. Impedance spectroscopy of poly(2,5-bis(3-alkylthiophen-2-yl)thieno[3,2-b]thiophene) shows similar behavior. The use of variable temperature impedance spectroscopy is also demonstrated. This technique is used to measure the reduction in trap energy—from 200 meV to 140 meV—produced by annealing the material in its liquid crystal phase.

CHAPTER I

Introduction

1.1 The Modern Transistor

The transistor has become ubiquitous in modern electronics, being present in nearly every electronic device (*Horowitz and Hill*, 1989). Due to its high performance and flexible processing (*Anderson and Anderson*, 2004), silicon is the pre-eminent material for a broad range of transistor applications. While this combination will ensure silicon retains relevance for years to come, many modern applications—for which silicon is poorly suited—present opportunities for non-traditional materials to make inroads into commercial electronics. These applications tend to be large area, flexible, and/or low cost electronic devices (*Dimitrakopoulos and Malenfant*, 2002; *Forrest*, 2004).

Due to their low processing cost and mechanical flexibility, organic materials are prime candidates to replace silicon in a number of applications. RFID tags (*Voss*, 2000; *Rotzoll et al.*, 2006), for example, are prohibitively expensive in most cases when manufactured from silicon. Organic materials also have great potential in display applications (*Rogers et al.*, 2001; *Gelinck et al.*, 2004), as their relatively poor performance is more than sufficient for backplane operation in a variety of modern display architectures. Flexible electronics, whether in the aforementioned display applications or electronic textiles (*Wallace et al.*, 2007), present an opportunity where

silicon is entirely unsuitable due to its mechanical properties. Finally, large area applications (displays, photovoltaics, *etc.*) remain cost intensive for silicon, while organic materials keep costs low through a variety of inexpensive processing routes (*Bao et al.*, 1996; *Chang et al.*, 2004; *Street et al.*, 2006).

1.2 Structure and Performance for Organic TFTs

The crystalline and semicrystalline materials used for thin film transistors (TFT)s show strong dependence of performance on macro and microstructure (*Salleo et al.*, 2010; *Virkar et al.*, 2010). To date, organic single crystal TFTs have exhibited the highest carrier mobilities. Rubrene single crystals have exhibited field effect mobilities of 20 cm^2/Vs (*Menard et al.*, 2004), well in excess of the 1 cm^2/Vs benchmark of amorphous silicon it is envisioned these materials will replace. The lack of grain boundaries and low defect concentrations are often cited as responsible for superior performance (*Sundar et al.*, 2004; *Briseno et al.*, 2006). While the largest mobilities have been exhibited by vapor-deposited single crystals, solution cast single crystals have also exhibited very good performance (*Mannsfeld et al.*, 2008) while benefitting from a more cost-effective solution-based process.

Despite their high performance, single crystals may not prove the most desirable route to real-world devices. The formation processes for single crystals are typically time consuming, costly and limited to small areas (*Liu et al.*, 2009). Further complicating the use of single crystals is that single organic crystals often exhibit significant mobility anisotropy—up to two orders of magnitude (*Dewijs et al.*, 2003). While means to influence crystal orientation to combat the anisotropy problem have been demonstrated by, for example *Chen et al.* (2001); *Swiggers et al.* (2001); *Chou and Cheng* (2004), such steps further complicate the use of single crystals in TFTs.

Polycrystalline TFTs reduce or eliminate mobility anisotropy due to their distributed grain orientation. Polycrystalline films are also readily fabricated over large

areas or into device arrays from a number of processes (*Sirringhaus et al.*, 2000; *Shtein et al.*, 2004). However, polycrystalline films, by definition, contain grain boundaries that potentially act as significant barriers to charge transport (*Horowitz and Hajlaoui*, 2000). In spite of these concerns, however, polycrystalline devices with performance rivaling amorphous silicon have recently been reported (*McCulloch et al.*, 2006; *Yuan et al.*, 2009). While performance in these devices does not match that of the best single crystal devices, polycrystalline devices made from simpler processes—where performance is just good enough—may experience greater adoption outside research labs.

1.3 Liquid Crystals

In contrast to crystalline materials, liquid crystals have unique structural characteristics that my prove interesting in the study of the relationships between molecular packing and charge transport. The relaxed ordering conditions and relative fluidity of liquid crystals compared to crystals permit the formation of large domains with smoothly varying molecular orientations (*Kumar*, 2001; *Kléman and Lavrentovich*, 2003). Such films could demonstrate reduced, or potentially no, mobility anisotropy due to the lack of a preferred molecular orientation throughout the film. Defects such as disclinations and dislocations are present in these films, though grain boundaries—oft cited for their negative effects on charge transport—have not been observed in the films of many common liquid crystalline phases (*Durst and Voigt-martin*, 1986; *Voigt-Martin and Durst*, 1989). Additionally, paramorphosis—the retention of key textural characteristics of a liquid crystal phase on cooling to a higher symmetry phase—offers the potential to incorporate unique structural characteristics of liquid crystals into solid films (*Wiegeleben and Demus*, 1988).

Recent results investigating the capability of liquid crystals for semiconductor applications have shown significant potential (*Hanna*, 2005; *O'Neill and Kelly*, 2011).

Mobility values measured through phase series tend to show decreases of an order of magnitude at the transition to a lower symmetry phase (*Funahashi and Hanna*, 2000). Noteworthy, however is the demonstration of ambipolar charge transport in certain smectic phases (*Funahashi et al.*, 2007) and nematic glasses (*Zheng et al.*, 2007). Furthermore, transport in smectic and discotic phases has been observed to be largely independent of temperature and field (*Funahashi and Hanna*, 1997a,b). Device measurements exploiting paramorphosis have also demonstrated good device performance in spite of the development of visible domain walls and cracks during the cooling process (*O'Neill and Kelly*, 2003). More recently, several main-chain, liquid crystal (LC) polymers have received tremendous attention for their capability to reorder in a mesophase (*McCulloch et al.*, 2006, 2009). Devices formed from as-cast films perform modestly, though mobility improves dramatically—to 0.5 cm^2/Vs or greater—by incorporating an LC annealing step in the processing.

1.4 The Interface Layer

Whether devices are formed from single or multiple crystals, there is significant evidence that transport depends most on the first few nanometers of semiconductor atop the gate dielectric (*Horowitz*, 2004; *Dinelli et al.*, 2004). Such findings are more significant in the context of recent results. Orientation mapping of the first and second monolayer in pentacene (Pn) films on SiO_2 shows that both layers orient with (001) parallel to the substrate, but with vastly different in-plane orientation (*Kalihari et al.*, 2009). Third, fourth, *etc.* monolayers of Pn are observed to maintain the in-plane orientation of the Pn monolayer directly beneath, indicating it is only the first layer—the layer most responsible for transport behavior—that differs from the rest of the film.

Such results are not unique to Pn on SiO_2. Scanning tunneling microscopy (STM) results indicate that growth on gold, for example, results in the first Pn layer lying flat

with π orbitals normal to the substrate (*Schroeder et al.*, 2002). With continued deposition, Pn molecules adopt the typical texture *i.e.* aligned nominally perpendicular to the substrate.

Such detailed experiments have not yet been conducted on other common materials, so it is unclear if similar layer-to-layer misorientation exists beyond pentacene. It does, however, present the possibility that structural characterization that focuses on the top or bulk of thicker semiconductor films—*e.g.* atomic force microscopy (AFM), scanning electron microscopy (SEM), X-ray diffraction (XRD), *etc.*—do not accurately reflect the structure at the interface layer. Transmissive or cross-section techniques (*e.g.* transmission electron microscopy (TEM), focused ion beam (FIB)) are potential routes to direct structural characterization of this interface. While significant work has been done to characterize these materials using these techniques (*Gonzalez Ronda and Martin*, 1997; *Drummy et al.*, 2002; *Drummy and Martin*, 2005; *Chen*, 2006), such experiments are performed on alternate substrates than the SiO_2 or self-assembled monolayers (SAM)s comprising the gate dielectrics in most modern devices.

An alternate possibility would be the use of sophisticated electronic measurements of TFTs. Due to the fact that charge is only carried in material nearest the dielectric interface, results from these experiments reflect only the relevant material. Charge transport models that depend upon structural details in this layer could thus be used to indirectly study the structure of this interface layer. Results from simulations and spectroscopic techniques have revealed, for example, trap energies that certain chemical or structural defects produce (*Northrup and Chabinyc*, 2003; *Chabinyc et al.*, 2007a; *Benor et al.*, 2008). Models also exist that permit determination of such trap energies from electronic characterization (*Stallinga and Gomes*, 2006b; *Stallinga*, 2009). By correlating electronic measurements of trap energies from devices with spectroscopic and simulation determinations of their expected values, aspects of the

structure in this interface layer can be determined indirectly.

Another such technique, which has seen little application in organic TFTs, is impedance spectroscopy (IS). There is significant precedent in the literature for the determination of structural properties through IS, however. *Bauerle* (1969), for example, has used IS to determine structural details for solid zirconia electrolytes. Included in such analysis is a determination of charge transport parameters specific to transport in grains, grain boundaries and at electrode surfaces. Similar work on calcium stabilized zirconia has been performed by *Beekmans and Heyne* (1976), while *Bruce and West* (1983) applied such techniques Li electrolytes.

The ability to resolve these various transport parameters originates from the variations in carrier mobility in these different regions. Transport in grain interiors is typically rapid, while transport through or across grain boundaries is comparatively slow. The frequency dependence of IS measurements thus separates these contributions by their frequency (or speed). As such, IS presents the possibility of determining transport parameters for the various structures present in the interface layer of organic TFTs in a single experiment.

1.5 Thienoacenes

To date, one of the most successful organic materials for TFTs is Pn, which has displayed hole mobility in excess of 1 cm^2/Vs (*Lin et al.*, 1997). Solubilized descendants of Pn—formed by substitution of soluble groups on the central acene ring (*Anthony et al.*, 2002)—have also shown high hole mobilities competitive with amorphous silicon (*Chen*, 2006). Despite promising performance of these materials, Pn is plagued by poor chemical stability (*Yamada et al.*, 1988). One route to address this problem of chemical stability has been to replace some of these acene rings with thiophene (*Laquindanum et al.*, 1998), though performance was modest.

More recently, materials were synthesized that replaced all five acene rings with

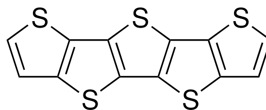

Figure 1.1: T5 combines the chemical stability gains of thiophene over acene rings while maintaining the rigid planarity of Pn

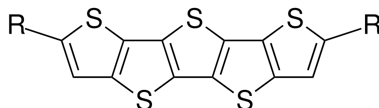

Figure 1.2: T5 substituted with solubilizing alkyl groups. R = C_8H_{17} or $C_{12}H_{25}$.

thiophene units (*Zhang et al.*, 2005) (Figure 1.1). Such materials—termed thienoacenes—present a potential new candidate for rigorous study. Like Pn, the unsubstituted, five-ring thienoacene—pentathienoacene (T5)—is largely insoluble and difficult to process. The crystal structure of this material is promising for transistor applications, however, as the molecules pack nearly planar with close face-to-face and edge-to-edge packing. Computational studies of the charge transport behavior for T5 produce promising results (*Kim et al.*, 2007), though devices fabricated from these materials have fallen somewhat short of these predictions (*Xiao et al.*, 2005).

One potential cause for this discrepancy is the low solubility of T5: thermally deposited T5—used to fabricate the previously cited devices—produces polycrystalline films while simulation results are based on single crystals. Soluble variants of T5 have also been synthesized with alkyl sidechains of various lengths attached at the α and α' positions (Figure 1.2). These substitutions dramatically improve solutibility, permitting facile solution processing (*Zhang*, 2006). Dioctyl pentathienoacene (C8) and didodecyl pentathienoacene (C12)—the symmetric dioctyl- and didodecyl- substituted variants of T5—are the subject of Chapters II, III and IV. In these chapters, the crystal structure and thin film behavior are discussed in detail, along with thermal and electron flux-induced phase transitions in these materials.

1.6 Dissertation Outline

Chapters II, III and IV discuss direct structural characterization of C8 and C12. These chapters cover room temperature phases as well as transitions to less ordered states brought about by heat flow or electron beam exposure. Chapters V and VI approach structural characterization of triisopropylsilyl pentacene (TIPS) and poly(2,5-bis(3-alkylthiophen-2-yl)thieno[3,2-b]thiophene) (PBTTT) more indirectly through IS of TFTs of these materials.

Chapter II covers the determination of unit cells for room temperature, crystalline phases of both C8 and C12. Thin-film solution growth behavior is also discussed. These unit cells are highly anisotropic with two molecules aligned largely parallel to the *c* crystallographic axis. Such an arrangement produces alternating layers of insulating substitutions and thienoacene cores, which in turn gives rise to numerous interesting phase behaviors discussed in Chapters III and IV. When cast into films, both materials form large single crystals with dimensions in excess of 100 µm and clear faceting, enabling the determination of molecular orientation from optical means. Molecular arrangements in cast films are also ideal for single crystal TFTs, with the direction of poor conduction perpendicular to the substrate.

Chapter III covers the thermal transitions exhibited by both substituted T5s. Both materials undergo a solid-solid phase transition—oft termed a "side chain melting" transition—driven by disorder in the substitutions. While such a transition has been observed frequently in similar materials, the microscopic and macroscopic implications for this transition are more profound for C8 and C12 due to details of crystal packing. Both materials also exhibit a smectic C phase.

Chapter IV covers a unique phase transition observed in C8. This transition is induced by exposure of C8 crystals to the high energy electrons from the beam of a modern TEM. Like the thermal transitions discussed in Chapter III, this transition is driven by the introduction of disorder into the substitutions. Despite this similar-

ity, the electron flux induced transition is fundamentally different from the thermal transitions from Chapter III. In the thermal transition, substitutions gain freedom of motion at elevated temperatures and adopt defective conformations; in the electron flux transition, these substitutions are disordered through broken bonds and atomic displacements.

Chapter V covers the application of IS techniques to TFTs made from TIPS, a well-studied, solution-processable Pn descendant with good mobility. Results from these experiments have implications for the persistent question of the structure of such materials at the dielectric interface. The response of these devices to alternating current (AC) signals suggests that channel transport is frequency independent to 100 kHz, which in turn implies conduction occurs predominantly through the delocalized states available in ordered segments of the film. An alternate method for calculating field-effect mobility is also presented, which is especially useful for devices with high resistances and/or gate dielectric capacitances.

Finally, Chapter VI covers the application of variable temperature impedance spectroscopy (VT-IS) techniques to TFTs made from the high performance LC polymer semiconductor PBTTT. These experiments permit estimation of the depth of energy traps in as-cast and annealed devices. Unlike the spectroscopic techniques often used to identify such states, however, these techniques are also able to localize these traps to those first few molecular layers where charge transport takes place. While such experiments can be conducted using conventional direct current (DC) methods, the use of these AC methods has the added benefit of decoupling the field-dependence of mobility from measurements, permitting more direct measurement of trap energy. These techniques also work at much lower voltages, reducing the potential for voltage-driven breakdown of the material under test.

CHAPTER II

Crystal and Thin-Film Structure of Alkyl-Substituted Pentathienoacenes

2.1 Introduction

With the strong dependence of electronic structure on local molecular packing, detailed knowledge of this structure is essential for utilization of electronic materials (*Grosso and Parravicini*, 2000). This is as true for organic materials as inorganic, especially given the large anisotropy of charge carrier mobility seen in many organics (*Dewijs et al.*, 2003). Mobility in rubrene, for example, measured along the *a* axis is often five to ten times lower than the perpendicular direction (*Ling et al.*, 2007). Similar results are seen in TIPS where anisotropy ratios of 10:1 are observed (*Chen*, 2006). Comparable anisotropy ratios are observed even in polycrystalline Pn TFTs with partial in-plane alignment (*Chou and Cheng*, 2004).

With the mobility anisotropy ratio of high performance, small molecule, organic semiconductors hovering around 10:1, in-plane texturing becomes a crucial issue for successful device fabrication. With the exception of rubrene (*Menard et al.*, 2004), alignment of the semiconductor perpendicular to the ideal transport direction drops mobility below the baseline 1 cm^2/Vs expected for successful devices. The identification of molecular alignments is thus of principal importance for promising new

materials.

2.1.1 Chapter Overview

In this Chapter, crystalline structures for C8 and C12 are proposed based on powder XRD and molecular modeling. These results predict similar packing motifs for both C8 and C12. Both materials have two molecules per unit cell arranged edge-to-edge in the (210) plane for C8 and the $(2\bar{1}0)$ plane for C12, with π-stacking along [210] for C8 and $[2\bar{1}0]$ for C12. For both materials, the long molecular axes are near parallel to [001]. Charge transport in [001]—due to the long substitutions lying in the conduction path—is likely poor in comparison to transport in the various $[hk0]$ directions.

Additionally, thin film growth behavior for both materials is discussed. Both C8 and C12 grow large, discrete single crystals from solution. Such crystals are excellent candidates for single crystal TFTs. Furthermore, solution grown crystals of both C8 and C12 have strong texturing with $(00l)$s parallel to the substrate. This is especially beneficial for TFTs, as the direction of poor conduction is excluded by simple growth processes. The faceting behavior of both crystals is an additional benefit, as molecular orientations can be determined from optical inspection of films.

2.2 Results & Discussion

2.2.1 Crystal Structure

Unit cell parameters for C8 and C12, as determined by powder XRD, are summarized in Table 2.1. These unit cells mirror the anisotropy of the T5 molecules themselves, with a narrow packing direction—presumably the face-to-face packing—a broader packing direction—likely edge-to-edge—and a significantly larger spacing that must correspond to the molecular long axis. Supporting these assertions is the

	C8	C12
a (nm)	1.15	1.10
b (nm)	0.43	0.42
c (nm)	3.05	3.89
γ (°)	90	92.9
Lattice System	Orthorhombic	Monoclinic

Table 2.1: Lattice parameters for C8 and C12 derived from powder XRD

relative insensitivity of the a and b values to changes in the length of the substitutions (4% and 2% respectively). The c lattice parameter, however, demonstrates significant dependence on substitution length: didodecyl substitutions increase c by 21.5%. Furthermore, assuming all *trans* in the substitutions, addition of two butyl segments to the ends of C8 increases the overall molecular length by 1.01 nm, comparable to the actual increase in c. Possible space groups for C8 are $P222$, $Pmm2$ and $Pmmm$. Possible space group for C12 are $P2$, Pm and $P2/m$. See section 2.4.3 for a discussion of space group refinement.

The volumes, and therefore densities, of these unit cells strongly indicate 2 molecules per unit cell. For C8, the density is either 0.59 g/cm^3 or 1.17 g/cm^3 for 1 or 2 molecules, respectively. For C12 the density is either 0.60 g/cm^3 or 1.19 g/cm^3 for 1 or 2 molecules. In both cases, the density resulting from single molecule per unit cell is so small as to be suspect, while a third molecule per cell results in densities so high as to be likewise improbable. Two molecules per cell gives densities exactly in line with the expectation for crystalline organics.

Given the shape of the unit cell, the presence of two molecules per cell, and the dependence of c on substitution length, the unit cells for both C8 and C12 must contain the two molecules aligned near parallel to c with approximately $\frac{1}{2}a$ separating them. The finer details of atomic arrangements for these materials were predicted by molecular modeling simulation. The crystal structures predicted from such simulations are presented in Figures 2.1 and 2.2. Both cells contain the pair of T5 cores

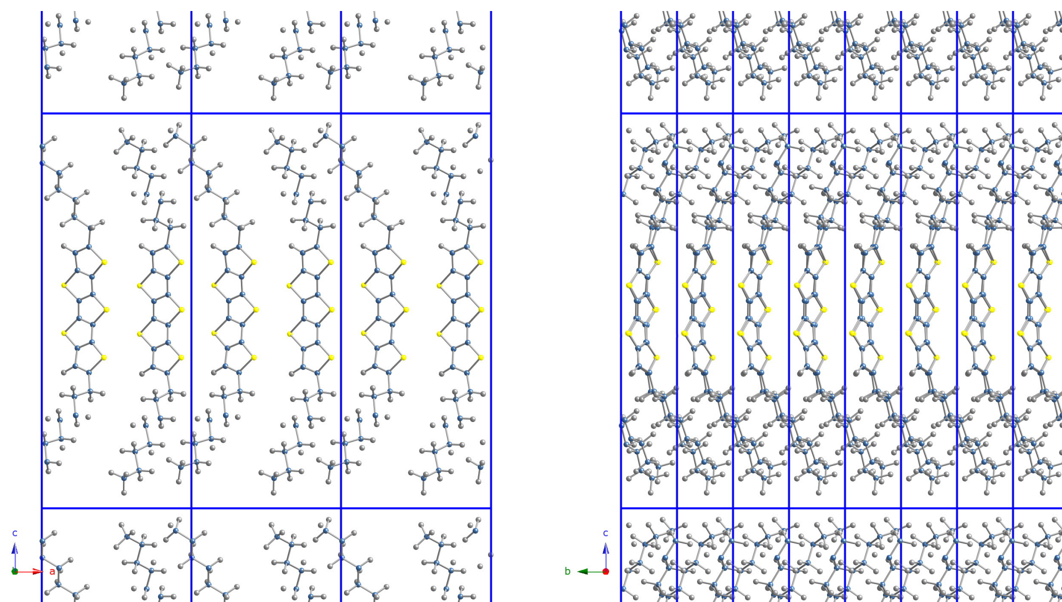

Figure 2.1: Atomic positions of C8 molecules predicted by molecular modeling inside unit cells determined from powder XRD. View directions are [010] (left) and [100] (right)

aligned near-parallel to [001], a characteristic inherited by less ordered, high temperature phases discussed in Chapter III. These characteristics are also retained in the electron-beam induced phase discussed in Chapter IV.

When viewed along [100] or [010], the structures of both C8 and C12 are clearly composed of alternating layers of conjugated, (semi)conducting T5 and saturated, insulating substitutions. This molecular arrangement presents potential barriers to charge transport along [001], especially given the length of the substitutions and the prediction of no interdigitation of those substitutions. As simulated, conductive layers 0.97 nm thick are sandwiched between insulating layers 2.08 nm thick in C8, while in C12 these insulating layers grow to 2.92 nm. While this layered arrangement does not entirely preclude conduction along [001], significant barriers to transit along this path exist that are absent along the various $[hk0]$ paths.

This supposition that adjacent, substituted T5 molecules arrange as they do, with alternating conductive and insulating layers, has additional justification in the struc-

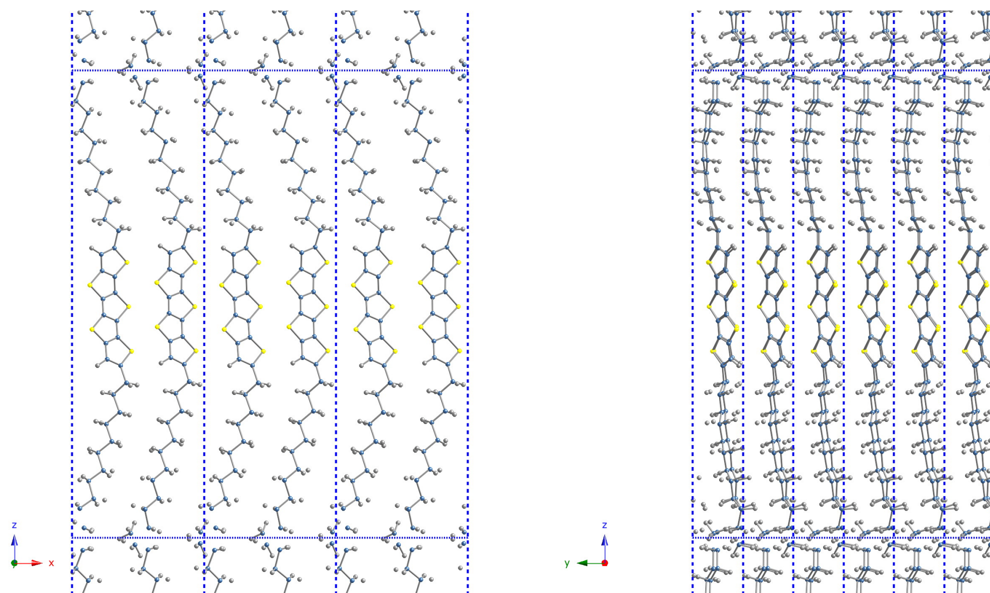

Figure 2.2: Atomic positions of C12 molecules predicted by molecular modeling inside unit cells determined from powder XRD. View directions are [010] (left) and [100] (right)

tures of unsubstituted T5. In T5 crystals, intermolecular sulfur-sulfur interactions were implicated in the proximity of sulfur atoms from adjacent molecules (*Zhang et al.*, 2006). It is reasonable to suppose that such forces are at work in these substituted T5s, contributing to the segregation of substitutions and thienoacenes.

These simulations also predict a face-to-face packing motif for both C8 and C12 (Figure 2.3). In these models, the T5 face normals are inclined at an angle of $\approx 33°$ to [010] for C8 and $\approx 35°$ for C12. As simulated, adjacent C8 molecules are separated by ≈ 0.34 nm in the face-to-face (π-stacked) direction; edge-to-edge, the T5 cores of C8 are ≈ 0.35 nm apart. In C12, adjacent molecules are separated by 0.35 nm in the face-to-face direction and approximately 0.32 nm edge-to-edge. As C8 cores lie near-parallel to (210), the π-stacking direction is nominally [210] with edge-to-edge packing in the (210) plane. For C12, T5 cores are largely parallel to $(2\bar{1}0)$ with π-stacking nominally in $[2\bar{1}0]$.

The face-to-face separation in unsubstituted T5—at 0.34 nm (*Zhang et al.*, 2005)—

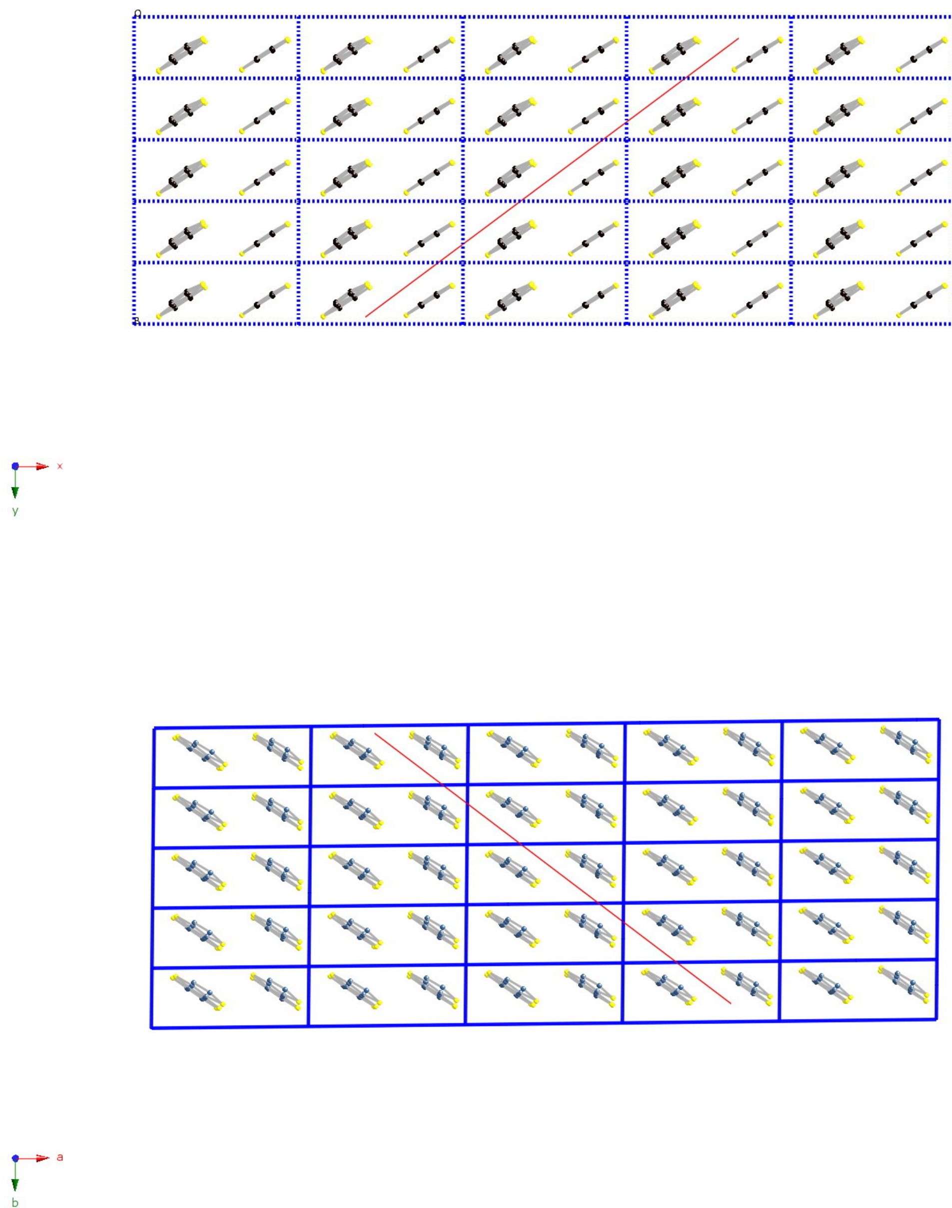

Figure 2.3: Simulated C8 (top) and C12 (bottom) unit cells as viewed on [001]. Alkyl substitutions hidden to permit view of T5 cores. T5 cores lie essentially parallel to (210) in C8 and $(2\bar{1}0)$ in C12, as indicated by red lattice planes in these figures. π-stacking is thus along [210] for C8 and $[2\bar{1}0]$ for C12.

is quite comparable to these predictions of π-stacking distances in both C8 and C12. Evidently the bulky substitutions, perhaps owing to their longitudinal rather than traditional transverse placement, do not drive the cores of these substituted T5s apart. These bulky substitutions do, however, rotate the T5 cores further than the native rotation of the unsubstituted variant. In unsubstituted T5s, core rotation is approximately 25.1°, nearly 10° smaller than in these predicted structures.

2.2.2 Thin Films

Figure 2.4 contains characteristic micrographs of solution-cast C8 films grown with differing deposition conditions. The quickly-grown films, are composed of a large number of modest-sized crystals showing no clear facets. These crystals have either low aspect ratio (near unity) or form high aspect ratio (≥ 10) needles. Unity aspect ratio crystals have dimensions in the range of 50–80 µm, while needles are hundreds of microns long but less than 25 µm wide. While their modest size is sufficient to cover the channel of an TFT, the voids between individual crystals are potentially problematic. Controlling the precise location of crystal growth, perhaps through use of surface treatment methods—such as those described by *Mannsfeld et al.* (2007)—may be sufficient to combat this issue.

Slowly grown films show similar features to those formed by rapid evaporation, but produce noticeably superior films. The two geometries observed in rapidly grown films—when given sufficient crystallization time—evolve into two principal crystal habits: needle and tablet. Needle crystals are narrow with 10 µm width but lengths exceeding 500 µm. Tabular crystals vary from 50 µm to 200 µm across with small aspect ratios typically between 1 and 2.

As these crystals are oriented with (001) parallel to the substrate (see XRD below), observed facets are various (hk0)s. Interfacial angles of these crystals identify the facets as (100), (010) and (110). Needle and tablet crystals show growth anisotropy,

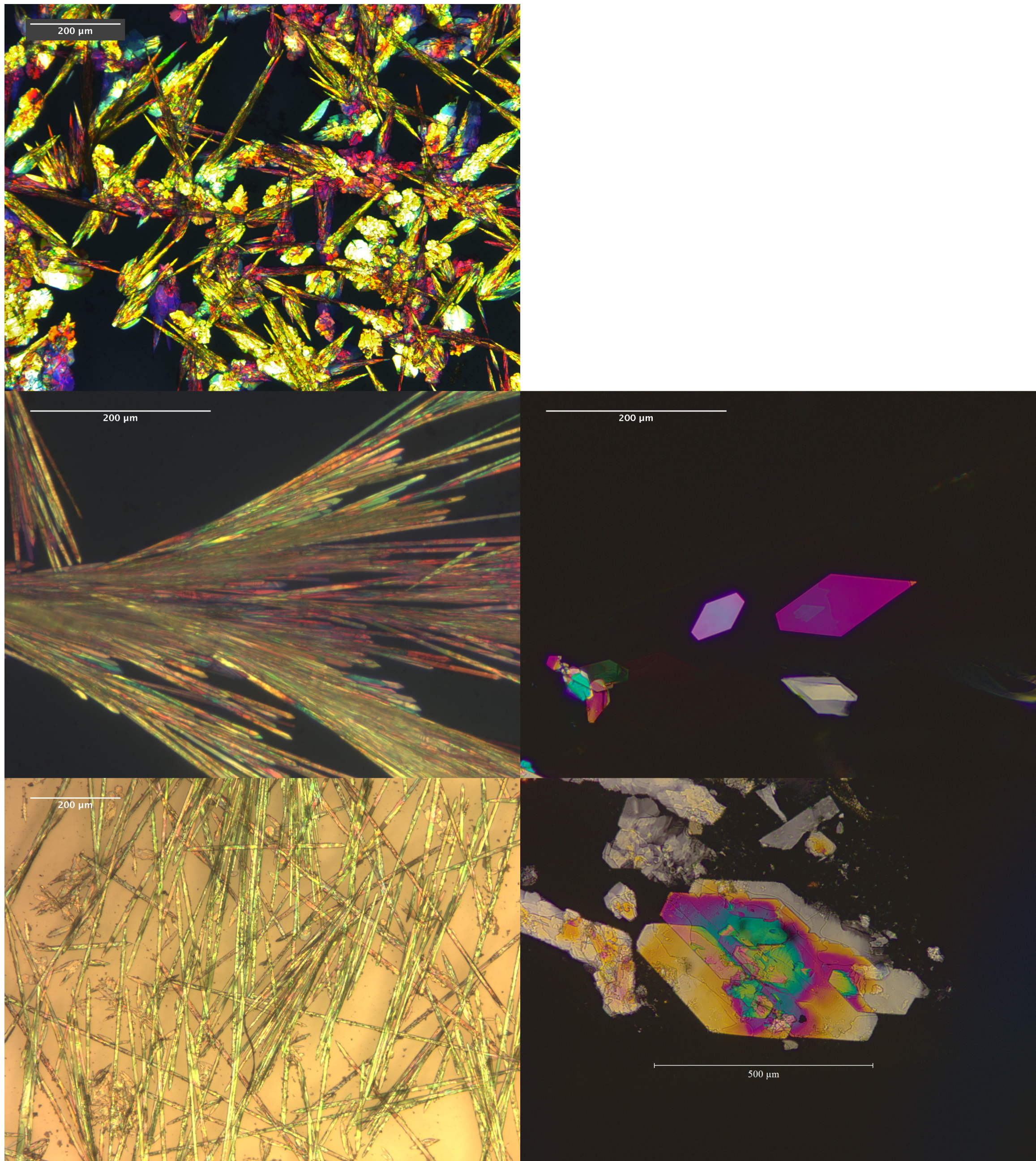

Figure 2.4: POM of C8 films grown from 0.1% by weight solutions in toluene. All films grown at room temperature. Films grown with quick (≈30 minutes) evaporation (top) show small crystals with poorly realized needle and tablet habit. Films with slow (≈8 hours) evaporation (middle) showing large crystals and both habits. Large but rough crystals of both habits from suspension crystallization (bottom).

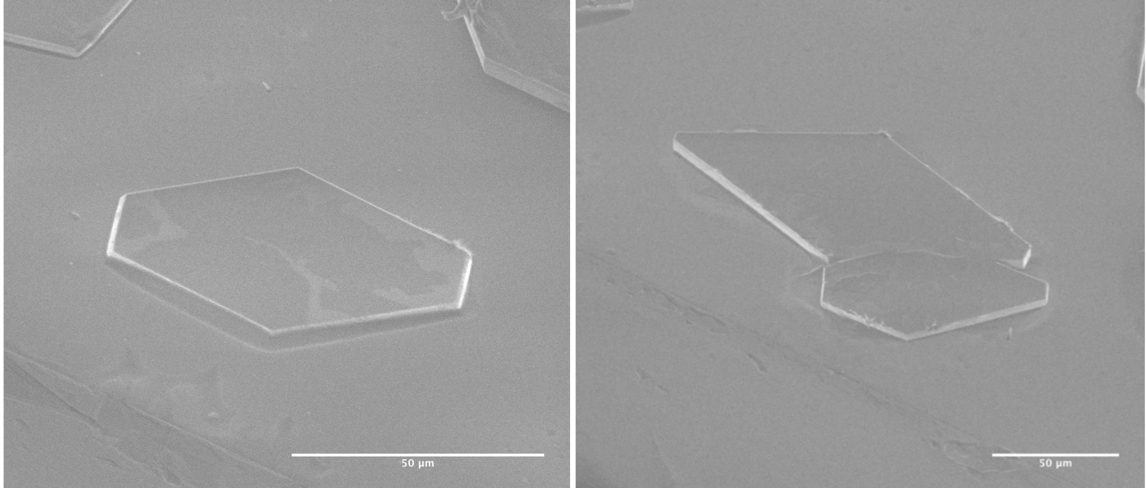

Figure 2.5: SEM of slowly grown C8 crystals showing slow growth in [001].

with fastest growth along [100]. Given the dramatically different geometries adopted from seemingly identical deposition conditions, the growth rate in [010] is clearly unstable in the minutiae of local conditions, while [100] is consistently rapid.

SEM of these slowly grown crystals (Figure 2.5) reveals the slow growth of C8 crystals in [001]. Crystal thickness along [001] is typically 5% or less the thickness in lateral directions: for crystals 100 µm wide, thickness is ≈5 µm. While not especially concerning for thin film devices such as TFTs, single-crystal XRD of C8 will be complicated by the small number of (001) planes present for diffraction.

For use in TFTs, these slowly grown crystals are superior. Single, tabular crystals could cover entire channels, while single needles could—if appropriately placed—produce many TFTs. The clear faceting also gives immediate knowledge of molecular orientation relative to charge transport from simple, optical means. The principal challenge, much as for quickly grown films, is control over growth location. Surface treatments to control nucleation site may be sufficient for this task. Another viable option may be an adaptation of delamination methods previously reported for polymer films (*Chabinyc et al.*, 2004).

Another option for control over crystal location and orientation may be the use

of suspensions of crystals rather than solutions for casting C8 films. Suspended crystals provide a means to selectively deposit such large crystals with some precision. Additionally, the highly anisotropic needle crystals should permit orientation control through either solvent flow or jamming at sufficient concentration. Crystals grown in this manner again show the two prominent habits. While large, faceted crystals are still produced, these surfaces are clearly not as smooth as when grown on a substrate. The quality of the interface with the gate insulator for TFTs is of paramount importance; the quality of this interface in suspension-cast films is suspect given this roughness.

Thin film XRD of C8 (Figure 2.6) corroborates many of the observations made optically. Regardless of deposition process, the patterns show the strong texturing exhibited by C8 with (001) parallel to the substrate. Such preferred orientation, with substitutions perpendicular to the substrate, is frequently observed in substituted organic semiconductors (*Chabinyc*, 2008; *Brinkmann and Rannou*, 2009). Such texturing is desirable for the use of C8 in TFTs, as it indicates a preference to align [001]—likely the direction of poorest conductivity—perpendicular to the flow of charge. The films are also highly crystalline, as evidenced by the presence of high order peaks, as high as (007), along the meridian.

The streaking observed in XRD patterns of the needle crystals reveals texturing behavior of needle clusters not observed optically. When stacked, as they are in Figure 2.4, many C8 crystals—likely those not in contact with the substrate—rotate so their [001] are out of alignment with the substrate normal. Such rotation is potentially concerning for top-contact devices, as conduction paths now more likely contain insulating [001] segments. Top contact devices, as discussed in Chapter III, are fraught with other problems, so this concern is likely minimal. This rotation is not observed in tabular habit crystals.

On the edge of these diffraction patterns—especially those for the quickly grown

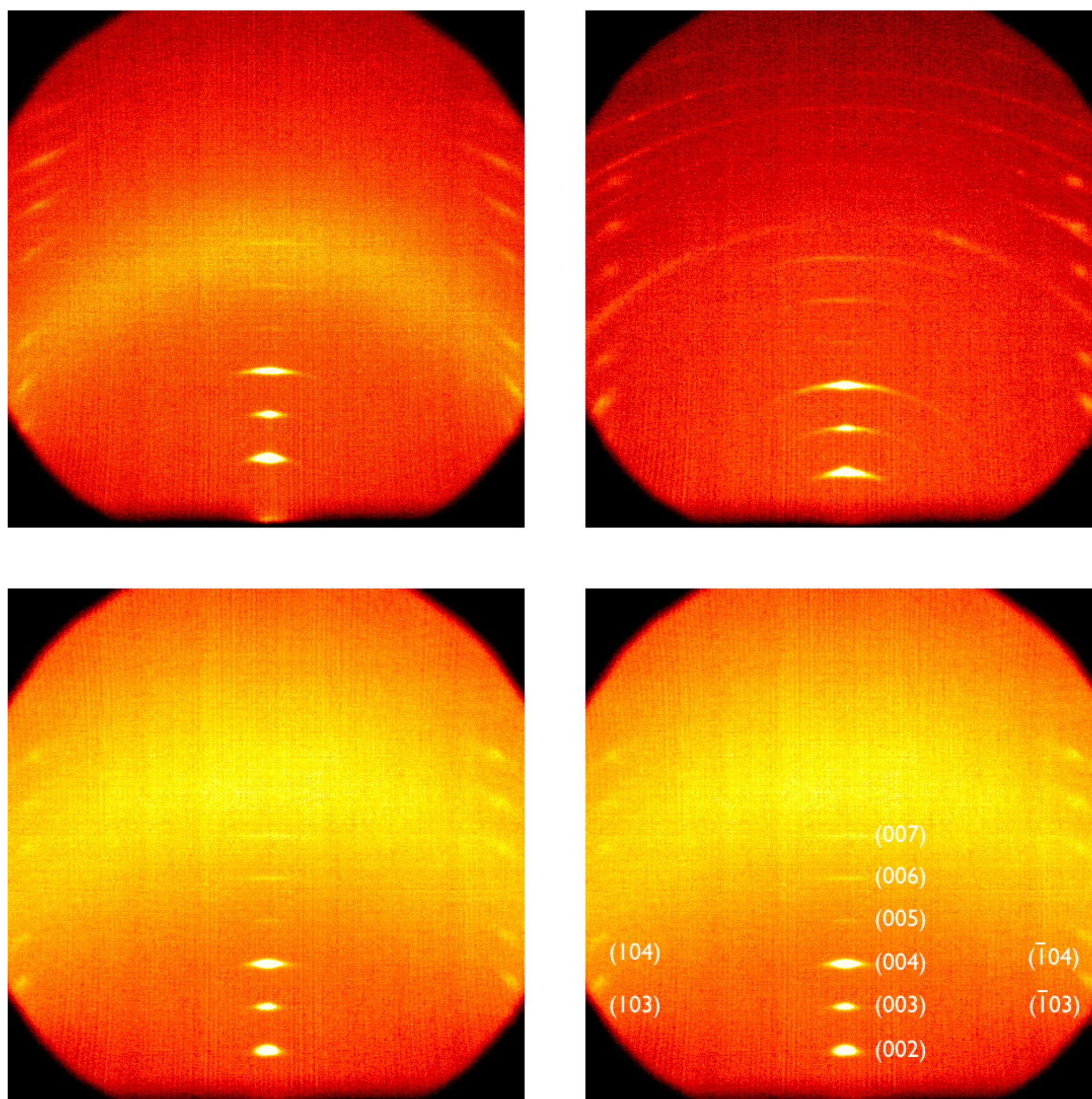

Figure 2.6: Thin film XRD of C8 films. All films grown at room temperature. Quickly grown films (upper left) showing strong texturing of $(00l)$ parallel to substrate despite fast solvent evaporation. Slowly grown, needle habit crystals (upper right) showing rotation of crystal stacks. Suspension crystallized needles (lower left) showing very strong texturing. Miller indices for observed spots (lower right)

films and the suspension crystallized films—relatively sharp points with little streaking are observed. While their presence may, at first, seem to indicate a single crystal texture to these films, prior micrographs clearly indicate otherwise. Rather than a true single crystal texture to these films, those spots—($h0l$)s—result from the fraction of C8 crystals oriented in the appropriate Bragg condition. As was seen with Pn, these substituted T5s adopt a fiber texture despite their film geometry (*Drummy*, 2003).

Slowly grown C12 films are composed of modestly sized (≈30–50 µm, Figure 2.7) single crystals with sharp faceting, as well as larger crystals (up to ≈ 100 µm) exhibiting similar faceting but lesser outward crystal perfection. This faceting is predominantly (010) and the various (110)s, again echoing observations of C8. Crystals with a needle habit have not been observed in slowly grown crystals. Thin-film XRD of C12 confirms optical inferences: (001) lies parallel to the substrate. Most C8 observations hold true for C12 as well: films are highly crystalline, strongly textured and ideally oriented for in-plane charge transport. With no needle-shaped crystals—and therefore no stacked crystals with [001] misalignment—no streaking of ($00l$)s or other peaks is observed. As with C8, C12 exhibits a fiber texture despite film geometry.

Characteristic electron diffraction (ED) patterns of single, solution-grown C8 and C12 crystals are provided in Figure 2.8. Both diffraction patterns agree further with XRD results, namely that these substituted T5s strongly prefer to grow with ($00l$)s parallel to the substrate.

2.3 Conclusions

Unit cell parameters for C8 and C12 were determined through ED, thin film XRD and powder XRD. For C8, the data indicate an orthorhomic unit cell with parameters $a = 1.15$ nm, $b = 0.43$ nm and $c = 3.05$ nm; for C12, the data indicate a monoclinic (c-unique) unit cell with parameters $a = 1.10$ nm, $b = 0.42$ nm, $c = 3.89$ nm and $\gamma =$

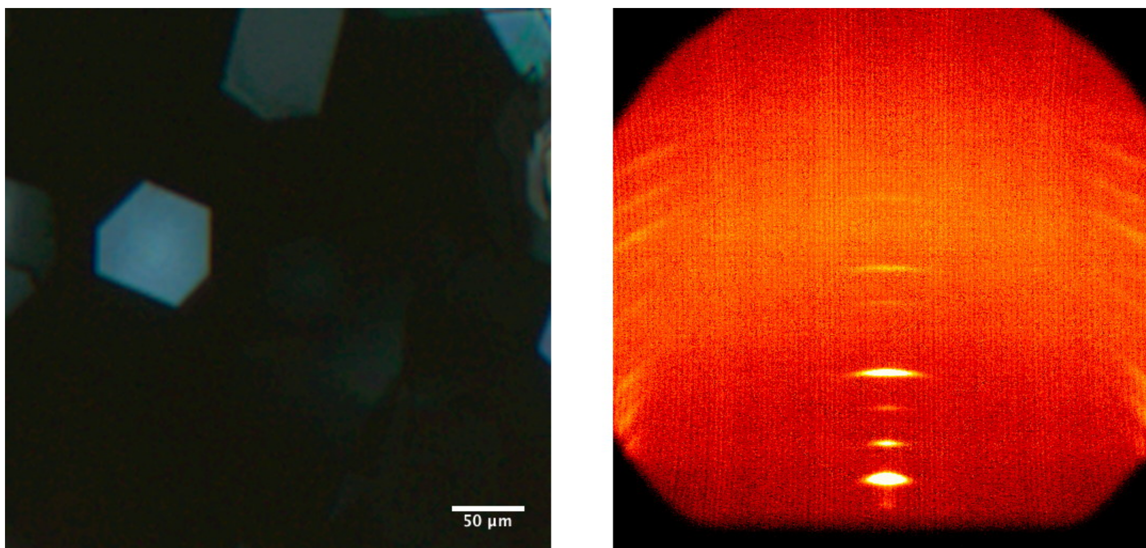

Figure 2.7: POM and XRD of slowly grown C12 thin films. POM of C12 showing tabular habit and large crystal size (left) and XRD showing strong texturing of $(00l)$ parallel to the substrate (right).

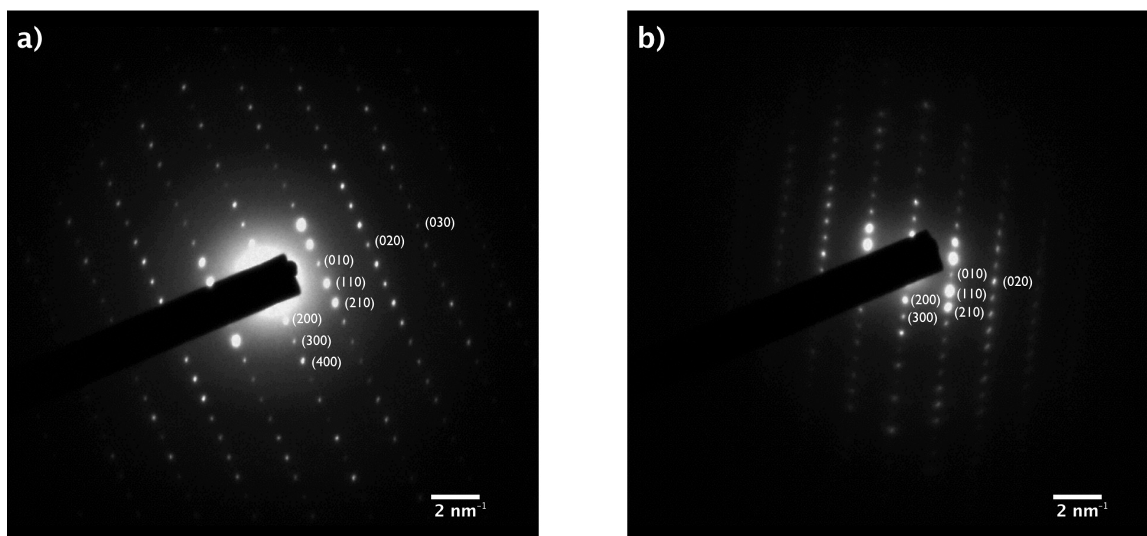

Figure 2.8: Representative ED patterns of a) C8 and b) C12 thin films exhibiting the same strong texturing observed *via* XRD. Zone axis for both patterns is nominally [001]

92.9°. Minimized energy simulations predict both molecules align largely parallel to the c axis for both materials. These simulations also predict face-to-face packing for both materials, with close intermolecular packing: 0.34 nm face-to-face and 0.35 nm edge-to-edge for C8 and 0.35 nm face-to-face and 0.32 nm edge-to-edge for C12.

Thin films of both C8 and C12 are highly crystalline and strongly textured with [001] parallel to the substrate normal with a random distribution of orientations in-plane. Both materials form large, discrete, single crystals when slowly crystallized. C8 and C12 frequently form crystals with tabular habit, though high aspect ratio needles of C8 are also formed. The strong texturing, large crystals and clear faceting allows significant structural detail to be inferred from simple, optical methods.

The large size and quality of C8 and C12 crystals produced through simple solution casting is promising for these materials' use in TFTs. Additionally, their natural texturing is ideal for thin-film devices with in-plane charge transport. Methods for controlling the position and orientation of these crystals—whether during or after deposition—should be developed or adapted in order to fabricate devices from these promising materials.

2.4 Materials & Methods

2.4.1 Materials

C8 and C12 were examined in these studies; synthesis of both is described elsewhere (*Zhang*, 2006). Materials were used as-received after the final sublimation purification step described in *Zhang* (2006). Toluene (ACS Reagent grade, ≥99.5%) was used as-received from Sigma-Aldrich.

2.4.2 Powder X-ray Diffraction

Powder XRD samples of C12 were used as recovered from sublimation purification. C8 powder direct from sublimation purification, however, is typically composed of two C8 polymorphs, as discussed in Chapter III. In contrast, solution-cast films of C8 contain only the room temperature polymorph. In order to examine the room temperature polymorph, polycrystalline C8 thin-film XRD samples were removed from glass slides with a razor blade. The collected powder was then used for powder XRD.

For both C8 and C12, a small amount of powder was placed on a glass slide and smoothed gently with a second glass slide. Data were collected using a Bruker D8 Discover with a 500 µm monocapillary collimator and HI-STAR 2D detector. The incident beam was held at a fixed 5°. Data were collected with the detector at 10°, 25° and—for C12 only—40° with a camera length of approximately 30 cm. Data were collected for 20 minutes at each detector position. Powder samples were continuously rotated about the normal axis of the glass substrate to reduce the effects of preferred orientation. The instrument was calibrated with a NIST1976 (corundum) flat plate standard prior to use.

2.4.3 Unit Cell Parameter Determination

Data were analyzed with Jade 8 software. Initial guesses for a, b, c and γ were taken from thin-film XRD and single crystal ED. The a and b crystallographic axes were assigned the measured spacings from ED (1.1 nm and 0.4 nm, respectively), while the c axis was assigned to the long spacing determined by thin film XRD for that particular material (3.0 and 3.9 nm). Given those axis assignments, the angles measured from ED were used as the initial values for γ: 90° for C8 and 92° for C12. α and β were assumed to be 90°.

Peaks in the powder XRD patterns were then assigned to the indices of the closest

match from the calculated peaks. Based on the measurements of γ, C8 was assumed orthorhombic. All peaks were matched to a reasonable (hkl), so lower symmetry lattices were not considered. Based on measurements of γ, C12 must possess a monoclinic or triclinic lattice. As all peaks were matched to reasonable indices assuming monoclinic, a lower symmetry lattice was not considered. After assignment of (hkl) to all peaks in range, the numerical values of the lattice parameters were refined from their initial values using the least-squares method provided in Jade.

Symmetry for these crystals was refined using all available diffraction data. For C12, centered space groups were eliminated as even $h+l$ peaks were not absent from thin film/powder XRD. $P2_1$ space groups were also eliminated as ED and XRD did not show $(h00)$, $(0k0)$ or $(00l)$ absences. $P2/b$ was ruled out as the $(hk0)$ points show no absences in ED. $P2$, Pm and $P2/m$ are all consistent with collected data. Single crystal data along other zones is necessary to further refine the space group for C12.

For C8, A, B and C space groups were ruled out as no absences were observed for the relevant two index sums, which also requires the elimination of F space groups. I space groups were also eliminated since (for example) (110) peaks are not absent in ED. These refinements also rule out all n glides. Space groups including 2_1 symmetry were excluded as $(h00)$, $(0k0)$ and $(00l)$ show no systematic absences. The lack of systematic absences in $(hk0)$s in ED and $(h0l)$s in thin film XRD rules out all glide plane space groups, leaving $P222$, $Pmm2$ and $Pmmm$. ED patterns show $I(hk0) = I(\bar{h}k0) = I(h\bar{k}0) = I(\bar{h}\bar{k}0)$, consistent with all three space groups. Without single crystal data along other zone axes, the C8 space group cannot be further refined.

2.4.4 Molecular Modeling

Atomic positions within best-fit unit cells were predicted through use of Cerius2 software. The COMPASS force field was used for all calculations. Individual C8 and C12 molecules were first minimized using the COMPASS force field to find the mini-

mum energy configuration. Two C8 or C12 molecules were placed inside the proposed unit cell and the system was allowed to reach the minimum energy configuration. The unit cell parameters were held fixed throughout all simulations.

2.4.5 Thin Film Deposition

Films for XRD and SEM were deposited by drop casting. 0.1% by weight solutions of C8 or C12 in toluene were made at modest temperature (≈40 °C) to ensure complete dissolution. Films were cast on cleaned glass coverslips in ambient atmosphere. Evaporation rate—and thus crystal size and habit—was controlled for C8 samples by reducing or enlarging the openings in the deposition chamber.

C8 suspension crystallization samples were made by allowing the deposition solution to cool to room temperature and sit undisturbed for a period of 6 hours. The resulting mixture of dilute T5 solution with suspended T5 crystals was then deposited on glass coverslips and allowed to dry quickly in ambient atmosphere.

For ED, single drops of solution were deposited on amorphous carbon-coated, copper TEM grids and left undisturbed for 30 seconds. Excess solution was then wicked off the grid with filter paper. Solution remaining on the grid was dried at room temperature in ambient atmosphere. No post-deposition processing steps were implemented.

2.4.6 Optical Microscopy

Polarized optical microscopy (POM) was conducted using a Nikon OPTIPHOT2-POL polarized optical microscope with a Spot2 RT Color digital camera. The instrument was calibrated prior to use with a reticle.

2.4.7 Scanning Electron Microscopy

SEM imaging was conducted using an FEI Quanta 200 3D environmental scanning electron microscope (ESEM)/FIB. Drop-cast samples were examined in environmental mode (20 torr water vapor) with no conductive coating. Images were captured at 7.5 kV.

2.4.8 Thin Film X-ray Diffraction

Thin film XRD was conducted using a Bruker D8 Discover with a 500 µm monocapillary collimator and HI-STAR 2D detector. The incident beam angle was fixed at 4° for all experiments. The detector was held at a fixed 10° with a camera length of 15 cm. The instrument was calibrated with a NIST1976 (corundum) flat plate standard prior to use.

2.4.9 Electron Diffraction

TEM and ED of C8 and C12 were conducted using a JEOL 3011 TEM operated at 300 kV and a camera length of 80 cm. Diffraction patterns were calibrated using gold (111) spacings. Measurements of d spacing and γ were performed using ImageJ software.

2.5 Acknowledgements

Dr. José Azurdia is acknowledged for his assistance in powder diffraction analysis. The financial support of NSF DMR-0320740 and DMR-0315633 is also acknowledged.

CHAPTER III

Thermotropic Phase Transitions of Alkyl-Substituted Pentathienoacenes

3.1 Introduction

Materials exhibiting LC phases are promising for use in TFTs. While the LC phases often exhibit poor performance compared to solid phases of the same material (*Funahashi and Hanna*, 2000), LC phases often display ambipolar transport (*O'Neill and Kelly*, 2011) and shallow trapping (*O'Neill and Kelly*, 2003). Such observations provide a means to further study the relationship between structure and transport. Additionally, key aspects of these LC textures can be retained when cooled to solid phases, a process termed paramorphosis (*Wiegeleben and Demus*, 1988). Thus processing routes passing through liquid crystal phases are appealing not just for the study of charge transport, but also for application in devices.

While methods have been demonstrated that permit control over crystal texturing at deposition (*Chen et al.*, 2001; *Swiggers et al.*, 2001; *Chou and Cheng*, 2004), LCs offer more flexibility. Due to their relaxed ordering conditions, LCs organize into large domains, with orientation that can be determined by POM, and—in many cases—controlled by the application of electromagnetic (EM) fields (*Dierking*, 2003). These properties have been harnessed to produce solid, monodomain TFTs exhibiting

a 10× increase in mobility over as-cast devices (*van Breemen et al.*, 2006). With their combination of order and fluidity, LC phases also present ideal conditions for annealing. Recent results (*McCulloch et al.*, 2006) show annealing in LC phases can produce dramatic increases in crystallinity and performance.

3.1.1 Chapter Overview

In this chapter, structural characterization of the elevated temperature phases of C8 and C12 is discussed. The first phase transition, elicited by both materials, is a so-called "side chain melting" transition. In this transition, the alkyl substitutions of both materials soften, resulting in a contraction of the unit cell along [001]. While such transitions have been observed in other materials, the unique chemical and crystalline structure of these substituted T5s—with substitutions stacked rather than interdigitated—results in a dramatic reduction in the c lattice parameter during this phase transition. This change in turn results in profound changes to crystal morphology as existing crystals attempt to accommodate such large molecular reorganizations.

This unique phase behavior, however, presents several problems for the use of these T5s in TFTs. The low onset temperature of this phase transition—85 °C for C8 and 95 °C for C12—may result in unwanted structural changes as post-deposition fabrication steps are employed. Additionally, annealing of either T5 in the liquid crystal phase is complicated by this phase behavior: the residual stresses that develop as these materials cool from the melt can cause violent cracking. Methods to reduce these stresses are necessary for successful implementation of annealing steps in device fabrication.

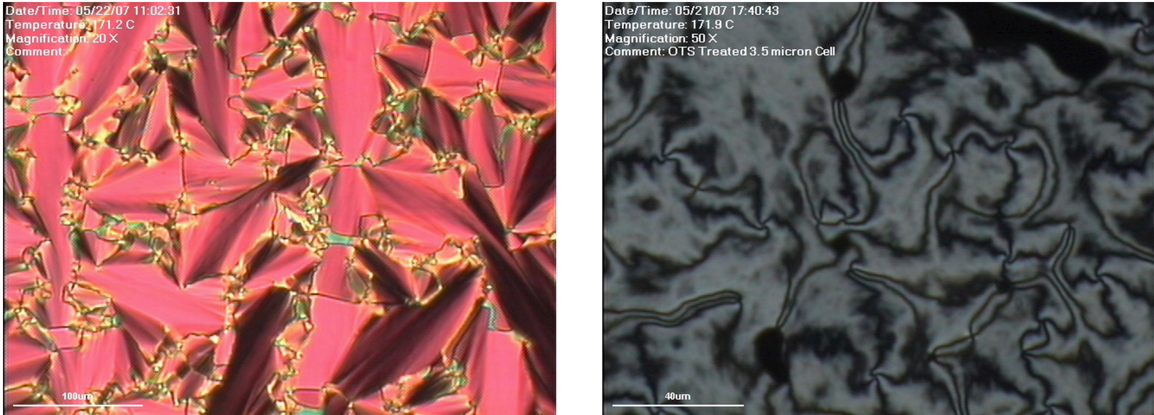

Figure 3.1: C8 exhibiting the fan texture (left) in a planar alignment cell and Schlieren texture (right) in a homeotropic alignment cell. The combination of these two textures identify this phase as smectic C

3.2 Results & Discussion

3.2.1 Liquid Crystal Texture Identification

A characteristic micrograph of C8 in a planar alignment cell at 171.2 °C is provided in Figure 3.1. This texture is the fan texture. A characteristic micrograph of C8 in a homeotropic alignment cell at 171.9 °C is also provided in Figure 3.1. This texture is Schlieren; defect strengths of $|S| = 1$ exclusively were observed. These two textures—Schlieren for homeotropic molecular alignment and fan for planar molecular alignment—indicate this phase of C8 is smectic C. Previous studies on dioctyl-substituted terthiophenes—which differ from C8 only by the absence of the sulfur bridges on the 2nd and 4th rings—indicate such molecules also exhibit smectic C phases (*Byron et al.*, 1995). Evidently, the additional rigidity of the thienoacene core does not inhibit the formation of the smectic C phase. However, it is interesting—and perhaps expected—that the transition temperature for C8 is markedly higher than for dioctyl-terthiophene.

A characteristic micrograph of C12 between untreated glass plates at 157.8 °C is provided in Figure 3.2. The observed texture is Schlieren; defect strengths of $|S| = 1$

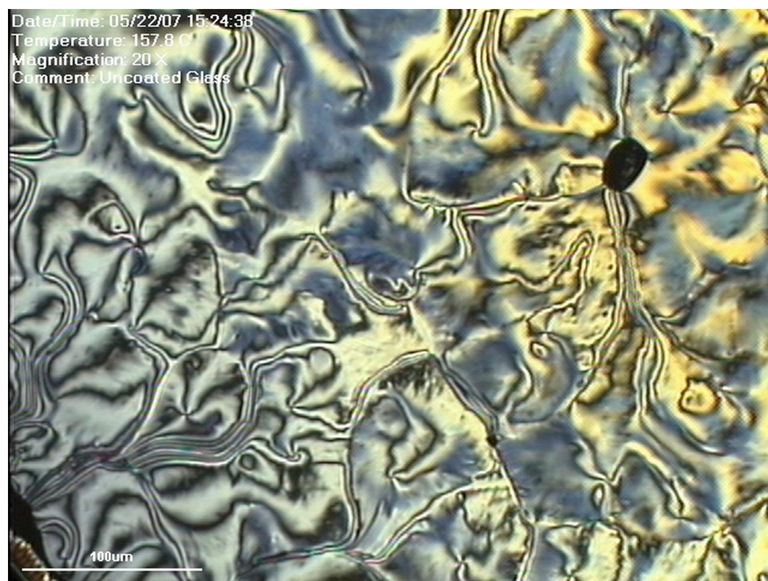

Figure 3.2: C12 exhibiting the Schlieren texture in a cell with untreated glass. Disclinations of strength $|S| = 1$ exclusively are observed, identifying this phase as smectic C.

exclusively were observed. This micrograph indicates the observed phase of C12 is also smectic C. These phase identifications—as well as those for C8—were corroborated with variable temperature X-ray diffraction (VT-XRD) in Sections 3.2.3 and 3.2.4.

3.2.2 Ferroelectricty

When subjected to a triangular voltage wave, the smectic C phase of C8 in the planar alignment cell shows only evidence for polarization of the C8 molecules and no evidence of ferroelectricity (Figure 3.3). This result agrees with the prior smectic C phase identification, as smectic C should exhibit no ferroelectric response. When these experiments are repeated above the clearing temperature, solely molecular polarization behavior is observed.

3.2.3 C12 High Temperature Crystallography

VT-XRD data obtained from C12 are provided in Figure 3.4. At room temperature, the ring at low q corresponds to a spacing of 3.89 nm, the (001) lattice spacing.

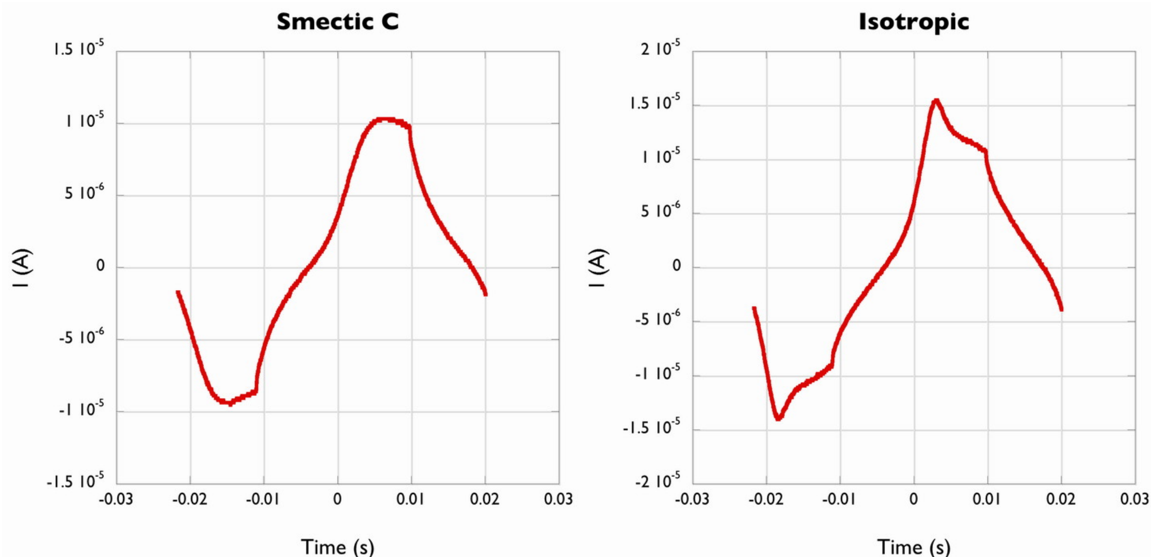

Figure 3.3: Polarization of C8 in the smectic C phase (left) in planar alignment and as an isotropic melt (right). Both show only molecular polarization response and no indication of ferroelectricity, consistent with the smectic C identification.

When heated to a temperature of 95 °C, a solid-state phase transition is observed. The most prominent feature of this transition is that the new $(00l)$ peaks have a q that is greater—and thus a d-spacing that is *smaller*—than observed in the room temperature data. The new (001) peak corresponds to a d-spacing of 3.00 nm—a 22.9% decrease from the room temperature phase.

Given the unit cell proposed in Chapter II, and its supporting diffraction data, these data indicate one of two possible structural changes at elevated temperatures. One possibility is that the C12 molecules interdigitate. Given the close packing of substitutions in the ab plane at room temperature, however, interdigitation seems energetically unfavorable. Another possibility is that the alkyl substitutions—likely all *trans* at low temperatures—develop *gauche* defects at elevated temperatures. The introduction of *gauche* defects into the substitutions would decrease their end-to-end distance, resulting in a contraction of the unit cell along the c axis.

Substantiation of the *gauche* defect mechanism can be found in the literature.

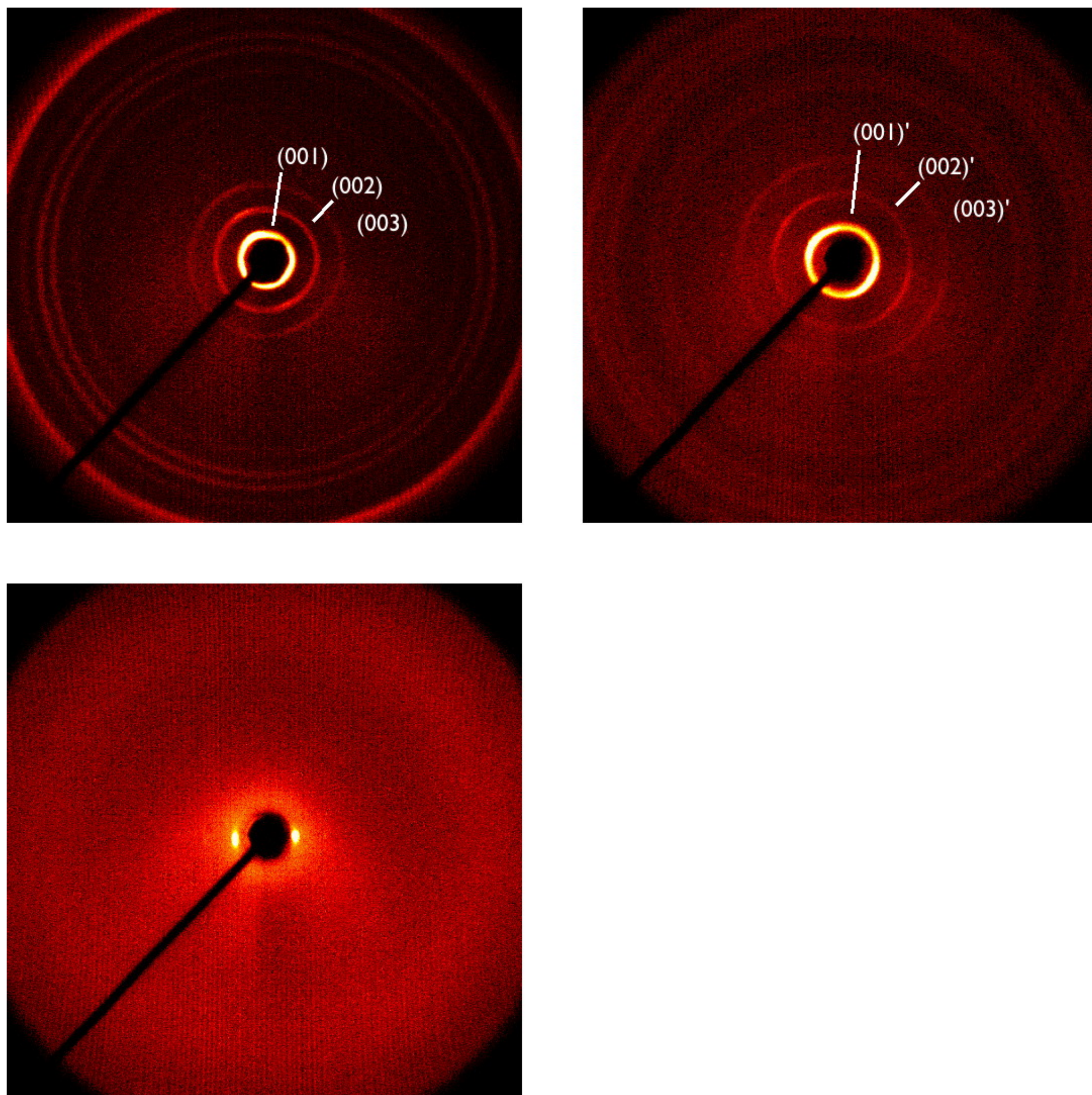

Figure 3.4: VT-XRD of C12 at room temperature (upper left) with c = 3.89 nm, at 95°C (upper right) after the "side chain melting" transition with c reduced by 22.9%, and at 160 °C (lower-left) in the smectic C phase with 3.20 nm layer spacing

Curtis et al. (2007) found that crystalline alkyl-substituted bithiazole oligomers exhibit a similar phase transition in which the relevant unit cell parameter decreases at the transition temperature. Further investigation of this transition revealed that room temperature crystals contain predominantly *trans* conformation substitutions, with a sharp increase in *gauche* concentration at the transition temperature. However, the data also indicate liquid-like mobility is not conferred onto these substitutions until the overall material melting temperature. The picture that thus emerges is an ordered phase with significant disorder—in the form of *gauche* defects rather than true fluidity—localized in the sidechains.

In addition to substitution disorder, materials exhibiting similar transitions show evidence for disorder in the ostensibly rigid cores. For example, the previously discussed bithiazoles, as well as poly(3-hexyl thiophene) (P3HT), show evidence of main-chain torsion at and above transition temperatures (*Yang et al.*, 1996; *Yazawa et al.*, 2006). While measurable, the core disorder in these materials is not so great as to destroy crystallinity until the material melting temperature is reached. In C12, by contrast, the fully aromatic core inhibits the formation of twist defects and relegates intramolecular disorder to the substitutions. This transition bears a great deal of similarity to the electron flux induced transition detailed in Chapter IV, where these connections are discussed further.

Heating the sample to 160 °C—inside the temperature window of the smectic C phase identified by optical methods—results in another phase transition. In this phase, all of the high q diffraction peaks have disappeared, leaving only two spots of equal q. The resulting structure is then clearly one of ordered layers with no long-range ordering beyond the layer spacing: an LC smectic phase. This layer spacing has a spatial period of 3.20 nm—shorter than the original c axis of C12, but still clearly along the molecular long axis. On its own, these data indicate either a smectic A or smectic C phase. However, coupled with the observation of an exclusive $|S| = 1$

Schlieren texture *via* variable temperature polarized optical microscopy (VT-POM)—or any Schlieren texture at all—these data clearly indicate this phase to be smectic C.

3.2.4 C8 High Temperature Crystallography

VT-XRD data obtained from C8 powder are provided in Figure 3.5. The ring at low q in the room temperature data corresponds to a spacing of 3.05 nm, the (001) lattice spacing. The remaining rings are not easily interpretable; diffraction rings for both (002) and (003) are clearly present, but a number of other peaks are as well. These rings do not fit the unit cell described in Chapter II—even considering all available (hkl)s, but can be identified simply by first examining the XRD results at elevated temperature.

When heated to a temperature of 85 °C, a solid-solid phase transition occurs. At this temperature, the same rings are present as at room temperature, but at very different intensities. Some peaks—namely the $(00l)$ peaks from the room temperature data—decrease in intensity, while others—the previously unidentifiable peaks—increase in intensity. Figure 3.6 depicts this change. These data show that the complex diffraction pattern observed at room temperature is actually composed of both the diffraction pattern of the room temperature phase—characterized in Chapter II—and the diffraction pattern for the phase stable at 85 °C. As was observed in VT-XRD of C12, C8 undergoes a phase change in which its substitutions disorder through development of *gauche* defects. This conformational change results in a contraction of the unit cell along the c axis. The difference between the C8 and C12, however, is that both the room temperature and high temperature ($T \geq 85$ °C) phases are present initially in the C8 samples studied.

As can be seen in Figure 3.6, the first peak is clearly (001), the room temperature c lattice parameter. The intensity for such a peak is quite high at room temperature

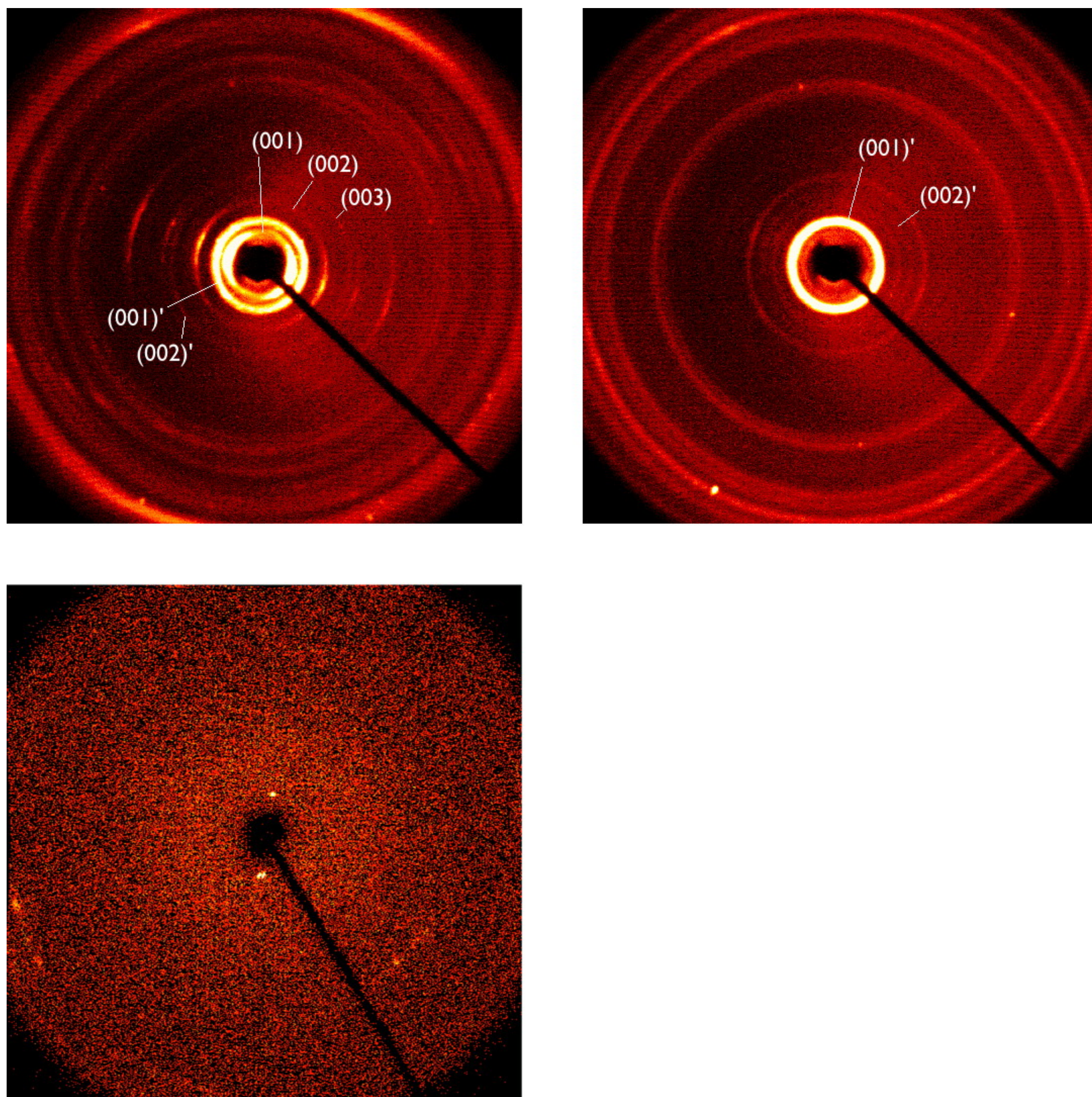

Figure 3.5: VT-XRD of C8 at room temperature (upper left) exhibiting the room temperature and frozen-in elevated temperature phase, at 85 °C (upper right) after the "side chain melting" transition and loss of the room temperature phase and at 174 °C (lower left) in the smectic C phase with 2.63 nm layer spacing

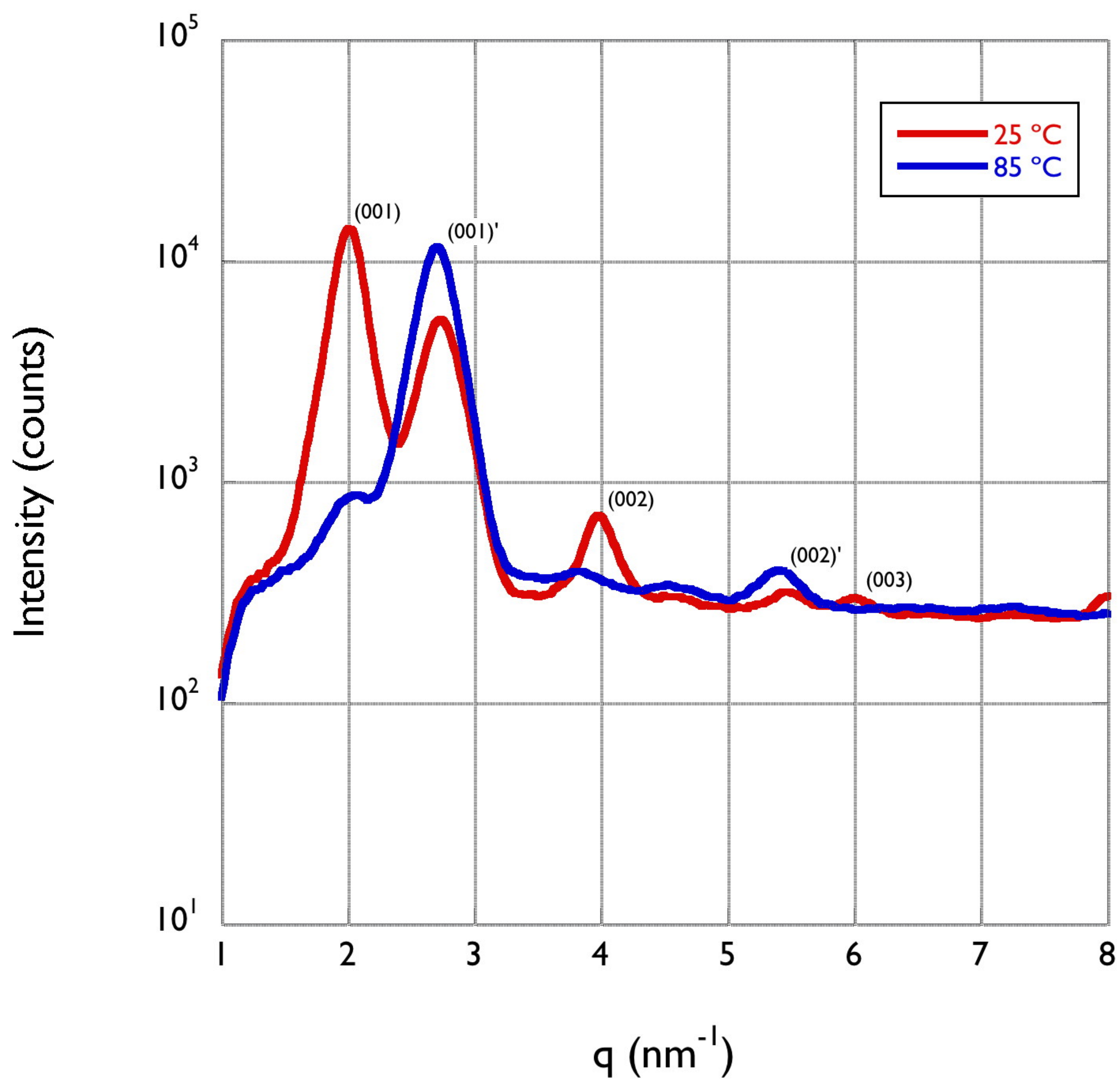

Figure 3.6: 1D VT-XRD of C8 before and after the “side chain melting” transition. The peaks corresponding to $(00l)$s reported in Chapter II all decrease in intensity above the transition temperature, while the intensity of the other peaks—the high temperature $(00l)$s—increase above this temperature

and reduced (nearly to background) as the sample is heated past the transition temperature. The second peak is $(001)'$, the high temperature c lattice parameter. At 2.27 nm, c' is 25.6% shorter than c. Also as expected, the intensity of the c' peak increases by more than a factor of 2 as the temperature is increased. This intensity change indicates the conversion of the initial room temperature phase into its high temperature variant.

Such analysis holds true for the other peaks observed in these data. The intensity of peaks at $q \approx 4$, 6 and 8 nm^{-1} (integral multiples of $q_{(001)}$) all decrease as the temperature is increased. These peaks are (002), (003) and (004) of the room temperature phase. Those of $q \approx 5.5$ and 8.25 nm^{-1} (integral multiples of $q'_{(001)}$) all increase as the temperature increases. These peaks are $(002)'$ and $(003)'$.

XRD of C8 cooled from the isotropic melt to a temperature of 174 °C confirms the smectic C phase identification previously made *via* optical means. The layer spacing measured from these data is 2.63 nm. As with C12, the layer spacing for the smectic phase is smaller than the original c axis spacing that preceded it, though larger than the c' spacing at elevated, but modest, temperatures.

3.2.5 Solid State Roughening Transition

The solid-solid phase transition—the "side chain melting" transition—also elicits unique changes in the optical appearance of substituted T5s. One would expect that—with a contraction of greater than 20% of the c lattice parameter—some macroscopic change must accompany the microscopic alterations. Such expectations are correct, as this phase transition produces significant, irreversible changes in film morphology.

Figure 3.7 shows polarized optical micrographs of the same C8 crystals prior to and after passing through the 85 °C temperature at which the unit cell contraction occurs. Figure 3.8 shows the same transition in C12. At this temperature, previously pristine, faceted crystals take on a rough, mottled appearance with the presence of

black streaks running throughout. This change is irreversible, however, as cooling past 85 or 95 °C again does not restore the blemish-free crystals: these morphological changes—at this scale—are permanent.

SEM of this same process is more revealing of the specific changes that occur. Figure 3.9 shows the same C8 crystals imaged prior to any heat treatment, as well as after heating past this transition temperature and returning to room temperature. Prior to any heat treatment, the crystals have sharp facets and nearly featureless faces. After the heat treatment, smooth surfaces become extremely rough while sharp corners are blunted or made ragged. Clearly the perceived roughening of crystals seen in POM was indicative of actual roughening of smooth crystal surfaces.

Such a transition has unfortunate implications for the use of top-contact electrodes for these substituted T5s in TFTs and other devices. The use of thermal evaporation to deposit metal electrodes on top of C8 or C12 crystals carries with it the risk of heating—localized or perhaps film-wide—past this relatively low transition temperature. This transition invariably introduces defects throughout a previously low-defect single crystal, potentially leading to significant trapping behavior at the sites of these defects. The morphological roughening may also be problematic at the contacts, where additional roughness could introduce unwanted contact resistance into the device. Top gating with a deposited dielectric on a roughened a surface would also be ill-advised, given the poor quality of the interface that would result. Bottom contact, bottom gate geometries are a much safer approach to fabricate devices from both of these materials.

3.2.6 Annealing

Annealing of C8 and C12 in the liquid crystal phase—a process known to improve performance in other materials (*McCulloch et al.*, 2006)—is fraught with problems. Figure 3.10 depicts C8 crystals heated through a phase sequence to clearing and

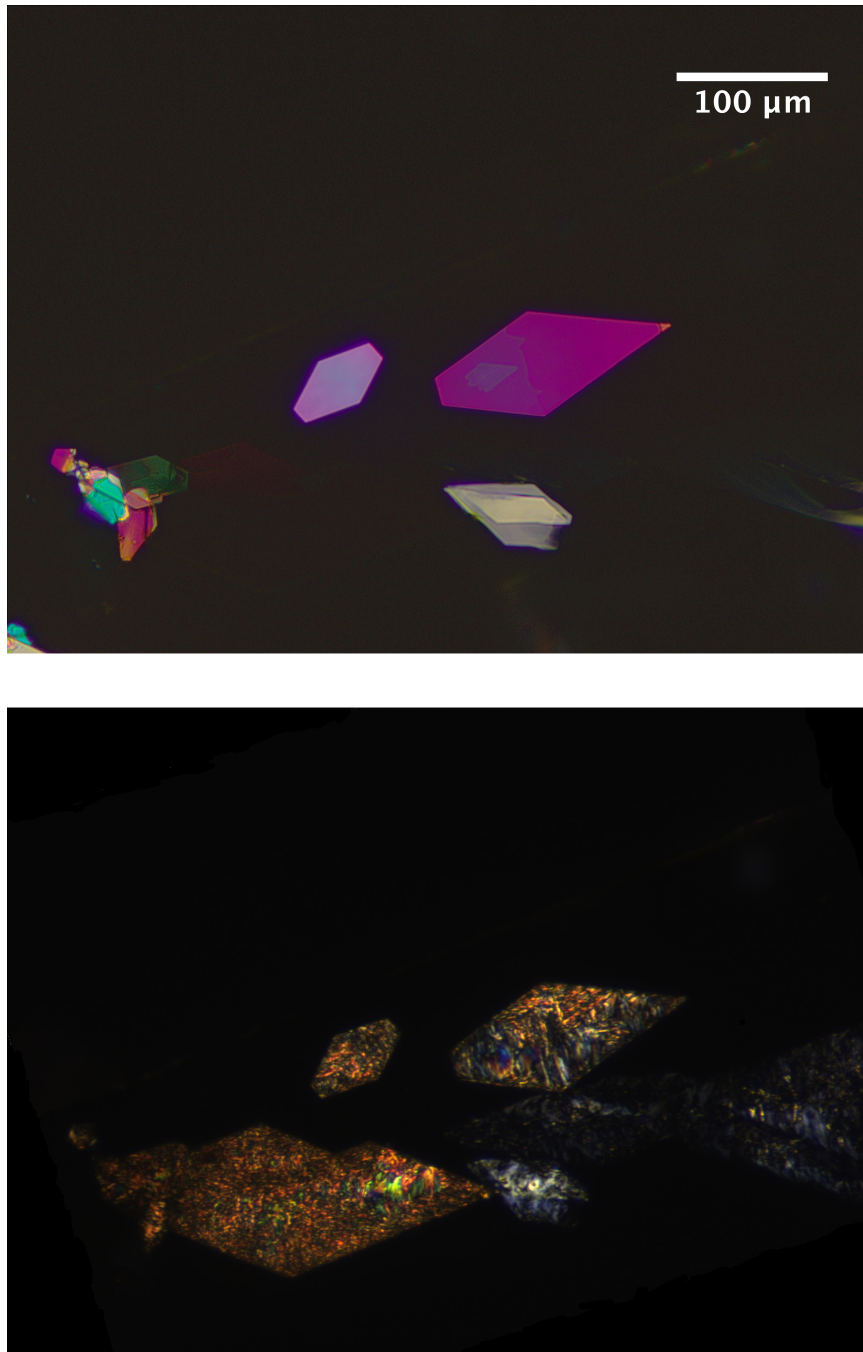

Figure 3.7: VT-POM of C8 crystals before (top) and after (bottom) macroscopic roughening induced by the unit cell contraction at 85 °C.

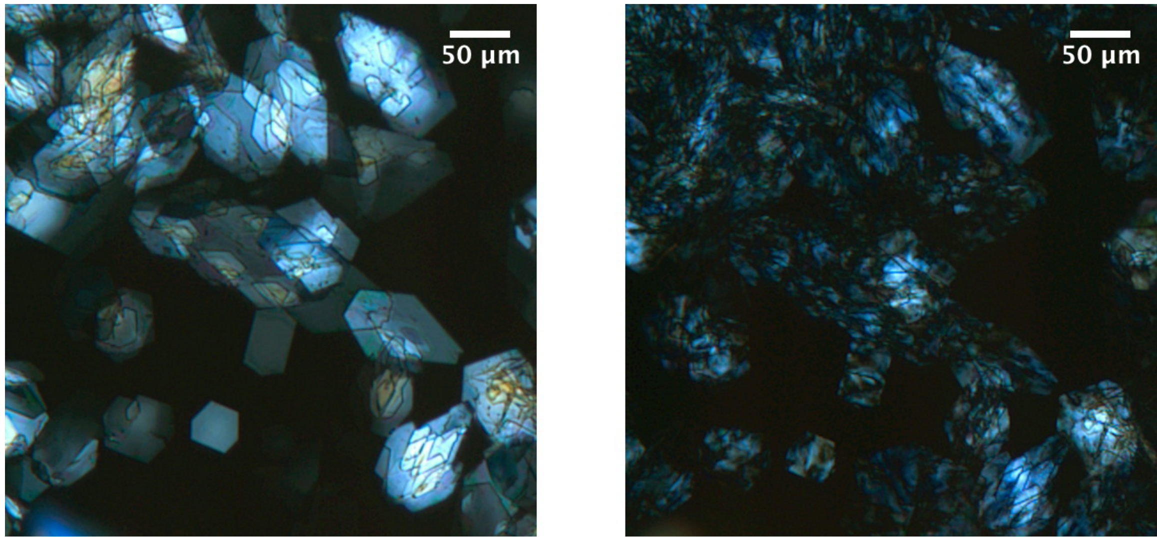

Figure 3.8: VT-POM of C12 crystals before (left) and after (right) macroscopic roughening induced by the unit cell contraction at 95 °C.

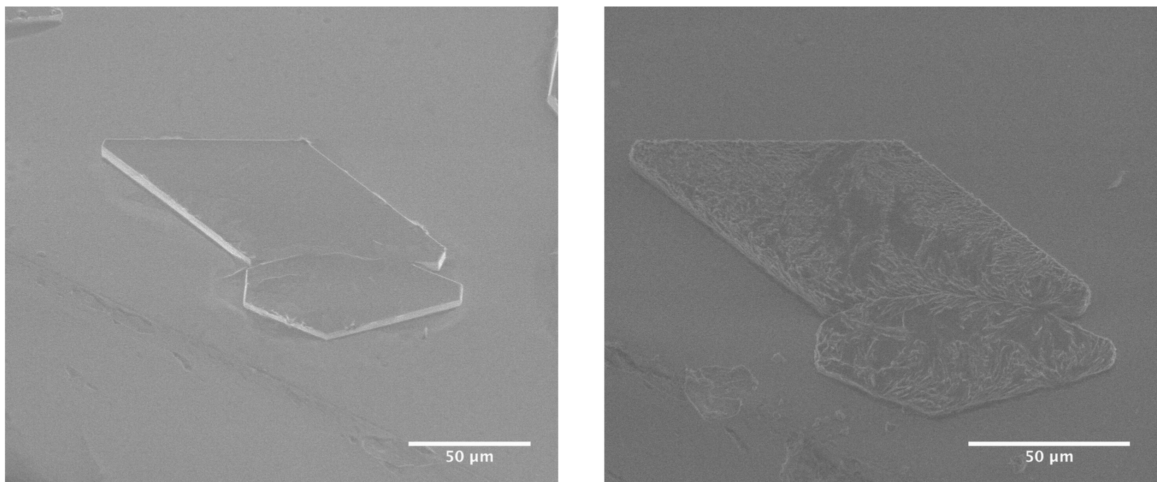

Figure 3.9: SEM of C8 crystals before (left) and after (right) macroscopic roughening induced by the unit cell contraction at 85 °C.

cooled to room temperature. While the heating process results in a film with greater coverage than the as-deposited, discrete crystals, huge cracks develop in the resulting films. In some cases, the cracking is so violent as to physically propel segments of the film distances of tens of microns.

Given what is known of the "side chain melting" transition observed in these materials, it seems the likely cause of the cracking. With the freedom of motion in the liquid phase, the T5 molecules reorder into large, continuous smectic C domains. These domains then solidify when the temperature is lowered and chain mobility of the substitutions decreases. At low enough temperatures, the substitutions cannot adopt the extended conformations energetically preferred due to the close packing established in the more fluid phases. Thus, significant stresses develop in these films. Such stresses, when sufficiently great, lead to cracking of the films.

This cracking makes annealing in an LC phase a dangerous proposition, given the high chances of complete device failure. The undamaged regions of the film still are sufficiently large to make single domain devices, though the location and propagation of these cracks is governed by no obvious macroscopic cue. It's a surprising finding that a rigid core/flexible substitution organic semiconductor like C8 or C12 would have this problem, considering the other similar materials—PBTTT for example (*Chabinyc et al.*, 2007b; *Zhang et al.*, 2010; *O'Neill and Kelly*, 2011)—that can be annealed with no such difficulty. One key factor that separates these T5s from those other similar materials, however, is that these T5 substitutions are not interdigitated.

In these other materials, the interdigitation of substitutions reduces the overall magnitude of unit cell contractions/expansions at phase changes. Figures 3.11 and 3.12 describe this schematically. Assume two hypothetical molecules, M_1 and M_2, with rigid centers and flexible substitutions. Let M_1 be the molecule with interdigitated substitutions (like PBTTT) and M_2 be the molecule with stacked substitutions (like C8 or C12). If given identical substitutions that contract by a distance δ at the

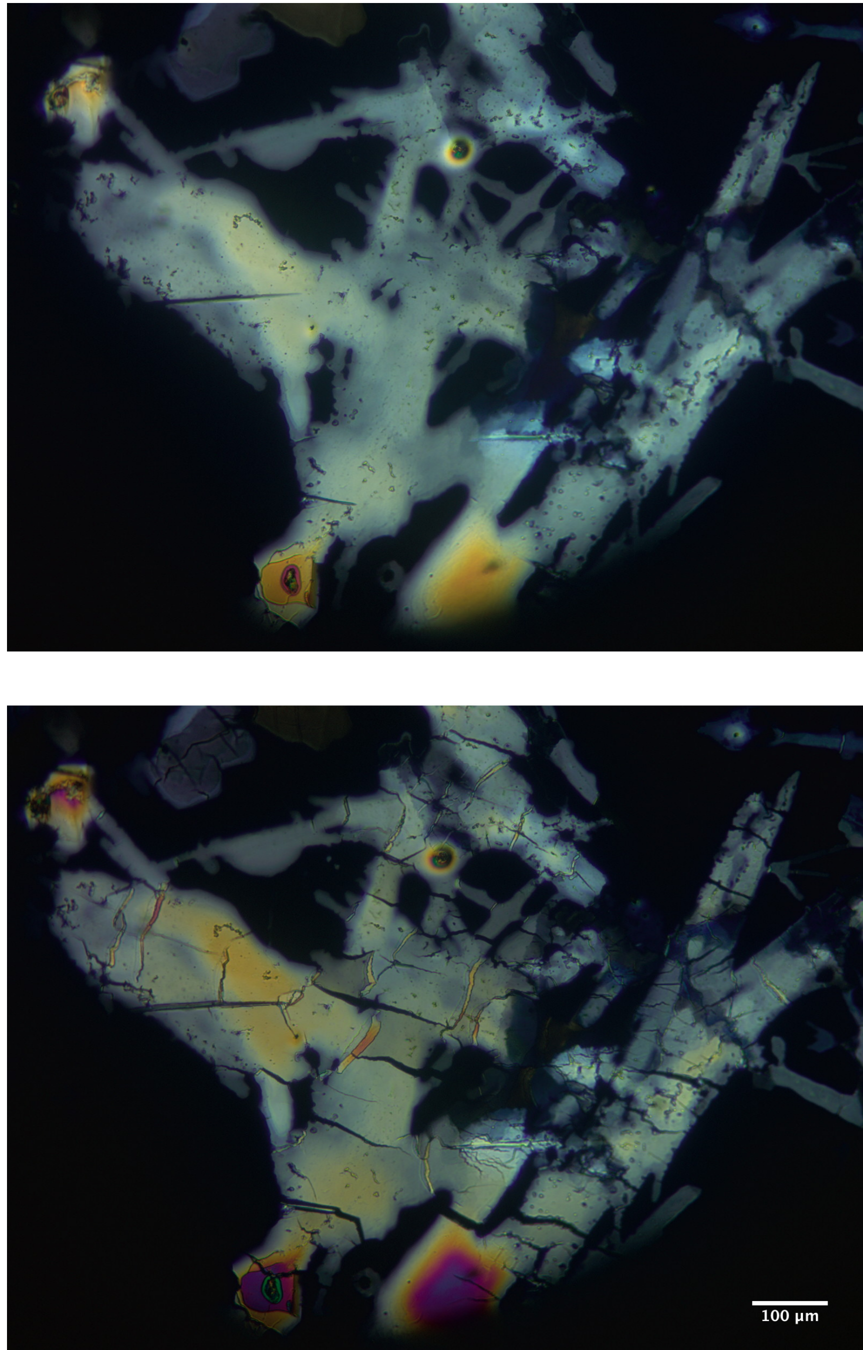

Figure 3.10: VT-POM of C8 showing the development of large cracks after cooling through the full phase sequence.

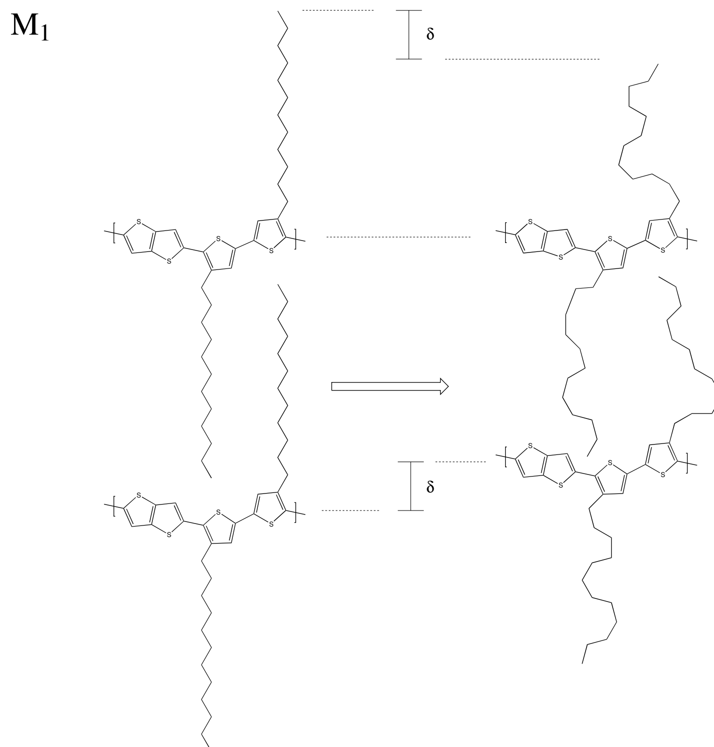

Figure 3.11: When interdigitated substitutions—such as those on PBTTT—contract by a distance δ, the unit cell contracts by δ

transition temperature, individual molecules of both M_1 and M_2 contract by a distance 2δ. However, the actual displacement of the solid cores of the molecules, and thus the overall unit cell contraction, is 2δ in M_2 but only δ in M_1. Smaller unit cell contractions result in lower stresses when returning to the extended state, and lower stresses lead to fewer—if any—issues with cracking.

3.3 Conclusions

VT-POM experiments reveal that both C8 and C12 form smectic C phases between 169–174 °C and 156–168 °C, respectively. The layer spacing for the smectic C phases was measured using VT-XRD. For C8, this spacing was measured at 2.63 nm; for C12, the layer spacing was measured at 3.20 nm.

VT-XRD experiments also indicate that both materials undergo a solid-solid phase

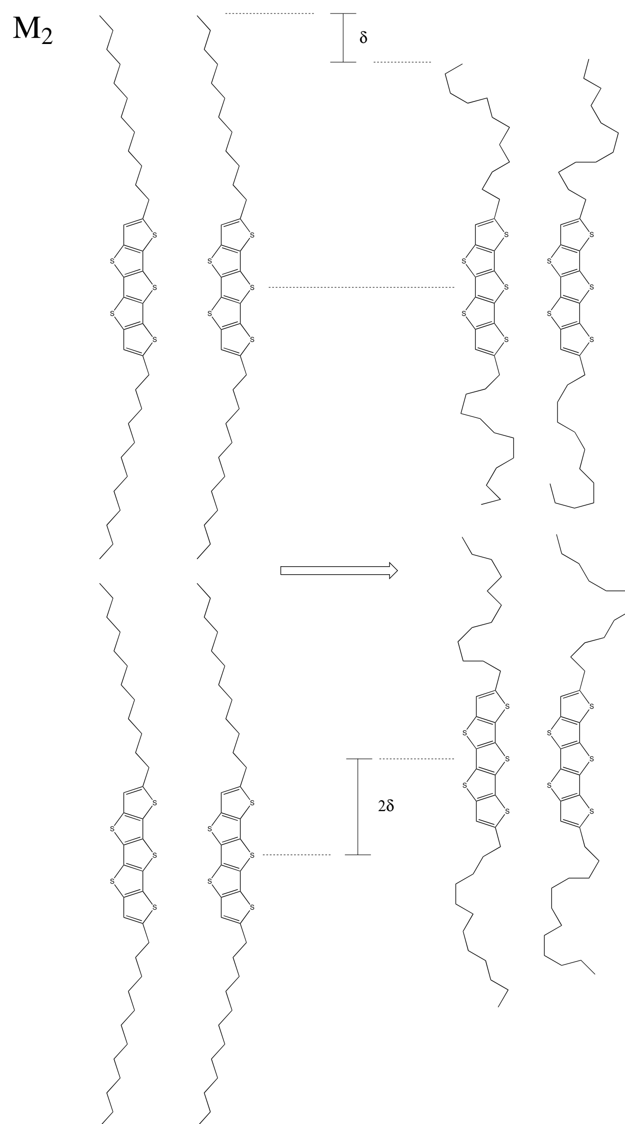

Figure 3.12: When stacked substitutions—such as those on C8 or C12—contract by a distance δ, the unit cell contracts by 2δ. This substitution stacking explains the large unit cell contraction exhibited by C8 and C12 and likely explains the cracking behavior

transition at elevated temperatures. These transitions occur at 85 °C for C8 and 95 °C for C12. This transition results in a contraction of the *c* lattice parameter from 3.05 nm to 2.27 nm for C8 and from 3.89 nm to 3.00 nm for C12—a decrease of 25.6% and 22.9%, respectively. Given the molecular orientation within the unit cell—both molecules aligned along [001]—this lattice contraction is the result of a process frequently—but perhaps erroneously—termed "side chain melting." As the temperature increases, alternate bond conformations become available to these substitutions, resulting in a shorter head-to-tail distance and the observed reduction in lattice parameter.

Such dramatic changes in unit cell parameters are due to an important detail that sets substituted T5s apart from other materials: the substitutions are attached at the ends, rather than the center, of the molecules. With these attachment points, there is no room for the substitutions to interdigitate like the substitutions on, for example, various substituted poly(thiophenes). With no interdigitation, the unit cell of C8 or C12 will necessarily contract twice as much as a poly(thiophene) with the same substitution length.

This unit cell shrinkage is responsible for additional—and unfortunate—morphological changes. Due to magnitude of the unit cell change, seemingly pristine single crystals that pass the transition temperature lose facets and sharp edges, while presumably developing significant defect concentrations. This limits the processing steps that can be employed after T5 deposition, as such a transition would severely hinder charge transport. The magnitude of this change also complicates annealing as a processing route to superior device geometry, as the molecular expansion when the phase sequence is reversed produces huge cracks that could result in complete device failure.

While C8 and C12 show complex and interesting phase behavior, their use in TFTs or other thin film devices is likely relegated to the large, single crystals easily formed from solution casting.

3.4 Materials & Methods

3.4.1 Materials

C8 and C12 were examined in these studies; synthesis of both is described elsewhere (*Zhang*, 2006). Materials were used as-received after the final sublimation purification step described in *Zhang* (2006). Toluene (ACS Reagent grade, ≥99.5%) was used as-received from Sigma-Aldrich.

3.4.2 Liquid Crystal ID *via* Variable Temperature Polarized Optical Microscopy

Optical texture identification of liquid-crystalline mesophases was performed using an Olympus BX60 POM. Sample heating was accomplished through use of an INSTEC STC200F heating stage flushed with dry nitrogen gas. Alignment cells were utilized to aid in texture identification. C8 samples were examined in homeotropic and planar alignments, produced in cells having octadecyltrichlorosilane (OTS) and rubbed polyimide on indium tin oxide (ITO) coatings, respectively. The OTS cell was fabricated with a gap of 3.5 µm; the rubbed polyimide cell was fabricated with a gap of 5 µm. C12 samples were investigated between cleaned, uncoated glass with no control over the cell thickness.

Sample powders were positioned at the open edge of alignment cells inside the heating stage. The stage was subjected to a constant purge of dry nitrogen gas. Samples were heated quickly (≈ 10 °C/min) to clearing and cells were filled *via* capillary action. Samples were then cooled slowly (≤2 °C/min) into the phase of interest as identified by differential scanning calorimetry (DSC) (*Zhang*, 2011). The phases of C8 existing between 169–174 °C and 152–169 °C were examined in these experiments. The phase of C12 existing between 148–165 °C was also examined.

3.4.3 Ferroelectricity

C8 in the planar alignment cell was examined for the presence of ferroelectricity. At a temperature of 172.8 °C, as well as above clearing, the cell was subjected to a 24 Hz triangular wave with 25 V amplitude and another with 40 V amplitude. The input was produced by an HP 33120A function generator. The resulting voltage across a 20 kΩ resistor in series with the alignment cell was monitored with an HP 54600B oscilloscope.

3.4.4 Variable Temperature X-ray Diffraction

Thin film XRD was conducted using a Bruker D8 Discover with a 50 µm mono-capillary collimator and HI-STAR 2D detector. Data were collected in transmission geometry. The instrument was calibrated with silver behenate powder prior to use. Due to the small temperature windows for many C8 phases, the details of data collection differ for C8 and C12.

Samples for C12 VT-XRD were assembled in a nitrogen glove box. C12 powder was deposited in 2 mm OD glass capillaries with 10 µm wall thickness from the Charles Supper Company. Capillaries were sealed with epoxy and allowed to cure for 72 hours before removal from the glove box. Samples were used immediately after removal from the glove box.

VT-XRD was conducted at temperature through use of a modified heating plate. Details of the construction of this plate are provided in Appendix A. Temperature was raised slowly ($\approx$ 5 °C/min) to temperatures of interest (95 °C, 160 °C) from *Zhang* (2011). Samples were held at this temperature while data were collected. Samples were then heated to clearing and cooled back to temperatures of interest to verify observed structures were not the result of sample history.

VT-XRD of C8 samples was conducted in a sealed heating stage. 8 mm segments of the same capillaries used for C12 VT-XRD were filled with C8 powder and secured

inside a modified Linkam TH1500 heating stage. Details of the modification of this tool are described in Appendix A. Dry nitrogen gas was flushed continuously through the sample chamber at 0.5 L/min. Samples were heated at 10 °C/min to the temperature of interest (85 °C) and held there while data were collected. Samples were then heated to clearing and cooled into the phase of interest at 174 °C for collection of XRD patterns.

3.4.5 Side-Chain Melting *via* Variable Temperature Polarized Optical Microscopy

Samples for VT-POM of the "side-chain melting" transition of C8 and C12 were prepared by drop casting. 0.1% by weight solution of C8 in toluene was made at modest temperature (≈ 40°C) to ensure complete dissolution. Films were cast on cleaned glass coverslips in ambient atmosphere. Evaporation rate was severely limited—requiring approximately 8 hours for film formation—resulting in the formation of large single crystals. These C8 samples were also used for SEM.

VT-POM of C8 and C12 samples was conducted using a Nikon Optiphot POL-2 POM with a Spot2 RT Color digital camera. Samples were heated with a Linkam THS1500 sealed heating stage flushed with dry nitrogen gas at a rate of 0.5 L/min. Samples were heated at 10 °C/min and held at 110 °C for high temperature imaging. Samples were cooled to room temperature and examined for signs of the reversal of the roughening.

3.4.6 Scanning Electron Microscopy

SEM of C8 crystals was conducted before and after heat treatment. As cast-samples were imaged using an FEI Quanta 200 3D ESEM/FIB. SEM images were acquired in environmental mode (20 torr water vapor) with no conductive coating. Images were captured at 5 kV.

3.5 Acknowledgements

Dr. Myung-Su Kim and Professor Satyendra Kumar are acknowledged for their assistance in the preparation of samples for VT-XRD. The financial support of NSF DMR-0320740 is also acknowledged.

CHAPTER IV

Electron Flux Induced Phase Transitions of Alkyl-Substituted Pentathienoacenes

4.1 Introduction

The interactions of organic materials with high energy electron beams produce a broad range of effects (*Kumar*, 1990). Beyond the generation of EM radiation and secondary electrons, these interactions often drive damage processes in these materials (*Williams and Carter*, 1996). These damage processes typically take the form of either bond scission or knock-on damage. Bond scission in organic materials may also lead to the production of free radicals, which in turn crosslink to form new chemical structures. Diacetylenes, for example, well known for a solid-state polyermization reaction when exposed to appropriate (UV) light, have been shown to also polymerize when bombarded by high energy electrons (*Liao and Martin*, 1993).

Such interactions have been harnessed for useful purposes, especially in areas of micro- or nanofabrication. With the difficulties extending photolithography to sub-nm scales, many have turned to electron beam resists (*Finch and Vesely*, 1987; *Kuller et al.*, 2004). Such resists—like their photon-activated cousins—typically become soluble or insoluble under electron flux. The use of these materials transforms an SEM into a fabrication tool, as it is used to define patterns for subsequent deposition,

implantation, *etc.*

More recently, refinements to these sorts of processes have been developed which allow for SAMs to be selectively activated (*Golzhauser et al.*, 2000). With such procedures, chemical reactions can be given extremely precise spatial localization without need for resist processing or masks. This is especially beneficial for devices requiring complex geometries of relatively fragile organic species, as the active materials needn't be exposed to potentially damaging resist processing materials or methods.

This ready reactivity of organic compounds under electron flux comes with unfortunate consequences, however. At present, many of the most advanced structural characterization instruments (*i.e.* TEM and SEM) interrogate samples using electrons that activate the same processes previously discussed for fabrication purposes. When the goal is structural characterization, rather than chemical modification, these processes limit the extent to which susceptible organic materials can be characterized as samples are modified while being imaged. This is especially problematic for studies of crystalline materials, as crystallinity is lost rapidly under even modest high energy electron flux (*Martin and Thomas*, 1995; *Martin et al.*, 2005).

Between these two extremes are cases where these electron activated processes are both necessary and limiting. *Lovinger* (1985) has used the focused TEM beam to both produce and characterize a dielectric-to-ferroelectric phase transition in copolymers of poly(vinylidene fluoride) (PVDF) and poly(tetrafluoroethylene) (PTFE). Additionally, in the previously discussed diacetylene example (*Liao and Martin*, 1993), imaging of the phase change was only possible because the beam used for imaging simultaneously drove the phase change. In such experiments, these processes are necessary as they produce the novel phenomena of interest. They are, however, simultaneously problematic as they limit the detail of those observations due to the short lifetime of the features of interest under continued electron flux.

4.1.1 Critical Dose

The rapid loss of crystallinity by organic compounds severely limits our ability to characterize them thoroughly in the TEM or SEM. While typically rapid, the rate at which crystallinity is lost can vary tremendously from one material to another. This variability in resilience has been quantified in a number of ways, but one with particular utility—especially to microscopists—is critical dose (*Kumar*, 1990). Critical dose, denoted J_c or Q_c, is the fitting parameter determined by modeling the decrease in diffraction spot intensity as a decaying exponential in total dose, *i.e.*:

$$\frac{I_{(hkl)}(Q)}{I^0_{(hkl)}} = \exp\left(-\frac{Q}{Q_c}\right) \tag{4.1}$$

where $I_{(hkl)}(Q)$ and $I^0_{(hkl)}$ are the intensity of the diffraction spot (hkl) after a total dose, Q, and zero dose, respectively, while Q_c is the critical dose.

Critical dose, reported in charge per area, ranges from single mC per cm^2 for especially fragile crystals (*e.g.* poly(ethylene) (PE), PVDF) to as high as hundreds of mC per cm^2 for compounds such as Kevlar™, poly(p-phenylene-2,6-benzobisoxazole) (PBO) and Pn (*Drummy et al.*, 2002). Materials such as linear PE and Pn demonstrate prototypical behavior: linear compounds are especially vulnerable to beam damage while aromatic compounds are not. Materials with both linear and aromatic character—for example TIPS (*Chen*, 2006)—tend to exhibit intermediate critical dose behavior.

4.1.2 Chapter Overview

In this chapter, the complex and unique phase behavior of C8 and C12 under high energy electron flux is discussed. Under modest total electron dose, crystals of both materials undergo internal reorganizations that result in an increase in symmetry order. Specifically, the a axis in both C8 and C12 develops twofold screw symmetry.

Under continued dose, amorphization behavior for C8 and C12 diverge. While the fading of the diffraction patterns for both materials is well characterized by exponential decay—with comparable critical dose values for both—C12 amorphizes directly while C8 passes through an intermediately ordered phase. This intermediately ordered phase is very long-lived under continued flux with a critical dose approximately $3\times$ that of the prior phase.

The existence of this phase is likely due to the unique composition of substituted T5s. The substitutions—chemically identical to linear PE—are much more vulnerable to electron flux induced damage processes than the aromatic, T5 cores. The phase behavior under low total electron dose is thus the result of preferential degradation of the substitutions, with the resulting structures due to the order retained by the beam resilient, T5 cores.

4.2 Results & Discussion

4.2.1 Dynamic Diffraction of C8

Figure 4.1 demonstrates the fading of C8 diffraction patterns under a relatively high current density of ≈ 20 pA/cm^2. The first observable change in the data is the loss of odd ($h00$) peaks. The loss of these peaks indicates the a axis develops twofold screw symmetry. Especially interesting about this transition is that these electron flux induced degradation reactions increase the symmetry order of C8 crystals, rather than decrease it. Such an increase is not unheard of, however, as *Lovinger* (1985) observed increased diffracted intensity and decreased misorientation of crystallites of PVDF/PTFE under electron flux. This increase in order happens very quickly, requiring total doses of ≈ 10 mC/cm^2. The mechanism behind this symmetry development, however, is not entirely clear from these data.

One possible explanation is that the degradation of the substitutions induces

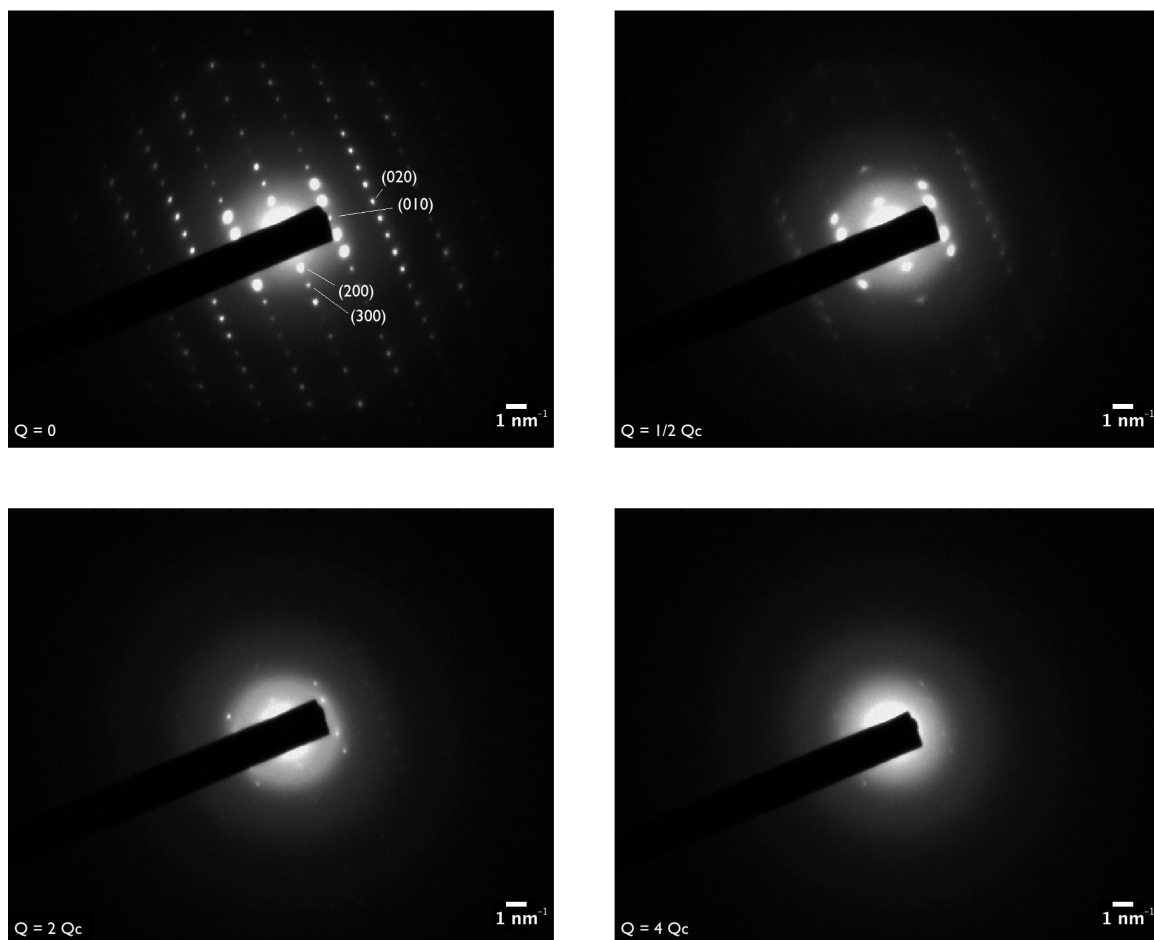

Figure 4.1: Characteristic fading behavior of ED patterns of C8 under electron flux. At zero dose, samples are highly crystalline with many diffraction spots. Under modest dose ($\approx$ 10 mC/cm^2), odd ($h00$)s disappear indicating formation of twofold screw symmetry on a. Continued exposure results in amorphization characterized by a critical dose of 15.2 ± 2.4 mC/cm^2, though this fading slows at $\approx$ 30 mC/cm^2. This intermediately ordered phase slowly amorphizes with a critical dose of 52 ± 15 mC/cm^2.

reordering of these crystals. Results discussed in Chapters II and III show how changes in the structure of these substitutions have profound effect on both crystal structure and morphology. Bonds within the substitutions will likely break after low electron doses, causing the remaining intact molecules—whether unsubstituted T5s or shorter/asymmetrically substituted T5s—to reorder.

This mechanism has additional justification in the structure of unsubstituted T5s. These materials—as published by *Zhang et al.* (2005)—natively show the same twofold screw symmetry exhibited by C8 only after modest electron dose. Simulated electron diffraction of unsubstituted T5 along [010]—the equivalent long molecular axis to [001] in C8—shows this same systematic absence (Figure 4.2). The damage processes in the substitutions perhaps lessen their influence on the overall packing of the T5 cores, leading to the adoption of a packing motif similar to the unsubstituted variant. It should be noted however, that the unit cell parameters of C8 after development of this symmetry (a and b) do not change to match those of their equivalents (a and c) in unsubstituted T5. The transformation to a similar structure is limited to the development of this symmetry.

An additional—or alternate—possibility is the removal of elements that break this symmetry in as-cast crystals. The dim-bright pattern to the ($h00$)s seen in the zero dose pattern in Figure 4.1 indicates that molecular packing in as-cast crystals approaches this symmetry. Perhaps the T5 cores posses this symmetry while the substitutions—and thus C8 crystals—do not. At a dose of 10 mC/cm^2, the substitutions—chemically no different than very short chains of linear PE—should have undergone significant damage. At 2.5× the critical dose of linear PE (*Kumar*, 1990), this total dose would reduce diffracted intensity of PE crystals to 10%. If, as supposed, the broken symmetry is due to the presence of crystalline substitutions, their amorphization would result in the observation of this symmetry using techniques such as ED.

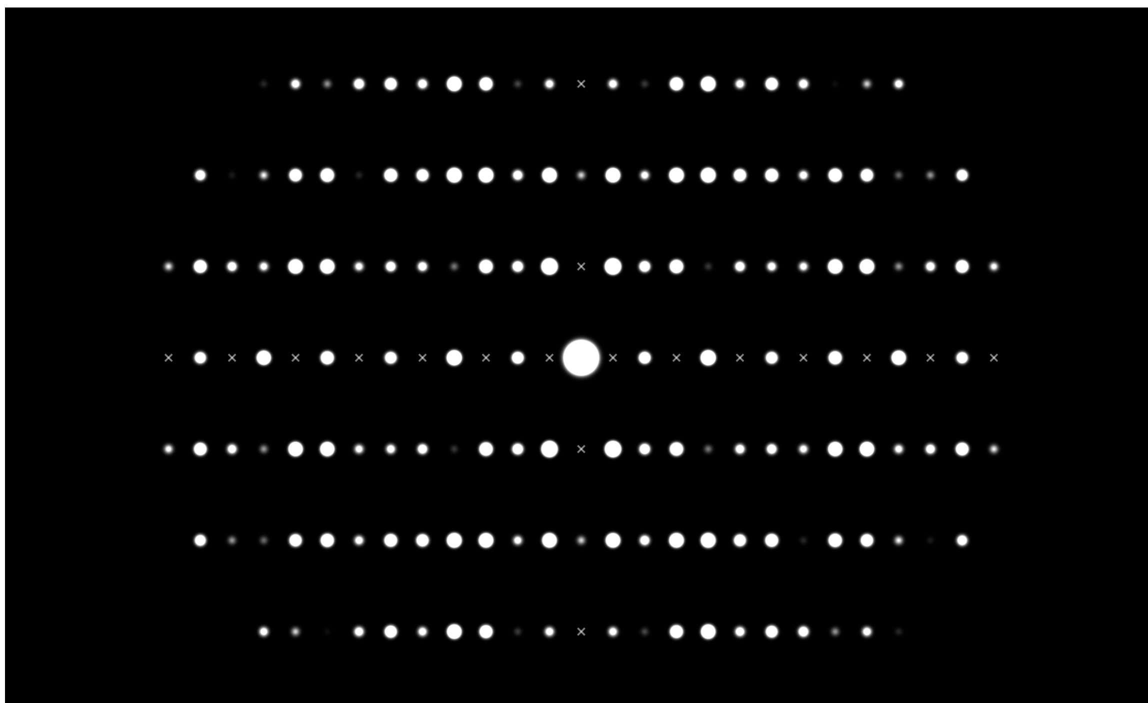

Figure 4.2: Simulated ED pattern of unsubstituted T5 from data published by *Zhang et al.* (2005). Systematic absences denoted by $\times$. Unsubstituted T5 exhibits the same twofold screw axis on the nominal edge-to-edge packing direction observed in C8 only after modest electron dose. Evidently, preferential degradation of C8 substitutions leads to adoption of symmetry possessed by the unsubstituted variant.

It is unclear from the data whether this observed symmetry order increase is due to internal reorganizations, selective amorphization of symmetry breaking elements or a combination of both. What is clear, however, is that the change is due largely to damage processes in the substitutions. At such low doses, the aromatic constituents of the T5 cores should show little—if any—damage.

The spots remaining after the development of the screw axis symmetry continue to fade with intensity vs. dose behavior closely matching the exponential decay model. The critical dose measured for this loss of crystallinity is 15.2 ± 2.4 mC/cm^2. Such a value is intermediate to observed critical doses for TIPS (*Chen*, 2006)—another rigid core/flexible substitution, crystalline, organic compound—and linear PE. After sufficient dose that all spots should clear ($\approx 4Q_c$), however, low index diffraction spots remain. At such elevated dose, little should remain of the substitutions, yet C8 is evidently able to retain some order.

It is important to make note of subtle details about the fading of the initial peaks. Figure 4.3 depicts the same transition, this time examined with a longer per-frame exposure time. The important details can be seen in the (400)s. These peaks first move to lower scattering angle, before suddenly giving way to a sharply defined peak at the original scattering angle. Such behavior is exhibited by other peaks as well, such as the various (h10)s, though the specifics of their scattering angle changes depend on the specific value of h. Measurements of γ show no change.

The translation of diffraction spots originates in expansion and contraction of the relevant unit cell parameters. Figure 4.4 details these changes as a function of dose. a_1, the a lattice parameter of the initial phase, expands continuously until rapidly fading, leaving behind a_2. a_2, the a lattice parameter of the residual structure, shows no further expansion or contraction. Similar behavior is seen from b, with b_1 continuously contracting before giving way to b_2 at higher dose. Just before disappearing, a_1 reaches a maximum value of 1.22 nm, a 6% increase. The contraction of b_1 to its

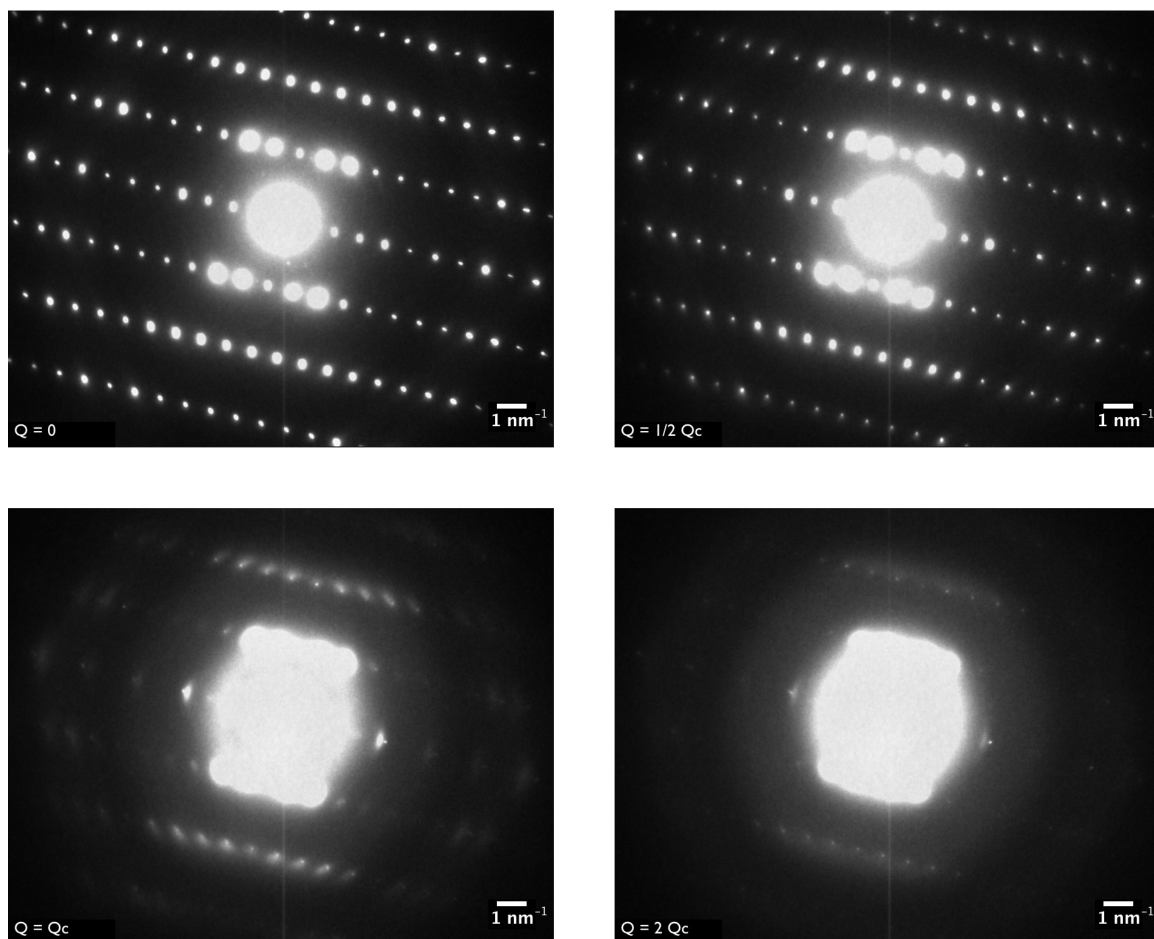

Figure 4.3: Electron-flux induced fading of C8 ED pattern with higher per-frame exposure time, showing the expansion of the lattice in a and the contraction in b. After sufficient dose ($\approx 2Q_c$), these large diffraction spots quickly fade away, leaving behind small, sharp spots. The sharp spots occupy nearly the same diffraction space locations as the original ($hk0$)s.

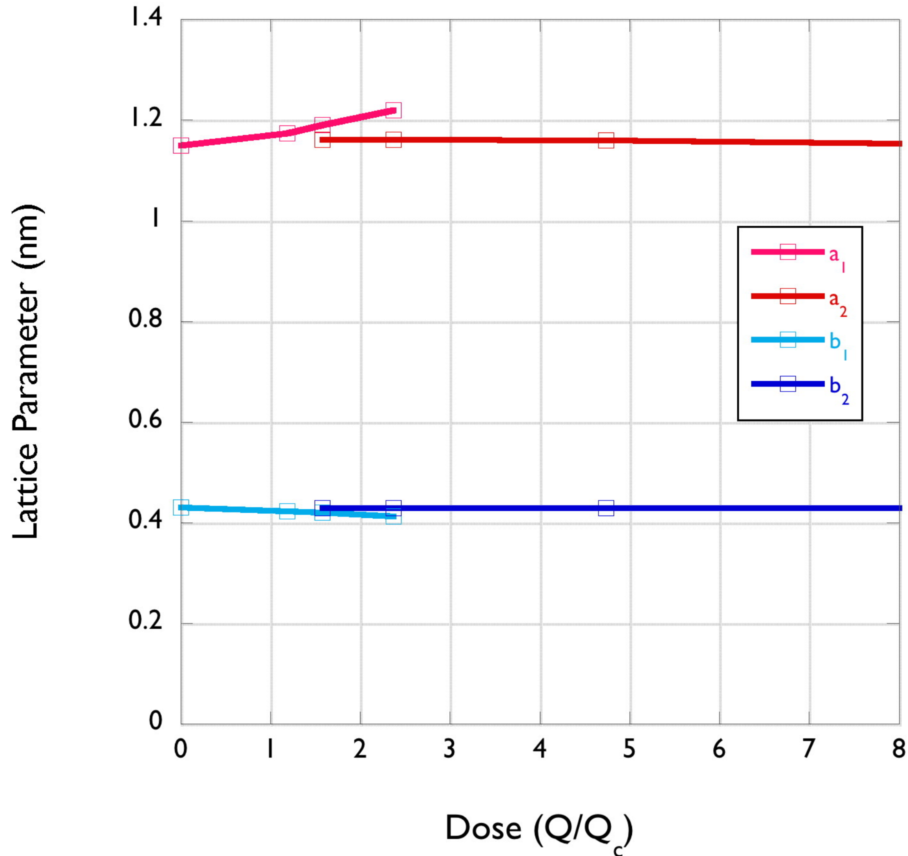

Figure 4.4: Lattice parameter values vs. electron dose for the initial phase (a_1 and b_1) and residual phase (a_2 and b_2). a_1 expands to a maximal value of 1.22 nm before fading as C8 converts to the next phase. b_1 contracts to a minimum of 0.41 nm before converting to the next phase.

maximal value—0.41 nm, a 4% decrease—occurs just before disappearing.

Looking closely at Figure 4.3 and 4.4, the sharp spots that remain after the lattice parameter expansions and contractions coexist—briefly—with the fading large spots. This implies a brief coexistence of the two phases. Intensity lost by the original, fading spots is replaced by intensity gains in the sharp, remaining spots. This occurs as C8 is converted from the expanded state characterized by the maximal a_1 and b_1 to the residual state described by the dose-insensitive a_2 and b_2.

These various new (110)s and (210)s from the residual phase display significantly slower intensity loss than the initial diffraction peaks. Measurements of the rate of in-

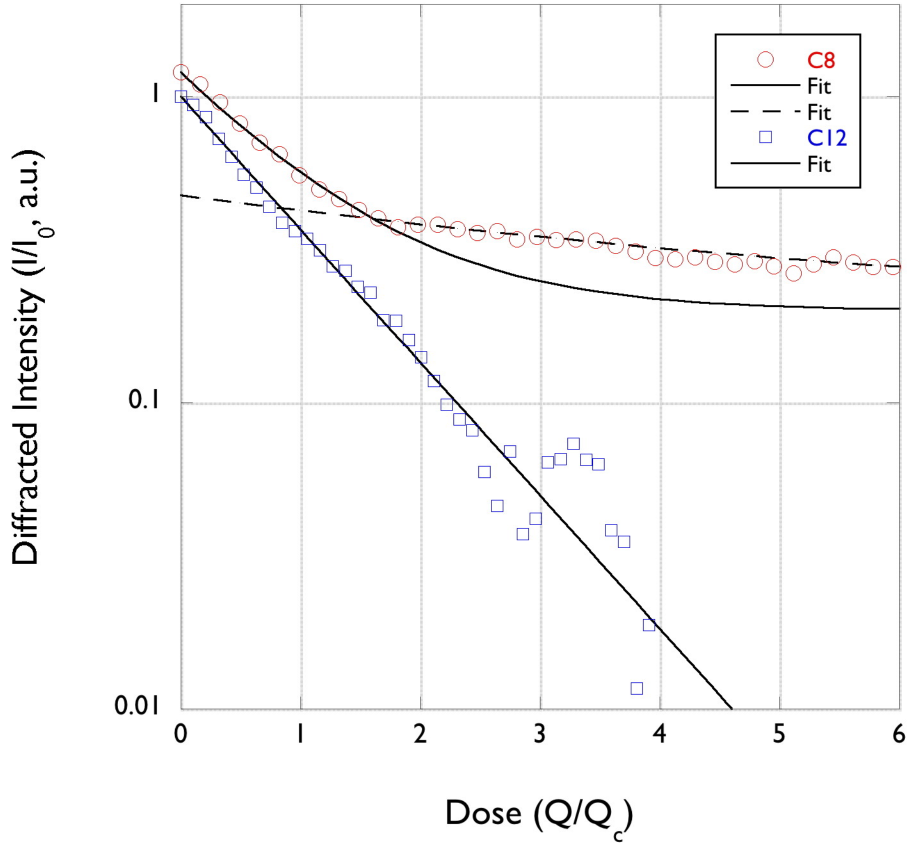

Figure 4.5: Normalized intensity ($I_{(hkl)}(Q)/I^0_{(hkl)}$) vs. dimensionless dose (Q/Q_c) for C8 and C12. The clear breakpoint in decay time at $\approx 2\times$ the critical dose for C8 shows a transition from one predominant disordering mechanism to another. C12, by comparison, shows no breakpoint and amorphizes directly. Curves offset to permit comparison.

tensity loss for these residual points yields a critical dose estimate of 52 ± 15 mC/cm^2. Such a value constitutes an increase of over $3\times$ for the critical dose of these same points compared to their initial fading. The dose dependence of critical dose can clearly be seen in the semilog plot of normalized spot intensity vs. dimensionless total dose (Figure 4.5). There is a clear break point ($\approx 2Q_c$) where intensity loss dramatically slows

The structure implied by this small collection of points is, at best, intermediately ordered. Just as the smectic C diffraction patterns for C8 and C12 in Chapter III

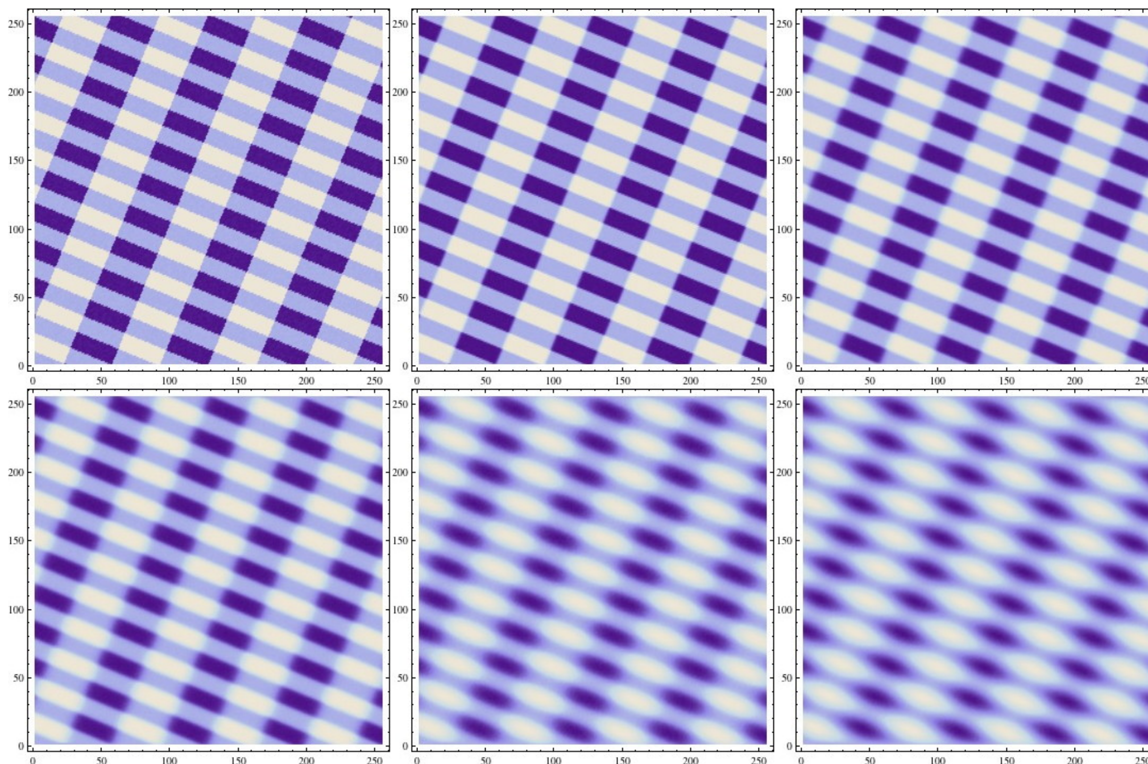

Figure 4.6: Visualization of the transition from the rigidly ordered, as-cast phase to the intermediately ordered phase induced by electron flux. With so few diffraction spots, the intermediately ordered phase is best understood as smoothly varying density fluctuations rather than precisely defined atomic positions.

implied a sinusoidal density fluctuation along [001], these patterns imply a smooth variation of density in the $a'b'$ plane (Figure 4.6). Such a density distribution implies the rigid sort of packing—*i.e.* molecules at precise positions—observed from the original crystals has given way to a similar, but less regular, structure. In this new structure, which resembles higher order LCs or so-called soft crystals, atomic positions deviate from the mean sufficiently that only these few diffraction spots remain.

At this point, at doses in excess of 7× the critical dose of PE (with 99.9% intensity loss), one would expect the substitutions to have lost all long range order. In this residual structure, in which crystallinity is stratified into ordered T5s and glassy substitutions, a phase of limited overall order exists due to interactions between neigh-

boring T5 cores. This residual structure, while resilient, is not impervious to electron bombardment and disorders under continued flux. As crystallinity is only retained in the aromatic T5 cores, this amorphization proceeds slowly. No third crystalline phase of C8 is observed after prolonged exposure. The slow transition from intermediate order ends in an amorphous state.

While not fundamentally identical to the thermal transitions previously described for C8 (see Chapter III), there are clear similarities in the proposed mechanisms for both. In both the thermal and electron flux cases, the transition to a less ordered phase is driven by substitution disorder. The essential difference between the two is the precise mechanism by which that disorder is introduced. For the thermal transition, the conferral of additional freedom of motion produces disorder in the side chains that results in the new structures. Contrast this with the electron flux induced transition described in this chapter, in which selective imposition of disorder in the substitutions through broken bonds and displaced atoms produces new C8 structures.

4.2.2 Dynamic Diffraction of C12

Figure 4.7 demonstrates the fading of C12 diffraction patterns under 300 kV electron flux. As with C8, the immediate change is to the loss of odd $(h00)$, indicating the development of twofold screw axis symmetry in a. The required dose to induce symmetry formation is again quite low, ≈ 10 mC/cm^2. Given the similarity of C8 and C12, the mechanism for this phase transition is likely similar for both materials.

The subsequent decay of remaining spots is characterized by a critical dose of 13.3 ± 1.4 mC/cm^2. This value is quite similar to that measured for the first C8 transition—arguably the same value, within error. In contrast to C8, however, there is no retention of modest order by C12 after significant electron dose. Normalized intensity vs. dimensionless dose (Figure 4.5) show no clear breakpoint in the data. If such a phase does exist in this material, the key indicator of its existence—the

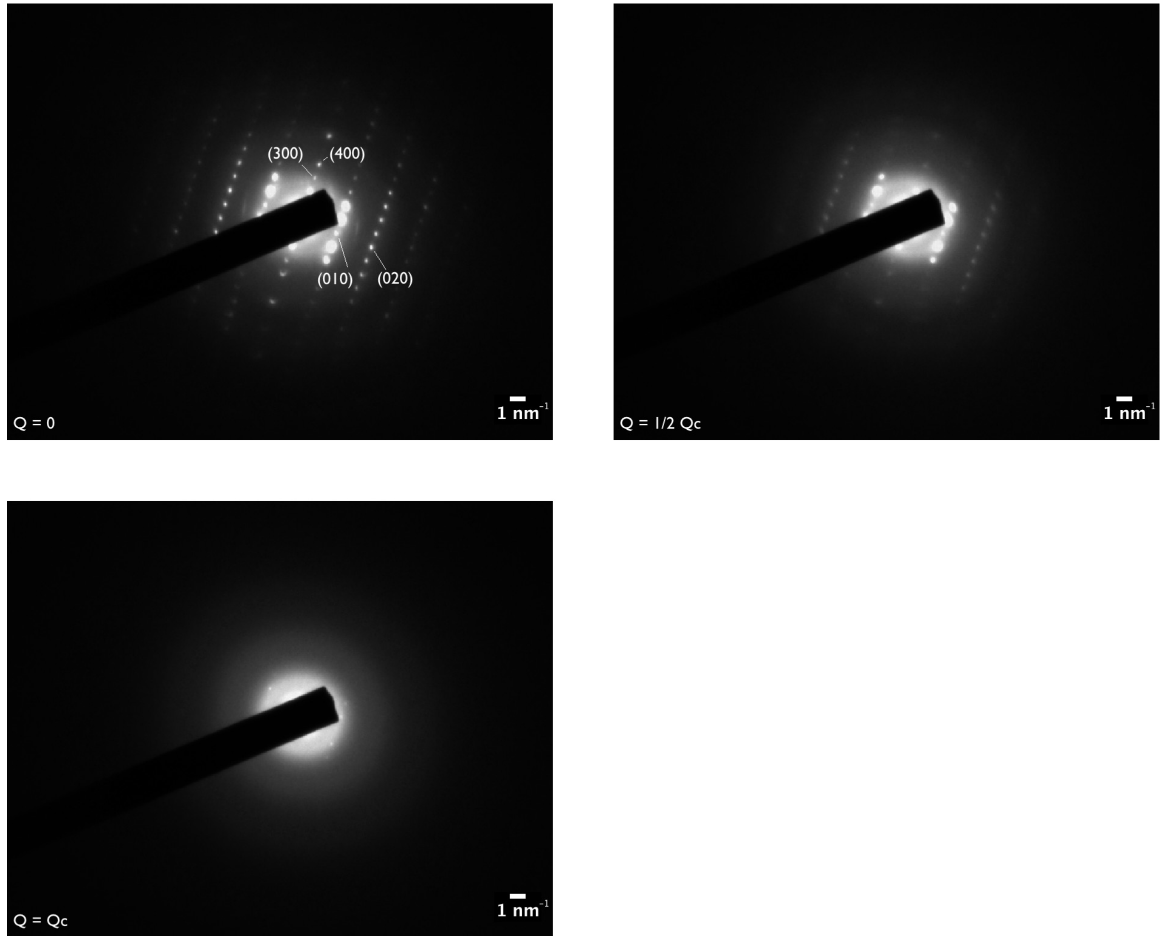

Figure 4.7: Characteristics fading of C12 ED patterns under electron flux. At zero dose, samples are highly crystalline with many diffraction spots. As observed with C8, light dose (≈ 10 mC/cm^2) results in formation of twofold screw symmetry in a. Under continued flux, amorphization occurs with a critical dose of 13.3 ± 1.4 mC/cm^2. In contrast to C8, no long-lived, intermediately ordered phase is observed.

increased critical dose—is so insignificant as to be undetectable in these experiments.

It is surprising that the addition of two butyl segments to the substitutions of C8 would entirely suppress the formation of this intermediately ordered phase, especially in light of the similar behavior for early dose. The DSC behavior of C8 and C12 (*Zhang*, 2011), however, shows that C8 exhibits one more phase than C12. This phase, which exists in the temperature range 152–169 °C and precedes the smectic C phase, has no analog in C12. Given the similarity between thermal transitions and these electron flux induced transitions, this extra thermally-induced phase in C8 seems another indicator that this increase in substitution length can have profound implications for the ability of these materials to order. Presumably some substitution length between nonyl and undecyl is the last to display this intermediately ordered phase, while some shorter length—between methyl and heptyl—is the first.

4.3 Conclusions

The molecular reorganizations of both C8 and C12 under bombardment by high energy electrons produce unique behavior not previously observed in other materials. While these high energy electrons are well known to amorphize crystalline samples, the symmetry order of C8 and C12 are observed to increase—rather than decrease—with low electron doses. The mechanism for this increase in symmetry is the introduction of twofold screw symmetry to the a axis of both materials. Based on the low total dose required to induce this reordering, the likely cause is electron beam induced damage to the substitutions that permits reorganization of the beam resilient T5 cores, elimination of the symmetry-breaking segments from the diffraction pattern or some combination of both.

Under continued flux, reorganization behavior for C8 and C12 diverge. C12 amorphizes directly with a modest critical dose of 13.3 ± 1.4 mC/cm^2, while C8 instead passes through an additional phase before becoming isotropic. Evidently the ad-

ditional substitution length precludes the retention of order by the beam resilient T5 cores. Conversion of as-cast C8 to the intermediately ordered phase occurs at a modest rate, characterized with a critical dose of 15.2 $\pm$ 2.4 mC/cm^2. This additional phase is intermediately ordered, as evidenced by the few, but long-lived, spots in ED patterns. The mechanism for formation of this phase is believed to be further degradation of substitutions, resulting in continued reorganization of the T5 cores. The amorphization of this phase occurs with an increased critical dose of 52.0 $\pm$ 14.5 mC/cm^2.

4.4 Materials & Methods

4.4.1 Materials

C8 and C12 were examined in these studies; synthesis of both is described elsewhere (*Zhang*, 2006). Materials were used as-received after the final sublimation purification step described in *Zhang* (2006). Toluene ($\geq$ 99.5% ACS Reagent Grade) from Sigma-Aldrich was used as received. Bare copper TEM finder grids from Ted Pella were used after deposition of amorphous carbon support films floated from freshly cleaved mica substrates.

4.4.2 Film Casting

Deposition solutions of C8 or C12 were made by dissolving 0.1% by weight T5 in toluene at slightly elevated temperature ($\approx$ 40°C) to ensure dissolution. Single drops of solution were deposited on amorphous carbon coated, copper TEM grids and left undisturbed for 30 seconds. Excess solution was then wicked off the grid with filter paper. Solution remaining on the grid was dried at room temperature in ambient atmosphere. No post-deposition processing steps were implemented. Samples were stored under vacuum prior to imaging.

4.4.3 Collection of Diffraction Patterns

Electron diffraction experiments were carried out on a JEOL 3011 Ultra High Resolution TEM operated at 300 kV. Video of fading diffraction spots was recorded using AMT Capture software. Sample current density was measured using the microscope's cathodoluminescence (CL) screen current density meter, assuming no beam absorption by the sample. Sample current density was controlled *via* selection of condenser aperture and/or Spot Size (C1/C2 lenses) and not by focusing of the C3 (post aperture) lens, which remained defocused. C8 and C12 were used as their own calibration standards.

4.4.4 Analysis of Diffraction Patterns

Intensity of diffraction spots were analyzed using ImageJ software. Image stacks covering the initial display of diffraction spots through their complete disappearance were generated from movie files captured from the CCD keeping only every 15$^{\text{th}}$ (for C8) or 10$^{\text{th}}$ (for C12) frame. Intensity vs. time plots were generated for the examined spots—(210), (110), ($\bar{1}$10), ($\bar{2}$10), (2$\bar{1}$0) and ($\bar{2}\bar{1}$0)—through use of the Plot Z-axis Profile command on a circular region 8 pixels in diameter, centered on the relevant diffraction spot. Time was converted to dose by averaging the recorded screen current densities ($\approx$ 20% variation) and scaling by the square of magnification. The mean grayscale value of this circular area was used as the intensity, $I_{(hkl)}(Q)$, for critical dose determination. The (020) and (0$\bar{2}$0) were not analyzed as the strong background surrounding the direct beam inhibited measurement of data of sufficient quality for analysis.

The minimum measured intensity for each (hkl)—the mean grayscale value recorded inside the region of interest after complete amorphization—was used as the (dose independent) background intensity for each (hkl) and subtracted from all $I_{(hkl)}(Q)$. At low total dose, intensity for analyzed spots was sufficiently high to saturate detector

pixels; such data were excluded for purposes of decay constant fitting. Remaining data points were plotted on semilog plots of background-free intensity vs. total dose.

All plots were evaluated for the obvious presence of multiple decay constants. Those with a clear breakpoint in the I vs. Q slope (*i.e.* C8) were fit with separate linear best-fit equations for each region. The slopes of these best-fit lines—equal to -1/Q_c—were used to calculate the decay constant for each region in the plots.

C12 plots appeared to have no intensity decay breakpoint. Data were plotted on semilog plots and fit with linear equations. The high quality of these fits, and the absence of a visible breakpoint, substantiate the conclusion that no second phase is visible from these experiments.

Additional measurements, such as $q(\boldsymbol{r})$ for translation of diffraction peaks, were also made in ImageJ.

4.5 Acknowledgements

Shandor G. Dektor is acknowledged for his assistance producing visualizations of the intermediately ordered phase of C8. The financial support of NSF DMR-0315633 is also acknowledged.

CHAPTER V

Impedance Spectroscopy of Triisopropylsilyl Pentacene Thin Film Transistors

5.1 Introduction

Characterization of transport in organic materials for transistor applications is frequently—almost exclusively—conducted using DC techniques (*Dimitrakopoulos and Malenfant*, 2002). These techniques are important characterization tools, as they give good measure of the performance a device will exhibit in most of its intended applications (*Anderson and Anderson*, 2004). Such techniques are inadequate for thorough materials characterization, however, due to their limited ability to study the dynamics of charge transport (*Barsoukov and Macdonald*, 2005). Though transport dynamics in these systems remains one of the most active areas of interest in the field (*Street et al.*, 2005; *Northrup et al.*, 2008; *Salleo et al.*, 2010; *O'Neill and Kelly*, 2011), the principal transport characterization tools are static in nature.

IS, in contrast, measures time dependent transport properties. By measuring the time—or equivalently, frequency—dependence of transport, significantly more insight can be gained (*Orazem and Tribollet*, 2008). Such measurements permit the separation of individual transport processes that are indistinguishable in DC. For example, transport in grains and grain boundaries can be decoupled by introducing

frequency dependence to traditional I-V characterization (*Bauerle*, 1969; *Bruce and West*, 1983). IS also permits verification of transport mechanisms by measurement of the characteristic times or frequencies that determine transport behavior (*Hill and Jonscher*, 1979; *Jonscher*, 1981).

This additional insight would be welcome in the study of organic TFT materials. The molecular arrangements of these materials at the interface with the gate dielectric, where it is believed the field effect is most pronounced and the majority of charge transport take place (*Horowitz*, 2004; *Dinelli et al.*, 2004), remains difficult to investigate directly. STM studies have shown, for example, that monolayers of Pn can form with molecules lying flat with π orbitals normal to the substrate (*Schroeder et al.*, 2002). This is in stark contrast to the bulk (*Campbell et al.*, 1961) or thin film (*Drummy and Martin*, 2005) crystal structures, in which π-stacking occurs largely within the plane of the substrate. The structure of the initial layer appears to depend strongly on the nature of the underlying substrate, however, as monolayers of Pn on SiO_2 develop with π-stacking in the plane of the substrate (*Kalihari et al.*, 2009). This first monolayer shows significant misorientation from subsequent layers, however.

The structure of this interface may be studied indirectly by formulating and testing models for charge transport that depend on the details of molecular packing. The variable-range hopping model, for example, has been suggested as suitable for transport in disordered media, due to the range of hopping distances and barrier heights expected in such media (*Jonscher*, 1977). While some argue that organic semiconductors must be disordered at this interface (*Stallinga*, 2009), contrary observations have been made (*Kalihari et al.*, 2008). The various variable range hopping models predict frequency dependence of conductivity, with the details of this frequency dependent on the nature of disorder (*Scher and Lax*, 1973; *Bernasconi et al.*, 1979; *Almond et al.*, 1983; *Abelard and Baumard*, 1984). In the absence of disorder, where

all wells are identical and equally spaced, frequency independent conductivity should be observed (*Barsoukov and Macdonald*, 2005).

5.1.1 Chapter Overview

In this chapter, DC and AC characterization of TIPS TFTs is presented. Devices were formed from solution grown films, composed of collections of discrete single crystals with varying orientation. These devices show good transfer characteristics, with modest mobilities likely due to traps at the SiO_2 interface. The frequency response of the active layer between 1 Hz and 100 kHz exhibits a single impedance peak, indicative of a single relaxation process. The magnitude and frequency of this peak show strong dependence on gate voltage.

Equivalent circuit modeling of these data reveal the linear elements required to produce this behavior are a resistor and capacitor arranged in parallel. The gate-bias dependent resistor behavior is due to the TFT channel, where gate-bias directly controls free charge density and thus conductivity. The capacitive behavior comes from C_{DG} and C_{SG}, the drain-gate and source-gate capacitances associated with the dielectric underneath the TFT. Such a model suggests all frequency dependence of TFT response is due to the gate dielectric, indicating frequency-independent transport in an isolated TFT channel in this frequency range. This frequency independence indicates transport in these TFTs occurs in delocalized states present in crystalline regions of the film, with any localized states—originating from disorder—acting as immobile (trap) states.

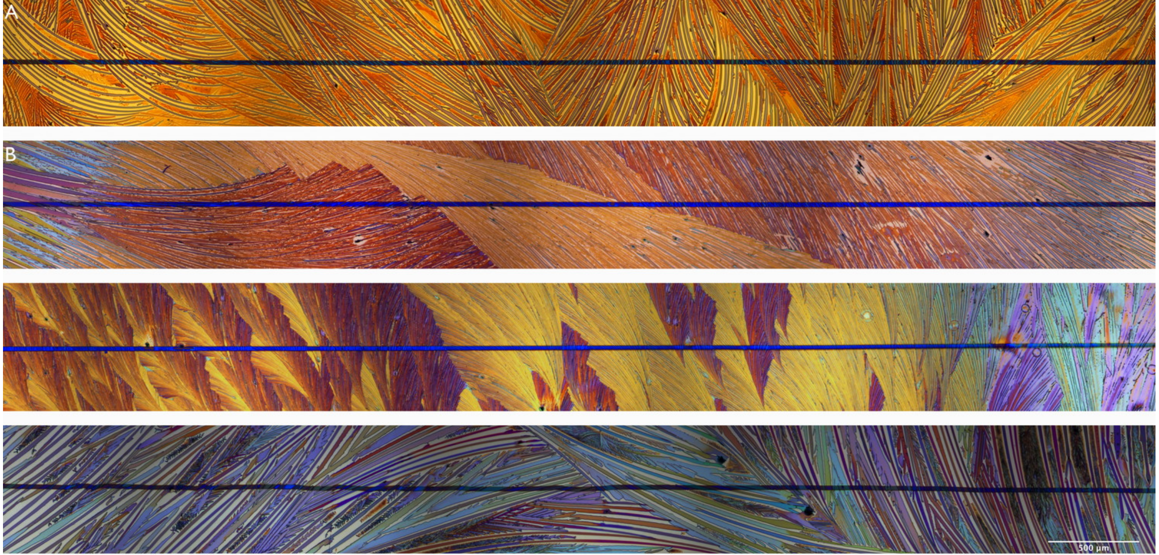

Figure 5.1: POM of TIPS TFTs used for DC and AC analysis. Channel length is 25 µm. Transistors A and B, exhibiting the best and worst DC behavior, respectively, are highlighted in further analysis.

5.2 Results & Discussion

5.2.1 Optical Crystallography

POM of solution grown, bottom contact TIPS TFTs (Figure 5.1) reveals films are composed of long, discrete single crystals with a variety of orientations relative to the TFT channel length. Results from *Chen* (2006) indicate this long crystal direction is [210] and that (001) are parallel to the substrate. Devices with charge conduction along [210] tend to show higher mobility than devices where transport occurs along the various other [$hk0$]s.

Figure 5.2 shows histograms of crystal misorientation in two representative devices, transistors A and B from Figure 5.1. These transistors represent the best (A) and worst (B) performing devices tested. Misorientation, in this context, refers to the deviation between crystal [210] and the channel. Transistor A shows a broad distribution—covering the full angular range of -90 to 90°, with the mode at 0°. Transistor B, in contrast, shows a narrower distribution—largely within 15 and 90°—with

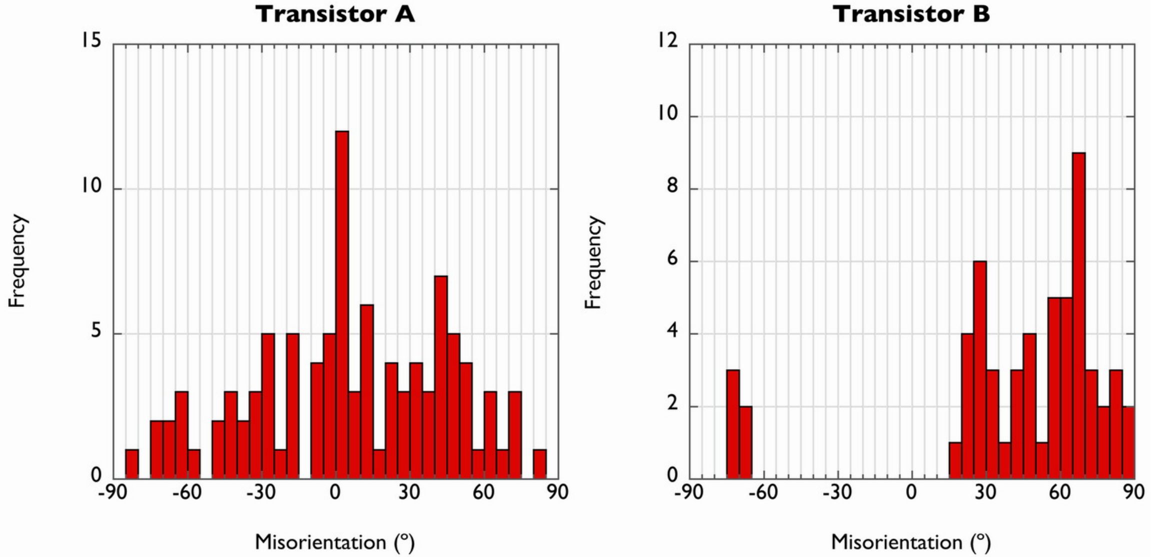

Figure 5.2: Histograms of TIPS crystal misorientation from transistors A and B. Transistor A shows a broad distribution of crystal alignments, though a pronounced mode at the high-performance 0° misalignment. Transistor B shows a narrower distribution, though concentrated about a non-ideal mode of 65°

the mode at 65°. Mean angular misorientation is 5.91° for transistor A and 42.5° for transistor B.

5.2.2 DC Operating Characteristics

DC operating characteristics of the transistors A and B are presented in Figure 5.3 with interpolated transfer characteristics in Figure 5.4. Devices show low threshold voltage and good saturation behavior, indicating low dopant concentration. Hysteresis for these devices (Figure 5.5) is also low, with a 0.2 V shift for transistor A and a 2.5 V shift for transistor B. Transistor A exhibits a field-effect mobility of 1.78×10^{-2} cm^2/Vs, while transistor B exhibits a field-effect mobility of 2.26×10^{-4} cm^2/Vs. Mobility for all 12 tested devices vary between these two extremes, with an average mobility for all devices of 2×10^{-3} cm^2/Vs. These mobility values are modest, but comparable to previously reported values for TIPS (*Chen*,

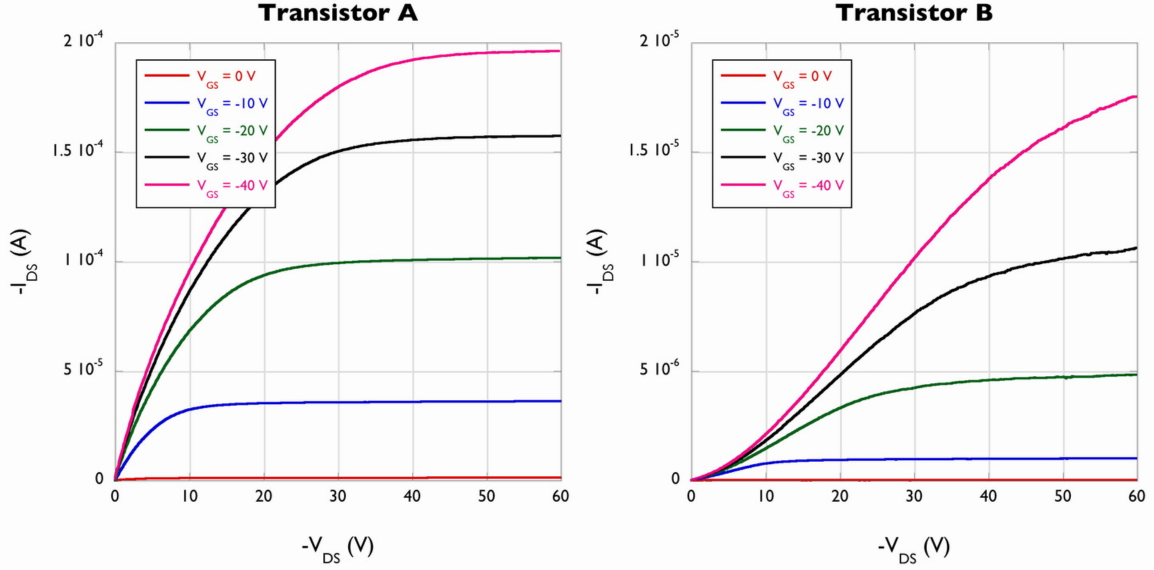

Figure 5.3: DC operating characteristics for TIPS transistors A and B from Figure 5.1. Devices fabricated on 250 nm SiO_2 with 25 µm × 12 mm channel. Transistor A shows modest mobility and low off current. Transistor B shows low mobility and low off current.

2006).

These modest mobility values are likely due, in part, to the lack of any passivating surface treatments on the underlying gate dielectric. The UV/ozone cleaning process used just prior to deposition removes organic contaminants, but leaves a surface decorated with hydroxyl terminations and other chemical defects, believed to cause carrier trapping at the interface (*Salleo et al.*, 2002; *Park et al.*, 2007). The mobility exhibited by these devices also shows prominent anisotropy in agreement with—through greater in magnitude than—prior observations. The device with low misorientation (A) has mobility almost 2 orders of magnitude greater than the device with high misorientation (B).

5.2.3 AC Operating Characteristics

In connection to the distinction between operating characteristics (varying V_{DS}, constant V_{GS}) and transfer characteristics (varying V_{GS}, constant V_{DS}), the term AC

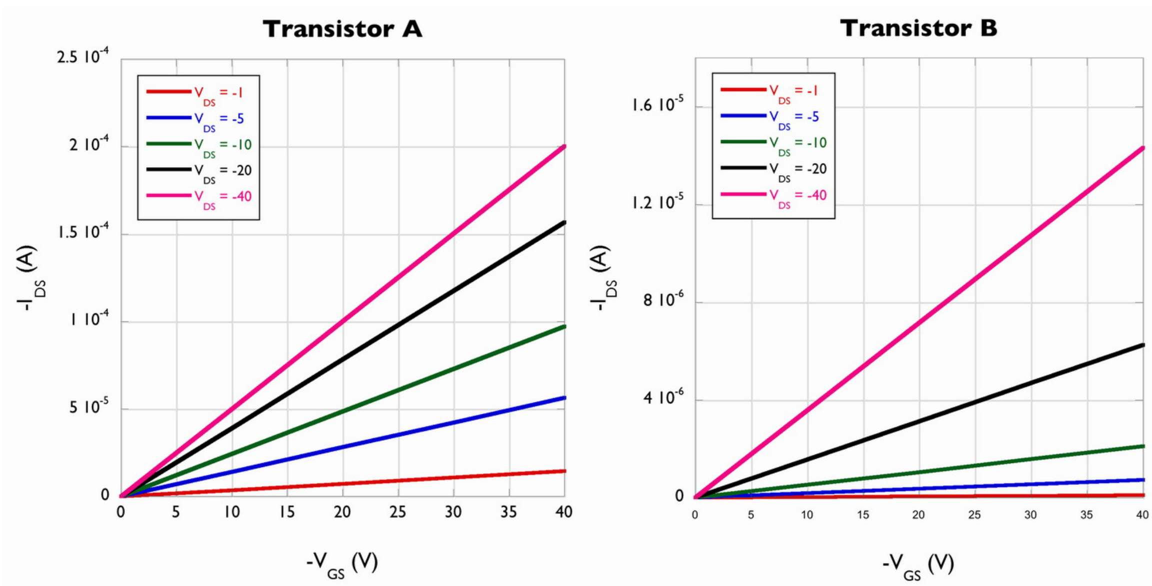

Figure 5.4: Interpolated transfer characteristics for transistors A and B. Transistor A shows good transfer characteristics and modest mobility, while transistor B shows non-ideal transfer behavior at low V_{DS} and poor mobility.

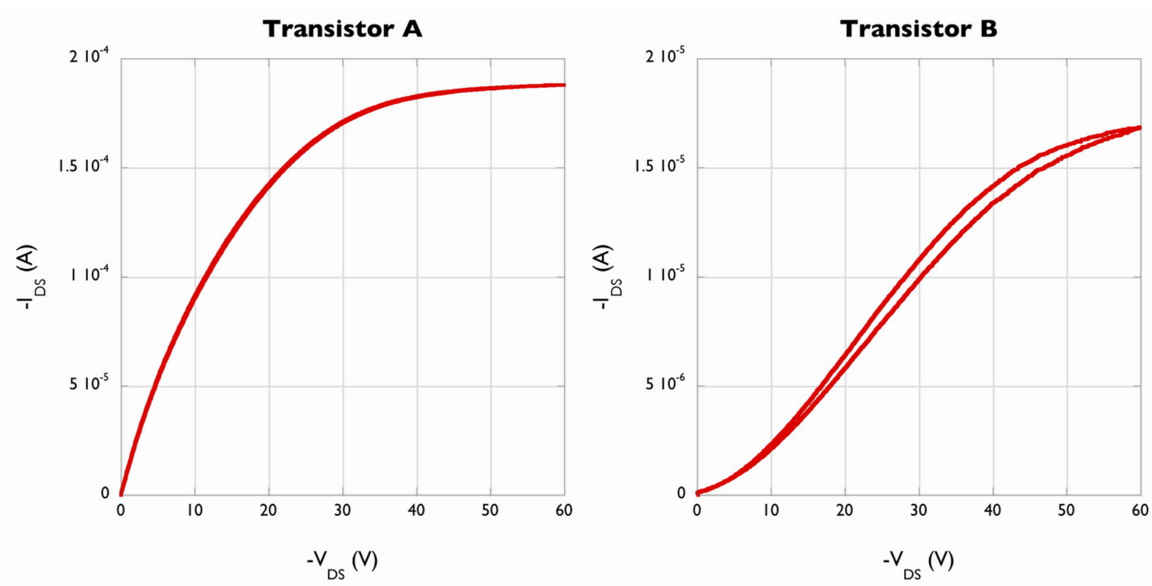

Figure 5.5: Hysteresis curves for transistors A and B at V_{GS} = -40 V and -V_{DS} from 0–60 V. Transistor A shows a 0.2 V shift; transistor B shows a shift of 2.5 V

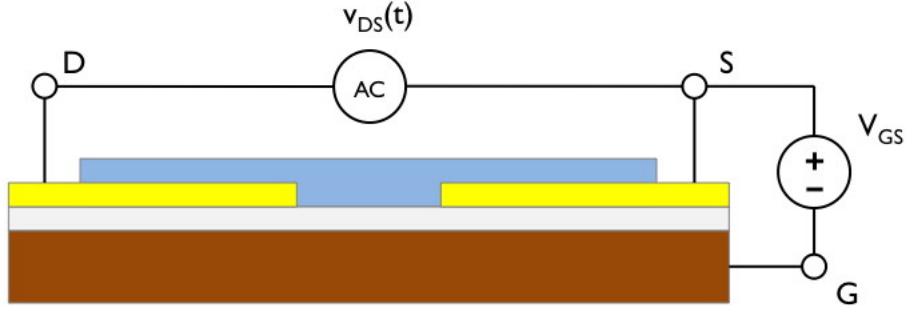

Figure 5.6: Experimental setup for collection of AC operating characteristics. Various gate-source biases are applied to control free charge in the TFT channel, while a small AC probe signal is applied to the drain-source terminal to probe dynamic charge transport. DC biases may also be applied to the drain-source terminals if $V_{DS} = 0$ V TFT behavior is nonlinear.

operating characteristics will here refer to the use of constant gate bias with a small signal AC voltage—potentially superposed on a DC bias—applied to the drain-source terminals. A schematic of such an experimental setup is provided in Figure 5.6. The transfer function measured by such experiments, typically the impedance ($Z_{DS}(f)$) or admittance ($Y_{DS}(f)$), describes the linear response of the TFT to a small signal sine wave at frequency f. Such transfer functions can then be used to calculate the response to arbitrary time-varying input, so long as no frequency component of the input has sufficient magnitude to produce non-linear behavior.

AC operating characteristics of transistors A and B are provided in Figure 5.7. These plots of $Z^{'}$ (loss) and $Z^{''}$ (storage) show similar functional behavior from sample to sample and as a function of bias, though differ quantitatively. Both show the tail of a small, high frequency peak in the $Z^{''}$ data. This peak can safely be ignored, however, as it represents contributions from the sample stage and other instrumentation (see Section 5.4.8). All data also share a second $Z^{''}$ peak at lower frequency. The frequency position of this peak varies from sample to sample, as well as within a given sample as a function of gate bias. At the lowest frequencies—the DC limit—all data converge to very low $Z^{''}$ and high, but constant, $Z^{'}$.

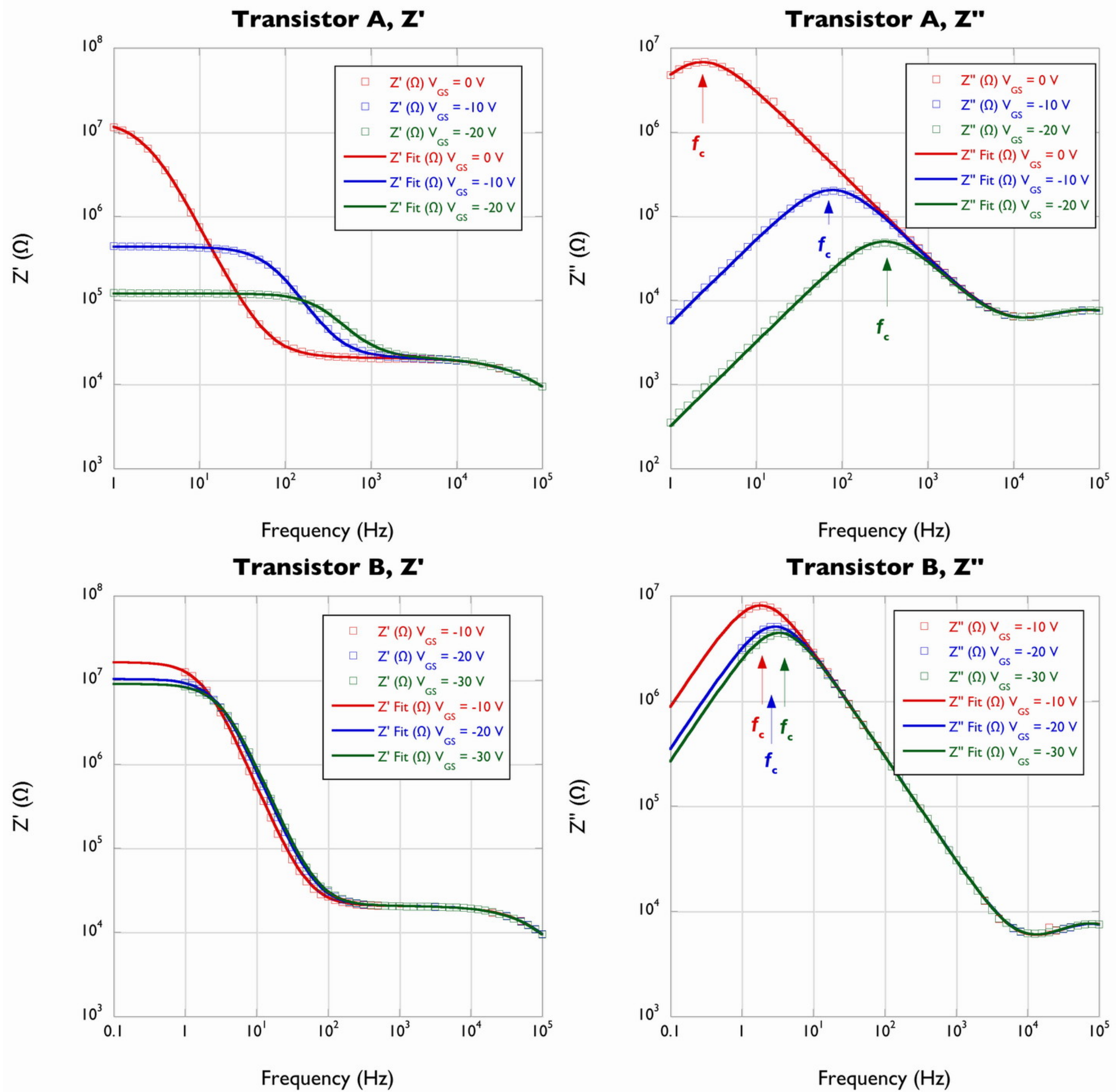

Figure 5.7: AC operating characteristics of transistors A and B. Characteristics show two features: the tail of the peak from the stage at high frequency, and a single relaxation peak at lower frequency. This peak shows strong dependence on both gate bias and sample. As gate bias increases, peak frequency increases while its impedance magnitude decreases. Transistor A, with high mobility, shows more dramatic variation in impedance. Relaxation frequencies indicated in Z'' plots. Best fit curves are the results of equivalent circuit fitting, described in Section 5.2.4

The low frequency saturation behavior of transistor A in the on state indicates that, in the DC limit, this device behaves as a gate bias-dependent resistor. This is the expected behavior for a TFT, where a largely non-conductive channel is made more conductive through charge carriers induced at the dielectric interface by application of a gate bias. The lack of apparent saturation behavior in transistor B does not indicate its DC behavior fundamentally differs from transistor A, however. Equivalent circuit modeling of transistor B (Section 5.2.4) indicates this device exhibits the same saturation behavior, so long as one looks at lower frequencies where the saturation behavior is observed. The characteristic frequencies for transistor B are merely lower—by as much as two orders of magnitude—than those for transistor A.

The low frequency peak in these data indicate electronic relaxation processes take place in these TFTs, with a characteristic frequency (f_c or ω_c) indicated by the peak in the Z'' data. Analogous behavior can be seen in Kelvin-Voigt models of viscoelastic materials (*Young and Lovell*, 1991), exchanging voltage for strain and current for stress. Dynamic mechanical analysis (DMA) of such systems exhibits similar plateaus and peaks in the complex modulus. As with viscoelastic systems, where these characteristic frequencies occur at the frequency of some molecular motion, these electronic systems have characteristic frequencies at the same frequency of key electronic motions. Such motions could be, for example, the orientation of dipoles or the polarization of a medium in response to sinusoidal field.

5.2.4 Equivalent Circuit Modeling

The electrical analog of the Kelvin-Voigt model is a parallel combination of a resistor and a capacitor (Figure 5.8). Such a combination produces behavior qualitatively similar to the AC operating characteristics exhibited by TIPS TFTs, though quantitative agreement was found through fitting these parameters to the data. Pure Voigt

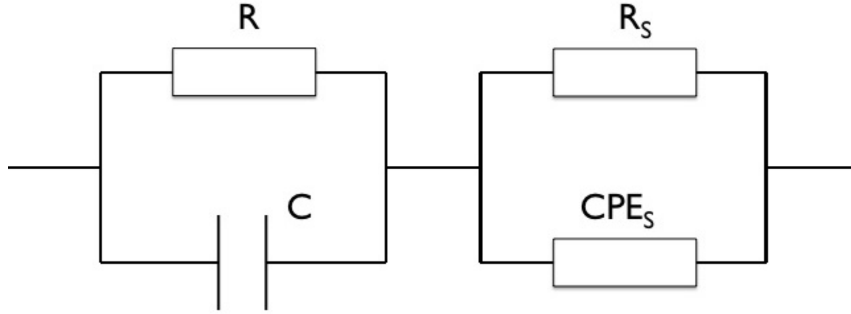

Figure 5.8: Equivalent circuit model for TIPS TFTs. The parallel resistor-capacitor pair (R and C) produce the sample behavior; the parallel resistor-CPE pair (R_S, CPE_S) models the behavior of the stability resistor, sample probes, leads, *etc.*

model fits—*i.e.* single time constant fits—produce good agreement with TIPS TFT data. The AC operating characteristics of transistors A and B—plotted in Figure 5.7—include the $Z(f)$ behavior predicted by these equivalent circuits.

Sample and gate-bias dependence of these fitted parameters are presented in Table 5.1. The fitted resistance, R, shows strong gate bias dependence for both transistors. Such behavior is expected, as the DC operating characteristics show such strong dependence of drain current on gate bias. The fitted capacitance, C, in contrast, shows very little dependence on gate bias. While R varies over orders of magnitude—$< 10^5$ to 10^7 in transistor A—variations in C are dramatically smaller. In the frequency and gate bias range tested, C exhibits less than 0.2% increase per volt of gate bias increase.

The physical basis for this equivalent circuit model can be determined readily from the device geometry itself (Figure 5.9). As IS of TFTs measures the impedance between the source and drain contacts, all current paths connecting the two must be considered. When applying a DC drain-source bias, the only conduction path is through the TFT channel. When drain-source bias is time-varying, however, the drain-gate and source-gate capacitances (C_{DG} and C_{SG}) have finite impedance, and charge can transit the gate dielectric to travel from drain to source. In such a model, the TFT

Sample	V_{GS} (V)	R (kΩ)	C (nF)
A	0	13,589 ± 0.5	4.91 ± 0.01
A	-10	410.4 ± 0.5	5.00 ± 0.01
A	-20	99.3 ± 0.1	5.08 ± 0.01
B	-10	16,247 ± 0.5	5.33 ± 0.01
B	-20	10,237 ± 0.7	5.33 ± 0.01
B	-30	8,929 ± 0.5	5.34 ± 0.01

Table 5.1: Fitted equivalent circuit parameters for transistors A and B. Fit resistor, R, shows strong dependence on gate bias. Capacitance, however, increases $< 0.2\%$/V of gate bias.

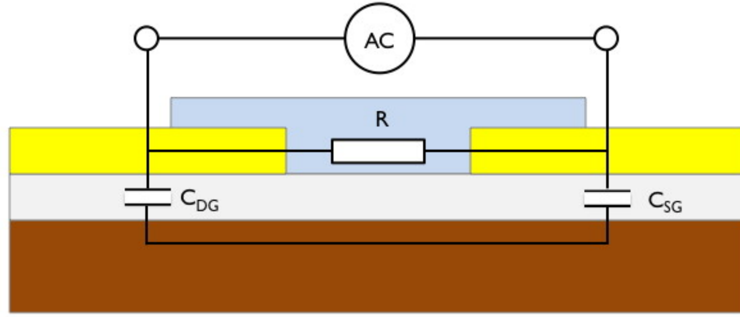

Figure 5.9: Physical meaning for the resistor and capacitor from the equivalent circuit fits. The gate-bias-dependent resistor, R, represents the channel where hole concentration, p—and thus resistance—is determined by gate bias. The capacitor, C, represents the parallel plate capacitors formed by the gate insulator, gate electrode and source/drain electrodes.

channel acts as a gate-bias controlled resistor in parallel with the various gate capacitances, analogous to small signal models of inorganic field-effect transistors (FET)s (*Anderson and Anderson*, 2004). The values of these gate capacitances calculated from device geometry and measured from empty substrates (5.6 nF and 5.8 nF, respectively) further substantiate this model.

5.2.5 Implications for Transport

The AC operating characteristics of whole TFTs shows a clear frequency dependence. However, within this model, conduction in an isolated TFT channel—*i.e.* an organic film in the absence of gate dielectric effects—is frequency independent.

As discussed in the introduction, frequency independent transport indicates carriers transit the delocalized states available in uniformly spaced, identical potential wells. Such a model is consistent with a single crystal—or single crystal texture—as the well spacing and depth (*i.e.* electric potential, $\phi(\boldsymbol{r})$) would have the same translational symmetry as the crystal itself.

Frequency independent channel transport should not be observed if carriers hop (tunnel) through the localized states produced by disorder in these films. Transport through such states would show pronounced frequency dependence due to the distribution of hop distances and well energies along conduction paths from source to drain. While POM investigations of these TFTs show they are composed of discrete single crystals, disorder in various forms must be present in these films. A lack of frequency dependence implies that the localized states originating from this disorder—*i.e.* chemical or structural defects—are immobile in these films.

Gate dielectric capacitances—while essential for device functionality—are inessential for the preceding analysis of channel transport. Removal of these effects from IS data would thus simplify analysis. For devices described by the Voigt model, this can be readily accomplished by altering the geometry of the source and drain electrodes. As the peak in the Z'' data occurs at a frequency given by $f_c = \frac{1}{2\pi RC}$, decreasing the area of the source and drain electrodes—and thus their total capacitance—increases the peak frequency. For example, reduction of the gate capacitances to 2 pF would raise the critical frequency of transistor A in the on state above 200 kHz, beyond the tested range. While the Voigt model would still describe these data, the change in capacitance would significantly reduce the presence of substrate contributions in the results.

5.2.6 DC Mobility From Impedance Data

Additionally, the DC field-effect mobility can be extracted from these IS operating characteristics. In the limit of low V_{DS} (ignoring terms of V_{DS}^2), the I_{DS} expression reduces to:

$$I_{DS} = \mu C_{ox} \frac{W}{L} \left(V_{GS} - V_T\right) V_{DS} \tag{5.1}$$

where C_{ox} is the capacitance per unit area of the oxide, W is the width of the transistor channel, L the length of the channel and V_T the threshold voltage. Rearranging, the expression for mobility, μ, is:

$$\mu = \frac{1}{C_{ox}} \frac{L}{W} \frac{1}{V_{GS} - V_T} \frac{I_{DS}}{V_{DS}} \tag{5.2}$$

But I_{DS}/V_{DS} is just the channel conductance, or $1/R$ from the IS equivalent circuit fitting in the limit of $f \to 0$. This means that mobility can be calculated from the IS data from:

$$\mu = \frac{1}{C_{ox}} \frac{L}{W} \frac{1}{V_{GS} - V_T} \frac{1}{R} = \frac{C}{C_{ox}} \frac{L}{W} \frac{2\pi}{V_{GS} - V_T} f_c \tag{5.3}$$

since $1/R = \omega_c C = 2\pi f_c C$. Thus for a given V_{GS}, mobility depends linearly on the peak frequency from the Z'' plot.

This relationship is not as useful as a calculation tool if an equivalent circuit must be fit to experimental data to determine mobility. However, we can eliminate this need by recalling that the equivalent circuit capacitance, C, can be calculated from known parameters. For electrodes with dimensions W and t, we can replace C with the expression $C = C_{ox} A = C_{ox} W t$ and

$$\mu \approx \frac{C_{ox} W t}{C_{ox}} \frac{L}{W} \frac{2\pi}{V_{GS} - V_T} f_c \approx \frac{2\pi t L}{V_{GS} - V_T} f_c \approx \frac{2\pi t L}{V_{GS}} f_c \tag{5.4}$$

with the far right hand side equation holding when V_T is sufficiently small compared to V_{GS} as to be ignored. This expression depends only on sample geometry, V_{GS}

and the observed peak frequency, permitting quick calculation of mobility from AC operating characteristics.

It should be noted that this simplest form of the mobility equation will underestimate mobility if used as-is with devices with incomplete channel coverage, such as the TIPS TFTs presented here. This lack of complete coverage reduces the effective width of the channel, W_e below that of the full channel width, W. For such devices, W does not cancel from the expression and the equation instead simplifies to

$$\mu \approx \frac{C_{ox}Wt}{C_{ox}} \frac{L}{W_e} \frac{2\pi}{V_{GS} - V_T} f_c \approx \frac{W}{W_e} \frac{2\pi t L}{V_{GS} - V_T} f_c \approx \frac{W}{W_e} \frac{2\pi t L}{V_{GS}} f_c \tag{5.5}$$

Table 5.2 summarizes the calculated mobility of transistors A and B from the AC operating characteristics. These mobility measurements are comparable for transistor A: the average of the three mobilities is 2.5×10^{-2} cm^2/Vs. Mobility measurements for transistor B, however, are consistently higher when derived from AC data than from DC. Some of this variation likely comes from the difference in scan speeds for AC and DC measurements. A sine wave with 20 mV amplitude and 1 Hz frequency has as its maximum sweep rate 0.126 V/s. The DC data, by comparison was swept at a constant 1 V/s, or almost 8 times faster. As the DC operating characteristics data do, in fact, have time dependence, additional resistance—in the form of capacitor charging—would appear in these data, reducing the apparent mobility of the devices. The high value of Z'' for transistor B at 1 Hz in Figure 5.7, demonstrates this. Thus, such AC measurements of mobility may, in fact, prove a more accurate measure of actual film mobility.

5.3 Conclusions

IS data from TIPS TFTs exhibits a single frequency peak consistent with a single relaxation process. These results indicate the AC response of these devices can be

Sample	V_{GS} (V)	μ (cm^2/Vs
A	0	1.8×10^{-2}
A	-10	2.3×10^{-2}
A	-20	3.3×10^{-2}
B	-10	1.1×10^{-3}
B	-20	8.4×10^{-4}
B	-30	6.7×10^{-4}

Table 5.2: Mobility values calculated from AC operating characteristics. Such mobility values are similar to DC-derived results when low frequency impedance is saturated. Values tend to be higher than DC-derived values when low frequency impedance is not saturated, likely due to poor measurement of the low frequency limit by DC methods. Note that V_T for transistor A is 1.86 V, permitting calculation of mobility at $V_{GS} = 0$.

represented with a simple physical model: a parallel resistor-capacitor pair. The physical meaning of the resistor is the gate-bias dependent conductance of the TFT channel, while the capacitor is due to the drain-gate and source-gate capacitances. The implication of this model is that transport in the TFT channel is, in isolation, frequency independent in the range 1-10^5 Hz. This in turn implies transport occurs in the delocalized states available in crystalline segments of these films. These data also suggest that localized states, introduced by disorder in various forms, are not mobile in these devices.

5.4 Materials & Methods

5.4.1 Materials

Thin film devices were fabricated from TIPS powder used as-received from Sigma-Aldrich. Unused material and cast films of TIPS were stored under vacuum until needed. Films were cast using anhydrous toluene from Fisher as-received. Acetone (ACS Reagent Grade, $\geq$ 99.5%) from Fisher was used as received. Bottom contact electrodes were formed using 99.999% gold pellets from Research and PVD Materials Corporation; eutectic gallium-indium alloy ($\geq$99.99%) from Sigma Aldrich was used

to make contact with the gate electrode. Both electrode materials were used as-received. Substrates were fabricated from n^+, arsenic-doped, prime silicon wafers ($\rho \leq 0.01$ Ω-cm) from WRS Materials. Supplier employed chemical vapor deposition (CVD) to increase total oxide thickness to 250 nm ($C_{ox} = 13.8$ nF/cm^2). Wafers were cleaned at several stages of sample preparation as detailed in section 5.4.2.

5.4.2 Substrates

Substrates for bottom contact TFT devices were fabricated by first cleaning as-received Si wafers for 15 minutes in a UV/ozone cleaner at a distance of 5 mm from the lamp. A physical mask was used to define a TFT channel 25 μm long and 12 mm wide. An Edwards Auto 306 thermal evaporator was used to deposit 40 nm gold electrodes. After the mask was removed, a 5 mm × 5 mm section of oxide was removed from the back of each substrate using a diamond scribe. Good electronic contact to the underlying n^+ Si was verified using an ohmmeter. Finally, substrates were rinsed with acetone and then cleaned again by UV/ozone for 60 minutes at 5 cm lamp distance.

5.4.3 Film Deposition

Prepared substrates for film deposition were placed in straight-sided glass vessels on a 2 mm elevated platform. These vessels were covered tightly with aluminum foil and purged for 5 minutes with argon gas at a flow rate of 0.2 L/min. After purging, films were drop cast from 0.1% by weight solutions in anhydrous toluene. Additional anhydrous toluene was placed in the bottom of the deposition chamber—below the level of the substrates—to reduce the rate of evaporation. Deposition chambers were resealed after drop casting and purged with argon at 0.1 L/min until samples had dried. Dried films were stored under vacuum for 12 hours before testing. All deposition steps were carried out under UV-filtered fluorescent light.

After deposition, films were inspected to ensure no TIPS material had reached the cleaved edge of the Si wafer. To avoid shorting the active layer to the gate (the n^+ Si under the oxide), any portion of the TIPS film at the edge of the wafer was removed using chloroform soaked cotton swabs from Fisher and dried under a stream of N_2 gas. Connection to the gate electrode was made by applying the gallium-indium eutectic alloy to the scribed patch of the back of each wafer. Completed samples were placed on glass coverslips for analysis.

5.4.4 Optical Microscopy

Optical crystallography was conducted using a Nikon Eclipse LV100POL POM with a Nikon DS-Ri1 digital camera. Images covering the entire transistor channel were formed by stitching overlapping images covering portions of the channel using Nikon Elements BR software. Quantitative measurements of micrographs (crystal orientation, channel coverage, *etc.*) were made using ImageJ software. Optical crystallography was performed after all electronic testing to eliminate the possibility of photo-induced degradation of the channel material.

5.4.5 Electronic Testing

DC and AC experiments on TIPS TFTs were performed using a Solartron Modulab potentiostat with high voltage, low current and frequency response add-on cards. Experiments were carried out with TFTs sealed inside a Linkham LTSE420 hot stage with pass-through probes and a dry nitrogen purge of 2 L/min. All samples were loaded into the heating stage in dim fluorescent lighting (UVA flux $\approx$ 10 µW/cm^2). Loading samples and connection of probes resulted in approximately 3 minutes of UVA exposure (total dose $\approx$ 1.8 mW/cm^2). After loading, all hot stage windows were blacked out to minimize sample degradation and to eliminate the presence of photo-induced carrier generation.

5.4.6 DC Operating Characteristics

Operating characteristics were collected from all devices by fixing V_{GS} and sweeping V_{DS}. Data were collected for V_{GS} values of 0, -10, -20, -30 and -40 V. V_{DS} was swept from 0 to -60 V at a rate of 1 V/s. Data were also collected at $V_{GS} = +10$ V for samples showing clear unintentional doping to enable better determination of V_T. In total, 12 devices were fabricated and tested to assess the distribution of device parameters.

Mobility (μ) was calculated using both the threshold and linear regime methods (*Stallinga*, 2009). I_{DS} vs. V_{GS} curves were generated by interpolation of I_{DS} vs. V_{DS} data at the five (or six) discrete V_{GS} values. Due to the incomplete coverage of TFT channels, the effective channel width, W_e, determined from measurements of actual channel coverage using POM, were used in place of the channel width defined by the electrode mask (W). Quoted μ values represent an average of the two values, which varied little in the best devices and by up to a factor of 3 in devices showing poor transfer characteristics for low V_{DS}. Threshold voltage was determined as the $I_{DS} = 0$ intercept of the I_{DS} vs. V_{GS} curves determined by interpolation.

5.4.7 AC Operating Characteristics

IS of the TFT channel was collected for V_{GS} values of -10 and -20 V, as well as 0 V if slightly doped or -30 V if dopant concentrations were too low to collect data at 0 V. Data were collected with $V_{DS} = 0$, unless DC operating characteristics showed asymmetric behavior around $V_{DS} = 0$. In such cases, a 150 mV drain-source bias was applied to ensure IS data were collected about a symmetric point near $V_{DS} = 0$. IS data were collected from all 12 devices.

IS data were collected over a frequency range of 1 Hz–10^5 Hz with 10 data points per decade. High frequency data were easily collected largely due to low overall impedance. Low frequency data collection, however, was complicated by high

impedance. Thus, the specific parameters for data collection (AC amplitude, number of cycles integrated, *etc.*) varied from point to point to maximize signal-to-noise ratio (SNR) while minimizing experiment time and sample degradation. The details of these experimental parameters are summarized in Appendix B.

Additional modifications to the experimental setup—for purposes of noise exclusion and potentiostat stability—are detailed in Appendix C. To facilitate background subtraction, IS data were also recorded from the stability resistor with the same experimental parameters (see Section 5.4.8). IS data were also recorded from an empty substrate (gold electrode pads on prepared silicon wafer) to verify the accuracy of calculated capacitance between electrodes.

5.4.8 Impedance Analysis

IS data for TFTs was analyzed using EIS Spectrum Analyzer software for fitting of equivalent circuits. Parameter values for proposed equivalent circuits were determined through use of the the "NM Simp" algorithm, a modification of the Nelder-Mead algorithm with box constraints.

Acquired IS data from TIPS TFTs also contains contributions from instrumentation (the potentiostat, cable runs, probes, *etc.*) and the stability resistor discussed in Appendix C. In order to account for these instrumentation effects in TFT spectra, IS data were recorded with sample leads shorted. The resulting IS data were fit with equivalent circuit models that best represented the data. The model with the best fit was a parallel combination of a resistor and a constant phase element (CPE). Rather than subtract this contribution from IS data of TIPS TFTs, these circuit elements were added in series to all fits of TIPS TFTs. Parameter values taken from the equivalent circuit fit of the shorted sample stage were used as starting values, though these values were allowed to vary 5% when fitting complete TFT spectra.

As discussed in Section 5.2.4, data from TIPS TFTs resembles the Voigt model of a

single resistor-capacitor pair in parallel. Fits of such a model showed good agreement with measured data in the range of 1–10^5 Hz. Deviations between measured and fitted spectra were 2% or less for all fits. 10 of the tested devices were analyzed in detail; the two omitted devices showed poor off current and saturation in DC operating characteristics, indicating high dopant concentrations. Insufficient data were collected from such devices with high unintentional doping to draw significant conclusions.

As TFT IS data contains random noise, the precision of fitted values is limited—in part—by this noise. In spite of the noise, variation in these parameters tends to be small. Errors in these fitted parameters were calculated by making three high-quality fits. The averages of these parameter values are reported as the parameter value, while the standard deviation of these values is reported as the uncertainty.

5.5 Acknowledgements

Jim Mason is acknowledged for his assistance designing electronic test experiments. Bakhtyar Ali, Roy Miller and Xiaoqian Ma are acknowledged for their help preparing TFT substrates.

CHAPTER VI

Impedance Spectroscopy of Poly(2,5-bis(3-alkylthiophen-2-yl)thieno[3,2-b]thiophene) Thin Film Transistors

6.1 Introduction

Shallow traps in organic TFTs, are—by definition—immobilizing electron/hole states where mobile carriers become trapped and escape on short timescales (*Chabinyc*, 2008). These dynamic processes occur over times in the range of 1 ms–10 s. As these traps are thought to play a prominent role in transport of organic TFTs (*Stallinga*, 2009; *Salleo et al.*, 2010), measurement of the trapping and detrapping dynamics of shallow traps is important to understanding the origins of observed transport behavior. As an inherently dynamic measurement, IS should prove a superior means to characterize this trapping behavior than existing DC measurements.

There is strong evidence to suggest that both structural (*Northrup and Chabinyc*, 2003; *Klauk*, 2006; *DeLongchamp et al.*, 2007) and chemical (*Northrup*, 2007; *Chabinyc et al.*, 2007a; *Benor et al.*, 2008) defects produce these trap states in organic semiconductors. While many spectroscopic techniques exist to determine the energies of such trap states *Salaneck et al.* (1988); *Hendrickx et al.* (2000); *Brown et al.* (2003), correlating these measurements with actual transport is complicated by the fact that these

techniques measure entire films. Electronic techniques for measuring these trap energies, however, exclude traps outside the active region as current only flows through the first few nanometers of the film (*Horowitz*, 2004).

Methods to measure trap energies are well established for DC measurements (*Hamadani et al.*, 2007). IS methods can also be used to measure these energies, however, with a number of benefits not shared by DC techniques. For example, the field dependence in Poole-Frenkel models (*Stallinga and Gomes*, 2006b) can be decoupled from the temperature dependence when AC methods are used. As the channel field is nominally zero, the field-dependent term vanishes and mobility depends solely on trap energy. With the low overall impedance of TFTs at higher AC frequencies, such experiments can be conducted with little or no gate bias, potentially eliminating concerns for gate bias stress. Finally, the low voltages required for these AC methods reduce the risk of material degradation induced by the high voltages often required for organic TFT operation.

6.1.1 Chapter Overview

In this chapter, the AC response of PBTTT TFTs is investigated. TFTs are studied *via* IS before and after annealing, as well as at elevated temperatures. TFTs fabricated from as-cast films show modest crystallinity that improves with thermal annealing the in LC phase. As-cast films have a high concentration of dopants, which results in high currents but poor off current and transfer characteristics. Thermal annealing both improves crystallinity and eliminates dopants, resulting in good transfer characteristics but poor mobility due to residual chemical defects likely introduced by the dopant species.

Also, the use of VT-IS to measure activation energies in PBTTT TFTs is demonstrated. VT-IS of as-cast films shows mobility depends exponentially on temperature, likely due to the presence of shallow traps in immobile, localized states. An average

trap energy of ≈200 meV was measured for as-cast devices. Annealing these films in the LC state shows a significant reduction in trap energy. TFTs of annealed films exhibit an average trap energy of 140 meV.

6.2 Results & Discussion

6.2.1 Film Structure

Specular grazing incidence (GI)-XRD of spin-cast PBTTT TFTs (Figure 6.1) shows similar film structure to previous findings (*McCulloch et al.*, 2006; *Chabinyc et al.*, 2007b; *Chabinyc*, 2008). Polymer chains lie predominantly in the plane of the substrate, with alkyl substitutions normal to the substrate. Crystallinity is modest in as-cast films, but increases dramatically after annealing for 10 minutes at 150 °C. At this temperature, PBTTT exhibits a highly ordered LC phase (*DeLongchamp et al.*, 2007, 2008) with sufficient fluidity to permit molecular reorganization.

6.2.2 DC & AC Operating Characteristics

DC operating characteristics (Figure 6.2) and transfer characteristics (Figure 6.3) of PBTTT TFTs before and after annealing indicate that films de-dope—in addition to reorder—at elevated temperature. Before annealing, samples have high off current, poor saturation and poor field effect. These high current values are due to the abundance of free charge induced in these films by dopants. After annealing, off current drops nearly to zero and saturation improves significantly, indicating a significant drop in dopant concentration. Mobility, however, is poor at 4.0×10^{-6}. Evidently some of the dopant species—likely oxygen or ozone (*Chabinyc et al.*, 2007a)—chemically degraded the PBTTT.

AC operating characteristics of as-cast and annealed TFTs (Figures 6.4 and 6.5) were collected using the experimental setup described in Chapter V (reprinted in Fig-

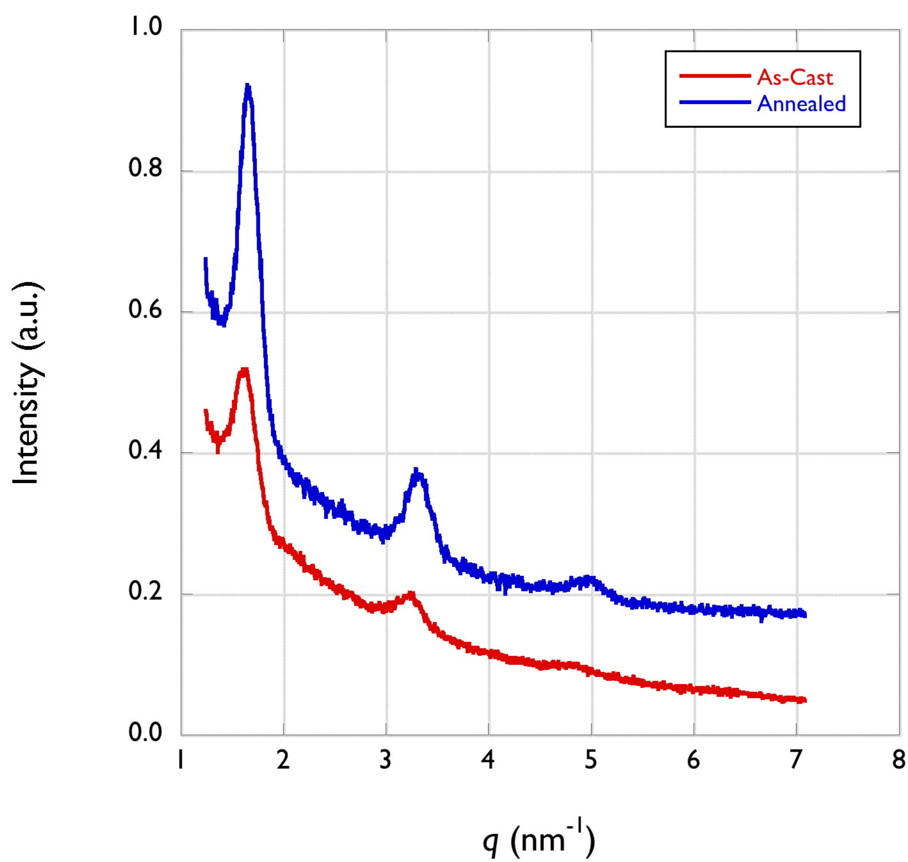

Figure 6.1: XRD of C12-PBTTT TFTs before and after annealing for 10 minutes at 150 °C. Annealed samples show dramatic increases in crystallinity, as evidenced by the $3\times$ increase in diffracted intensity. Peaks are (001), (002) and (003). Measured d-spacing is 1.92 nm, in agreement with *Chabinyc et al.* (2007b). Peaks offset vertically to permit comparison.

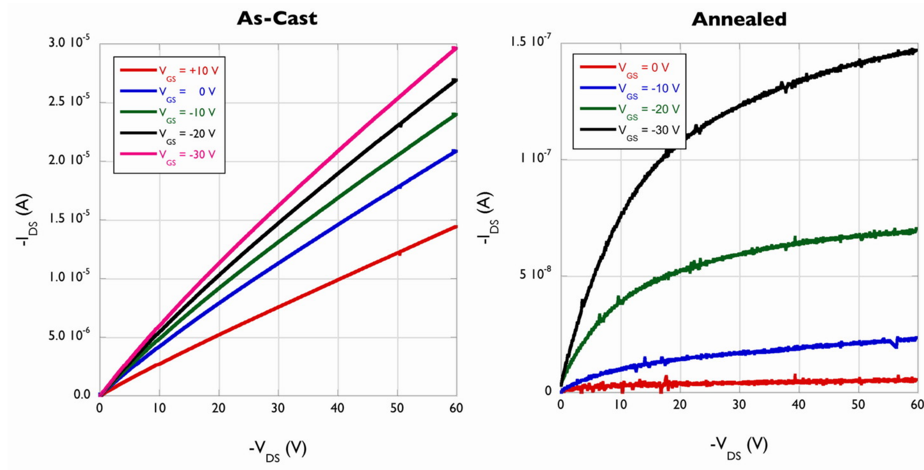

Figure 6.2: Operating characteristics of as-cast and annealed PBTTT TFTs. As-cast TFTs contain a large dopant concentration, and thus display poor off current. Annealed/de-doped TFTs show very low off current but low mobility, likely due to residual chemical defects introduced by dopants. Devices fabricated on 250 nm SiO_2 with 25 µm × 12 mm channel.

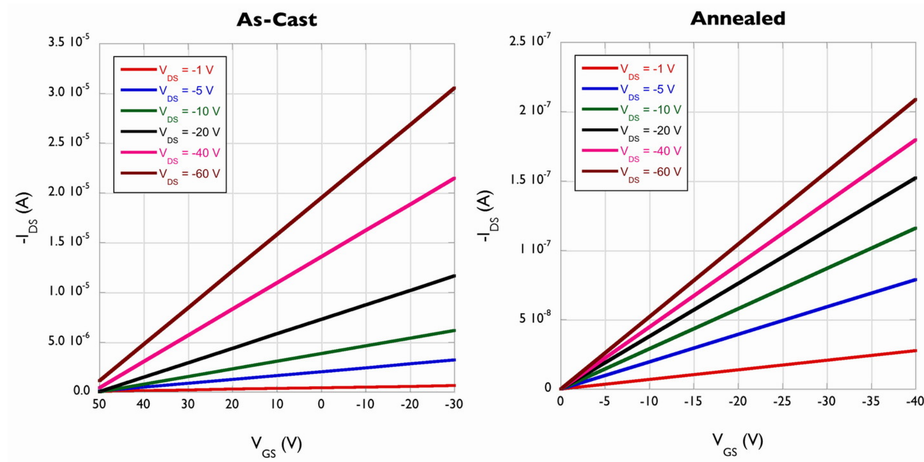

Figure 6.3: Transfer characteristics for as-cast and annealed devices. As-cast devices show large threshold voltage (≈50 V). Annealed/de-doped devices show poor mobility but low off current.

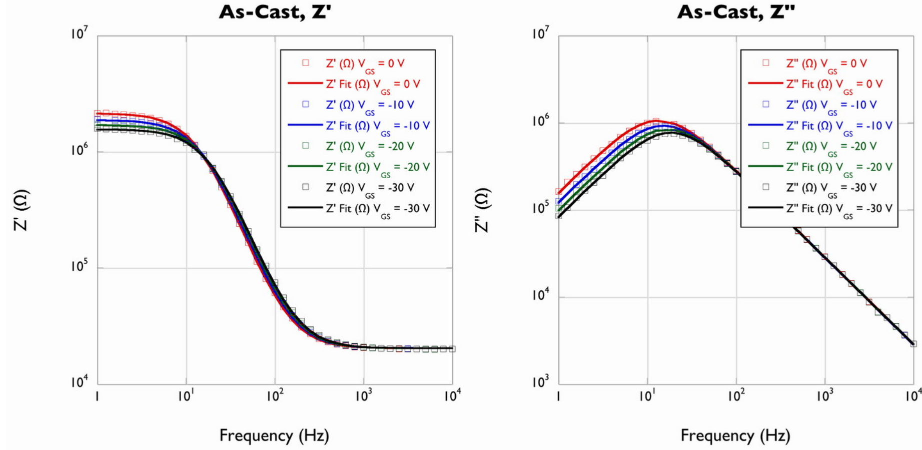

Figure 6.4: AC Operating characteristics for as-cast devices. The limited influence of gate bias on impedance magnitude and peak position is the result of the poor field effect observed in Figures 6.2 and 6.3. Fitted data are from best-fit Voigt models to the data.

ure 6.6). The AC operating characteristics of these TFTs have the same functional form as TIPS AC operating characteristics from Chapter V. Equivalent circuit modeling of a Voigt element (Figure 6.7) again produces good fits to the data. Due to the increased resistance of the de-doped (annealed) devices, the Z' plateau and Z'' peak are shifted to frequencies below the collected range of data. As such, Figure 6.5 contains equivalent circuit model data extended to 0.01 Hz. See section 6.4.8 for a discussion of other attempted fit models.

Using equation 5.3 from Chapter V, mobility was also calculated from the AC operating characteristics. The average mobility calculated from these devices is $\approx 5 \times 10^{-5}$ cm^2/Vs, an order of magnitude larger than the DC-derived value. As seen in Chapter V, these values are likely higher than the DC values due to the influence of capacitive impedance at the sweep speeds used for DC analysis.

6.2.3 Variable-Temperature AC Operating Characteristics of Doped PBTTT

VT-IS data of as-cast, doped PBTTT TFTs in the temperature range 25–90°C are provided in Figure 6.8. These data were collected with zero V_{DS} and V_{GS} using

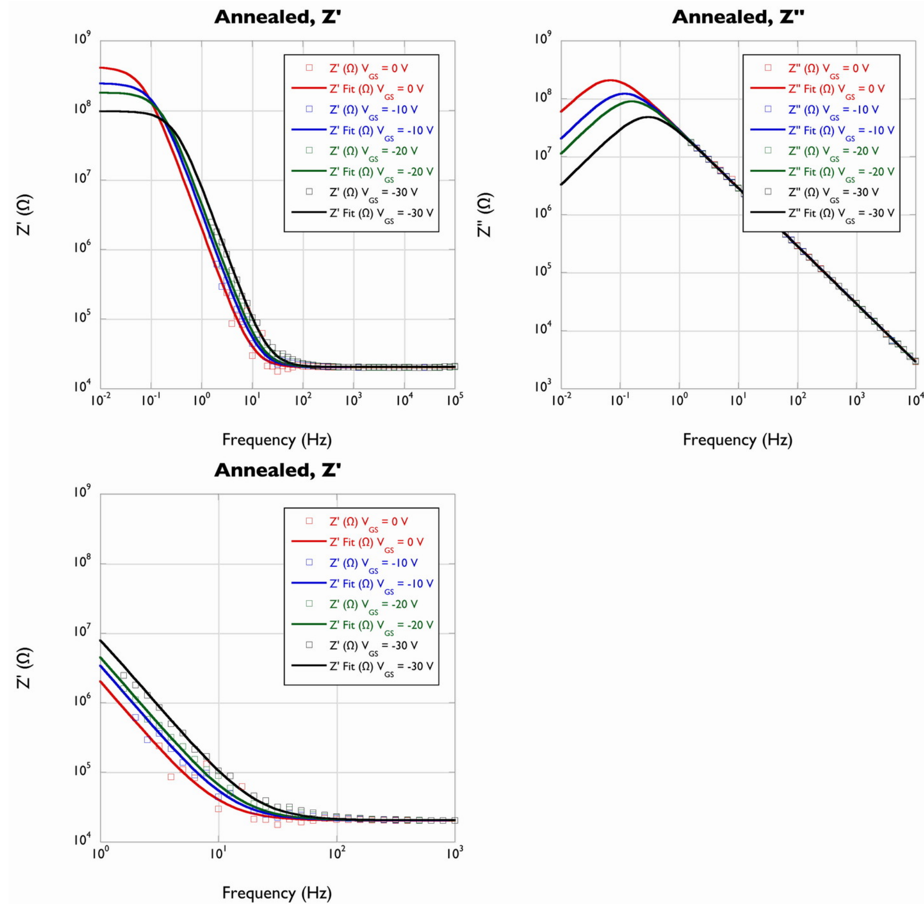

Figure 6.5: AC operating characteristics for annealed devices. Devices show improved field effect over as-cast devices, though poor mobility limits the gate bias modulation of channel conductance. Fitted data are from best-fit Voigt models to the measured data. Data to 10^{-2} Hz extrapolated using the equivalent circuit model. The Z' behavior at low frequency is magnified at bottom-left to resolve individual impedance curves.

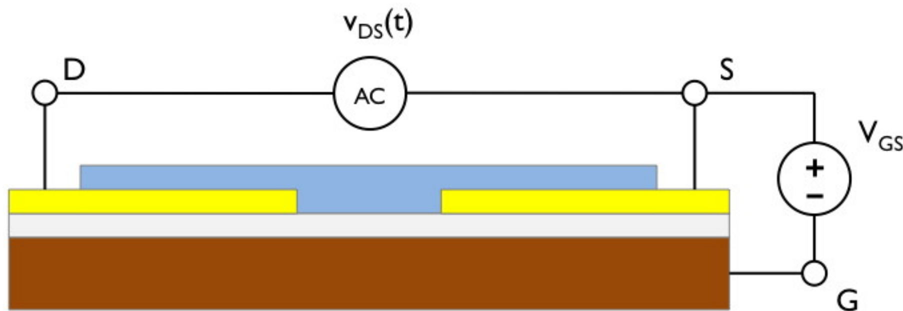

Figure 6.6: Experimental setup for collection of AC operating characteristics and VT-IS spectra.

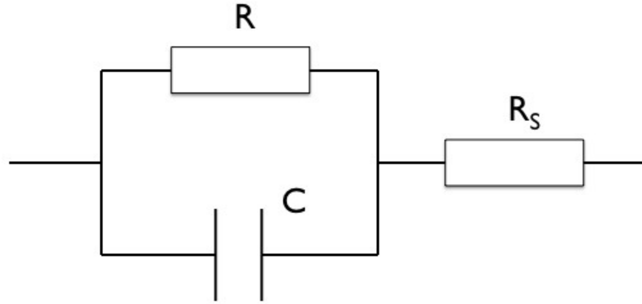

Figure 6.7: Equivalent circuit model for PBTTT TFTs. A Voigt element fit accurately represents the AC response of these devices before and after annealing and as a function of temperature. R_s describes contributions from instrumentation, as discussed in Section 6.4.8

the AC operating characteristics setup previously described. The functional form for these data resembles that seen for TIPS TFTs in Chapter V. The most prominent feature of these data is again the low frequency peak. In this case, the impedance—both magnitude and peak position—show strong dependence on temperature. This temperature dependence is similar to the gate-bias dependence of impedance seen for TIPS and PBTTT TFTs, where in this case higher temperatures lead to lower overall impedance and a higher peak frequency. The same low-frequency saturation (DC limit) behavior is also observed.

These AC operating characteristics again resemble the response of a Voigt model. Fits of these data to a Voigt model show good agreement with measured data. Figure 6.8 contains the curves predicted by these equivalent circuits alongside measured data. As seen in Chapter V, the impedance variation of these TFTs is manifest in a dependence on the resistor, R; little variation in fit capacitance, C, is observed in these data. Table 6.1 contains these fitted values. The fit capacitance again shows good agreement with the calculated and measured values (5.6 and 5.8 nF) of the gate capacitances, indicating the capacitive behavior is again attributable to the gate insulator. As discussed in Chapter V this implies that conduction in these films occurs through the delocalized states available in crystalline regions of the film, with

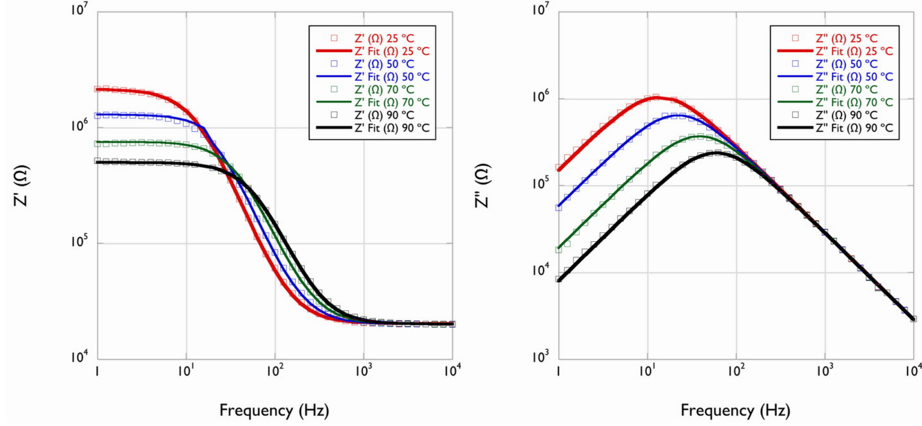

Figure 6.8: VT-IS spectra from as-cast PBTTT TFTs. Devices show strong dependence of impedance on temperature. This temperature dependence is manifest as a temperature dependence of channel conductance. Fit data from equivalent circuit modeling.

T (°C)	R (kΩ)	C (nF)
25	2118.0 ± 6.3	5.54 ± 0.01
50	1276.2 ± 7.8	5.55 ± 0.01
70	735.0 ± 3.4	5.56 ± 0.01
90	480.6 ± 1.2	5.56 ± 0.01

Table 6.1: Fit parameters R and C from equivalent circuit modeling of VT-IS of doped PBTTT TFTs. C shows essentially no variation with temperature while R decreases exponentially with increasing temperature.

disordered-induced localized states acting as immobile traps.

The temperature dependence of the fit resistor, R, can be related to the temperature dependence of mobility through equation 5.3 from Chapter V. From this equation,

$$\mu = \frac{1}{C_{ox}} \frac{L}{W} \frac{1}{V_{GS} - V_T} \frac{1}{R} = A \frac{1}{R(T)} = AG(T) \tag{6.1}$$

where A is the grouping of the temperature-independent factors and $G(T)$ is the conductance of the channel ($= 1/R(T)$). Oxide capacitance, transistor dimensions and gate voltage are essentially independent of temperature, though threshold voltage does show some temperature dependence. However, within this temperature range—

prior to the onset of thermal de-doping discussed in Sections 6.2.2 and 6.4.7—V_T is determined by dopant concentration and is independent of temperature. Thus effective mobility is directly proportional to the channel conductance and shares its temperature dependence.

Temperature dependence of mobility (or conductance) in organic TFTs frequently arises due to localized trap states at the band edge (*Street et al.*, 2005; *Baranovski*, 2006; *Salleo et al.*, 2010). These electronic states, resulting from impurities, structural defects, *etc.*, exist at energies comparable to—though typically lower than—the conductive states that mobile electrons and holes occupy. As the name implies, however, once a carrier occupies one of these states, it becomes trapped and unable to contribute to transport. Thus traps in the TFT channel reduce the population of carriers available for transport and thus decrease the apparent (*i.e.* measured) mobility of devices.

The temperature dependence of these trap states comes from thermal detrapping behavior (*Stallinga and Gomes*, 2006a). The likelihood of a carrier escaping a trap is governed by Fermi-Dirac statistics with exponential dependence on the ratio of the energy depth of the trap state, ΔE_T to the thermal energy (kT). Thus as the temperature—and attempt frequency—is raised, this ratio decreases and the probability of a carrier escaping a trap increases exponentially. With greater carrier concentration in the channel, the apparent mobility—and thus conductance—rises exponentially.

Mathematical models for this temperature dependence can be found in, for example, *Waragai et al.* (1995); *Stallinga and Gomes* (2006b). Poole-Frenkel behavior, predicts that trap states introduce both temperature and drain-source bias dependence of mobility according to

$$\mu = \mu_0 \exp\left[-\frac{\Delta E_T - q\sqrt{\frac{q}{\pi\epsilon}\left|V_{DS}\right|}}{kT}\right] \tag{6.2}$$

where μ is the apparent (measured) mobility, μ_0 is the mobility in the absence of traps, ΔE_T is the trap depth (in energy), q is the carrier charge (typically $\pm e$), ϵ is the permittivity of the material and k is the Boltzmann constant. As these IS measurements are conducted at zero drain-source bias, the bias-dependent term is zero and the mobility should depend on T according to

$$\mu = \mu_0 \exp\left[-\frac{\Delta E_T}{kT}\right] \tag{6.3}$$

where the trap energy, ΔE_T, can be easily extracted from an Arrhenius plot.

An Arrhenius plot of $\ln G(T)$ vs. $1/T$ taken from VT-IS results is provided in Figure 6.9. The best fit line to these data shows excellent agreement and a slope of -2496 K. From equation 6.3, this gives a trap energy of 215 meV. Variation on as-cast trap energy is low, ≈10%. This value agrees well with previous spectroscopy and simulation results from various poly(thiophenes). Cited results indicate that defects in the form of backbone twists (*DeLongchamp et al.*, 2007; *Northrup and Chabinyc*, 2003) and oxygen degradation (*Northrup*, 2007; *Chabinyc et al.*, 2007a; *Benor et al.*, 2008) introduce localized states (*i.e.* traps) up to 300 meV above the valence band edge.

6.2.4 Variable Temperature Impedance Spectroscopy of Annealed PBTTT

As many of these cited traps have origins in structural defects or impurity species, the LC annealing phase of PBTTT should be an ideal means to reduce this trap energy. Figure 6.10 presents AC operating characteristics of annealed/dedoped PBTTT TFTs in the temperature range of 25–130 °C. The most pronounced difference from the doped film behavior is the shifting of the Z'' peak to significantly lower frequencies and higher overall impedances.

Equivalent circuit fitting—using the same equivalent circuit elements as in Section

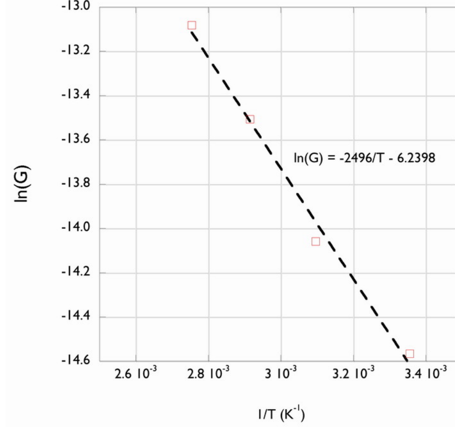

Figure 6.9: Arrhenius plot of $G(T) = 1/R(T)$ for as-cast PBTTT TFTs from equivalent circuit data. The slope, -2496 K = -$\Delta E_T/k$. The trap energy calculated from these data is 215 meV.

T (°C)	R (MΩ)	C (nF)
25	416 ± 88	5.46 ± 0.02
50	272 ± 27	5.48 ± 0.02
70	233 ± 26	5.52 ± 0.02
90	205 ± 26	5.53 ± 0.02
110	123 ± 13	5.51 ± 0.02
130	115.9 ± 2.5	5.54 ± 0.02

Table 6.2: Fit parameters R and C from fitting a Voigt model to VT-IS data for annealed/de-doped PBTTT TFTs. C shows an insensitivity to temperature, while R shows exponential dependence on T.

6.2.3—again results in good fits to these data. These fit parameters are summarized in Table 6.2. Again an insensitivity of capacitance to temperature is observed, with nearly all the impedance changes due to the temperature dependent channel conductance.

Exponential fits of conductance to temperature (Figure 6.11) again show good agreement. The slope of the Arrhenius plot is significantly lower than the as-cast films, indicating a decrease in trap energy. Trap energy from these data is 127 meV, a 41% decrease from the as-cast device. Thus the increase in crystallinity and expulsion of impurity species results in a 30× increase in mobility in these films. While these

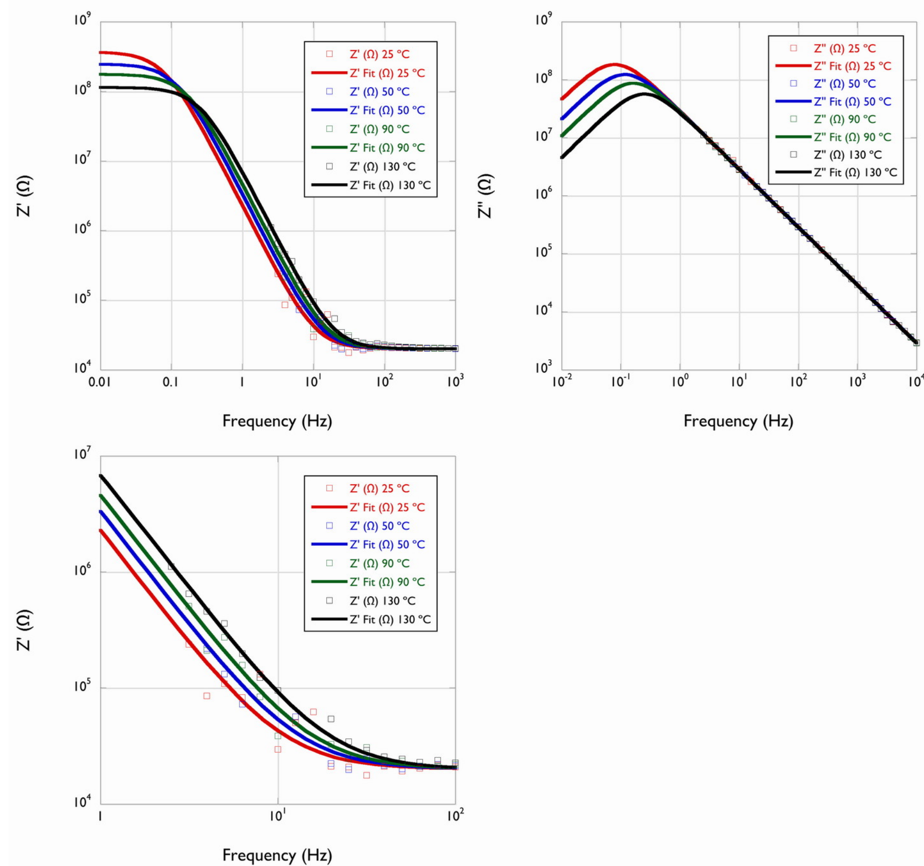

Figure 6.10: VT-IS spectra from annealed PBTTT TFTs. Devices show strong dependence of impedance on temperature. This temperature dependence is manifest as a temperature dependence of channel conductance. Fit data from equivalent circuit modeling. Data to 10^{-2} Hz extrapolated from equivalent circuit model. The Z' behavior at low frequency is magnified at bottom-left to resolve individual impedance curves. Data from 70 and 110 °C omitted for clarity of the figure.

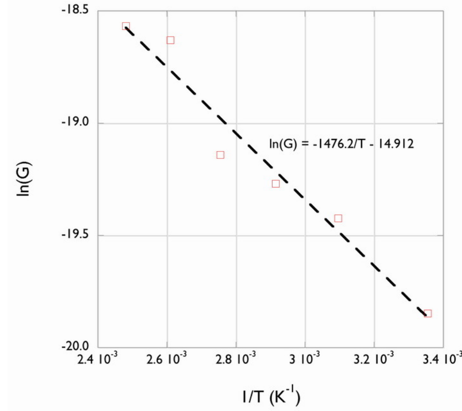

Figure 6.11: Arrhenius plot of $G(T) = 1/R(T)$ for annealed PBTTT TFTs from equivalent circuit data. The trap energy calculated from these data is 127 meV.

results indicate a significant decrease in the influence of traps on device performance, 127 meV is high compared to the thermal energy of carriers. Only at temperatures of 1475 K and above—far beyond the breakdown temperature of PBTTT and other organic semiconductors—would transport insensitive to these traps be observed.

Variation on annealed trap energies is more significant ($\approx$25%) than as-cast devices. This is likely due to variations in residual chemical defects between films. However, these values of trap energy in annealed TFTs are in agreement with *Hamadani et al.* (2007), who measured PBTTT TFT activation energies using DC methods.

As previously discussed, such Voigt model transport in these films indicates conduction occurs through delocalized states available in ordered regions of TFT films. In these PBTTT films, as in the discrete crystal TIPS TFTs from Chapter V, disorder must be present, however. IS results from both materials indicate that the localized states produced in disordered regions do not constitute viable conduction paths in the frequency ranges tested. In PBTTT—through the incorporation of temperature dependence to these measurements—the effects of disorder are made more clear. The localized states that exist in these partially or fully disordered regions contribute immobile trap states.

This is further supported by the decrease in trap energy on annealing/de-doping. XRD data indicate annealing produces an increase in crystallinity (*i.e.* reduced structural disorder). Additionally, DC and AC operating characteristics indicate this temperature processing results in decreased impurity concentration (*i.e.* reduced chemical disorder). These combined observations—frequency independent transport with trap depth correlated with structural and chemical defect prevalence—strongly agree with so-called "mobility edge" models (*Street et al.*, 2005; *Baranovski*, 2006; *Salleo et al.*, 2010). Such models are based on transport through delocalized, mobile states near the band edge with localized, immobile states in the band gap.

6.3 Conclusions

VT-IS of PBTTT TFTs shows that these devices are modeled effectively by the same Voigt element equivalent circuit used for TIPS TFTs. This model is composed of a parallel combination of a resistor and capacitor, and is characterized by a single time constant from a single relaxation process. This model circuit is appropriate for as-cast devices at room temperature, as well as elevated temperatures. The model is also appropriate for annealed devices at room temperature and elevated temperatures.

The resistive behavior in this model comes from the temperature-dependent PBTTT channel conductance, while the capacitive behavior comes from the drain-gate and source-gate capacitances. This implies that frequency dependence of these data are solely due to the capacitances of the gate dielectric. Transport in the TFT channel in isolation is thus frequency independent. As for TIPS TFTs, this implies conduction occurs through the delocalized states available in ordered regions of the film.

VT-IS is also a viable tool for measurement of trap energy. The temperature dependence of the fit conductance in these TFTs fits the model of Poole-Frenkel transport in the presence of trap states. Measurement of this trap state energy in as-cast films using VT-IS techniques produces an average value of ≈200 meV, comparable

to measured and simulated values for shallow trapping behavior. After annealing in the LC state, the measurement of this trap energy decreases by an average of 30% to ≈140 meV. These temperature-dependent results agree with mobility edge models, which predict transport occurs in delocalized states that is hindered by localized, immobile trap states originating from disorder.

6.4 Materials & Methods

6.4.1 Materials

Dichlorobenzene (99%) and acetone (ACS Reagent Grade, $\geq$ 99.5%) from Fisher were used as received. PBTTT was used as received from purification described in *McCulloch et al.* (2006). Bottom contact electrodes were formed using 99.999% gold pellets from Research and PVD Materials Corporation; eutectic gallium-indium alloy ($\geq$99.99%) from Sigma Aldrich was used to make contact with the gate electrode. Both electrode materials were used as-received. Substrates were fabricated from n^+, arsenic-doped, prime silicon wafers ($\rho \leq 0.01$ Ω-cm) from WRS Materials. Supplier employed CVD to increase total oxide thickness to 250 nm ($C_{ox} = 13.8$ nF/cm^2). Wafers were cleaned at several stages of sample preparation as detailed in section 6.4.2.

6.4.2 Substrates

Substrates for bottom contact TFT devices were fabricated by first cleaning as-received Si wafers for 15 minutes in a UV/ozone cleaner at a distance of 5 cm from the lamp. A physical mask was used to define a TFT channel 25 µm long and 12 mm wide. An Edwards Auto 306 thermal evaporator was used to deposit 40 nm gold electrodes. After the mask was removed, a 5 mm × 5 mm section of oxide was removed from the back of each substrate using a diamond scribe. Good electronic contact to the

underlying n^+ Si was verified using an ohmmeter. Finally, substrates were rinsed with acetone and cleaned again by UV/ozone for 60 minutes at 5 cm lamp distance.

6.4.3 Polymer Deposition

PBTTT TFTs were fabricated from 3 mg/mL solution of PBTTT in dichlorobenzene, heated to ≈ 70 °C to ensure complete dissolution. Heated solutions were filtered through 0.45 µm PVDF syringe filters before deposition. Solution was deposited on prepared bottom contact TFT substrates *via* spin coating. Spin coating was conducted at 1500 RPM for 30 seconds with 150 RPM/s acceleration. Coated substrates were stored in glass vessels purged by 0.1 L/min argon for 2 hours to complete drying. To ensure films did not short to the gate electrode (the n^+ silicon underneath the oxide), deposited material near the edge of wafers was removed with a clean razor blade prior to testing. Connection to the gate electrode was made by depositing gallium-indium eutectic alloy at the scribed location. Completed samples were placed on glass coverslips for analysis. All sample fabrication steps were performed under UV-filtered fluorescent light.

6.4.4 X-ray Diffraction

XRD of PBTTT films was conducted on samples before and after annealing using a Rigaku Ultima IV multipurpose XRD X-ray diffractometer with a copper Kα source. Samples were interrogated using GI geometry with 0.2° incident beam. The detector was swept in 0.02° increments at rates of 0.25–1 °/min. Intensity data were normalized based on sweep speed. All XRD was performed after electronic characterization to limit photo-induced degradation of the channel material. In total, three annealed and two as-cast devices were examined using XRD. Demonstrated data are from single annealed and as-cast devices; comparisons of peak intensity are from averages of as-cast and annealed devices.

6.4.5 Electronic Testing

DC and AC experiments on PBTTT TFTs were performed using a Solartron Modulab potentiostat with high voltage, low current and frequency response add-on cards. Experiments were carried out with TFTs sealed inside a Linkham LTSE420 hot stage with pass-through probes and a dry nitrogen purge of 2 L/min. All samples were loaded into the hot stage in dim fluorescent lighting (UVA flux ≈ 10 µW/cm^2). Loading samples and connection of probes resulted in approximately 3 minutes of UVA exposure (total dose ≈ 1.8 mW/cm^2). After loading, all hot stage windows were blacked out to minimize sample degradation and to eliminate photo-induced carrier generation.

6.4.6 Operating Characteristics

DC operating characteristics were collected from all devices by fixing V_{GS} and sweeping V_{DS}. Data were collected for V_{GS} values of 0, -10, -20 and -30 V. Data were also collected at $V_{GS} = +10$ V to enable better determination of V_T. V_{DS} was swept from 0 to -60 V at a rate of 1 V/s. Mobility (μ) was calculated using both the threshold and linear regime methods (*Stallinga*, 2009). I_{DS} vs. V_{GS} curves were generated by interpolation of I_{DS} vs V_{DS} data at the four (or five) discrete V_{GS} values. Quoted μ values represent an average of the two values, unless otherwise indicated. Threshold voltage, V_T was determined as the $I_{DS} = 0$ intercept of the I_{DS} vs V_{GS} curves determined by interpolation.

Operating characteristics were acquired from as-cast devices. After the thermal annealing process described in Section 6.4.7, operating characteristics were again collected. In total, six devices were tested. Quoted mobility values are an average of all devices.

6.4.7 Variable Temperature Impedance Spectroscopy

AC operating characteristics were collected from PBTTT TFTs as-cast at V_{GS} values of +10, 0, -10, -20 and -30 V. Data were collected with $V_{DS} = 0$. IS data were collected over a frequency range of 1 Hz–10^5 Hz with 10 data points per decade. High frequency data were easily collected due to low overall impedance. Low frequency data collection, however, was complicated by high impedance. Thus, the specific parameters for data collection (AC magnitude, number of cycles integrated, *etc.*) varied from point to point to maximize SNR while minimizing experiment time and sample degradation. The details of these experimental parameters are summarized in Appendix B.

VT-IS of PBTTT TFTs was conducted using a Linkam LTSE420 heating stage. After collection of room temperature data, samples were heated at 10 °C/min to 150 °C and held for 10 minutes. Heating was halted at 50, 70, 90, 110, 130 and 150 °C for the collection of impedance data throughout the annealing process. Data at 110, 130 and 150 °C did not satisfy the requirements of time invariance for linear IS analysis. This is likely due to the onset of ion motion at 110 °C and the reorganization of the LC phase at 150 °C. Impedance data collection required holding temperatures for approximately 3 minutes at each temperature value. After reaching 150 °C, samples were cooled at 10 °C/min to room temperature. VT-IS data were collected again at 130, 110, 90, 70 and 50 °C as samples cooled to room temperature. All VT-IS data were collected at $V_{GS} = 0$ V. A full set of AC operating characteristics were again collected after annealing.

Additional modifications to the experimental setup—for purposes of noise exclusion and potentiostat stability—are detailed in Appendix C.

6.4.8 Impedance Analysis

IS data for TFTs was analyzed using EIS Spectrum Analyzer software for fitting of equivalent circuits. Parameter values for proposed equivalent circuits were determined through use of the the "NM Simp" algorithm, a modification of the Nelder-Mead algorithm with box constraints.

Acquired IS data from PBTTT TFTs also contains contributions from instrumentation (the potentiostat, cable runs, probes, *etc.*) and the stability resistor discussed in Appendix C. In order to account for these instrumentation effects in TFT spectra, IS data were recorded with sample leads shorted. The contributions from instrumentation were modeled as a series resistor (R_s). Rather than subtract this contribution from IS data of PBTTT TFTs, this resistor was added in series to all fits of TIPS TFTs. The parameter value taken from the equivalent circuit fit of the shorted sample stage was used as the starting value for fitting TFT data, though this value was allowed to vary 5%.

As discussed in Section 6.7, data from PBTTT TFTs resembles the Voigt model of a single resistor-capacitor pair in parallel when ion motion is inhibited. Fits of such a model showed good agreement with measured data in the range of 1–10^5 Hz. Deviations between measured and fitted spectra were 2% or less for data above 50 Hz, though exceeded this 2% window below 50 Hz.

Errors on impedance measurements using these instruments at frequencies below 1 kHz and impedances greater than 10^6 Ω are $\pm 10\%$. Data from annealed samples demonstrate such high impedances at low frequencies. To properly account for the added uncertainty of low frequency measurements, equivalent circuit fitting weighted data points based on the magnitude of impedance at that point. The NM Simp algorithm employed for equivalent circuit fitting implements this weight by scaling residuals for a given frequency, f, by a factor of $1/|Z(f)|$.

As the Z'' peak is not clearly visible in IS data from annealed samples, equivalent

circuit fitting was also performed with other models. The slope of the impedance ($\approx$1) in log-log plots indicates principally capacitive behavior at tested frequencies. As such, the TFT was modeled as a simple capacitor in series with the stability resistor. Such fits produced good agreement at higher frequencies, but the trailing off of impedance at the lowest frequencies could not be fit with such a model. The introduction of the parallel resistance seen in the Voigt model properly accounts for this.

The combination of random noise and large sample impedance produces greater variation in the fitting of equivalent circuit parameters in these experiments, especially in comparison to TIPS TFTs from Chapter V. To account for this variability, reported values for all equivalent circuit parameters are the average of three values produced from separate, high-quality fits to the data. The reported error on these values is the standard deviation for these three measurements.

6.5 Acknowledgements

Professor Michael Chabinyc is acknowledged for his assistance preparing PBTTT TFTs. Jinglin Liu, Wenlaun Zhang and Professor Michael Mackay are acknowledged for their assistance performing XRD.

CHAPTER VII

Conclusions and Future Directions

7.1 Results of Work

7.1.1 Crystal Structure and Thin Film Morphology of Alkyl-Substituted Thienoacenes

C8 and C12 crystallize into similar unit cells with two molecules per cell. The unit cell for C8 is orthorhombic with lattice parameters $a = 1.15$, $b = 0.43$ and $c = 3.05$ nm. Space group for this unit cell is $Pmmm$, $Pmm2$ or $P222$. The unit cell for C12 is monoclinic (c-unique) with lattice parameters $\gamma = 92.2°$, $a = 1.10$, $b = 0.42$ and $c = 3.89$ nm. Space group for this unit cell is $P2$, Pm or $P2/m$. Within these cells, molecules align with molecular long axes near parallel the c crystallographic axis. The T5 cores in adjacent molecules align into layers, resulting in a unit cell—and macroscopic crystals—where conducting cores alternate with insulating substitution layers. The close packing of molecules inhibits interdigitation of these substitutions. This stacked arrangement of alkyl substitutions produces unique phase behavior discussed in other chapters.

Solution cast thin films of C8 and C12 produce large (50–1000 µm) single crystals ideally suited for use as TFTs. The faceting of these crystals—the various (110)s, (100)s and (010)s—give a clear picture of molecular alignments from optical obser-

vations of cast crystals. Such knowledge permits fabrication of devices with the best mobility exhibited by these materials.

The strong texturing of both materials is also beneficial for TFTs or other thin film devices with lateral charge transport. As the *c* axis is perpendicular to the substrate, the substitutions are likewise near perpendicular to the substrate. As *c* corresponds to the direction of poorest charge transport, the exclusion of this molecular alignment from the channel of TFTs—without explicit control over texturing—is extremely helpful for implementation of such material in devices.

7.1.2 Thermal Transitions of Substituted Thienoacenes

Both C8 and C12 show complex thermal phase behavior. Both materials exhibit a thermotropic solid-solid phase transition driven by the introduction of disorder—in the form of *gauche* defects—into the substitutions. The lack of interdigitation in both materials effectively doubles the magnitude of the unit cell contraction produced when these defects are introduced. For C8, this substitution contraction results in the *c* lattice parameter reducing from 3.05 to 2.27 nm (25.6%). In C12, *c* decreases from 3.89 to 3.00 nm (22.9%).

This dramatic crystallographic change in turn produces dramatic morphological changes in C8 and C12 crystals. Outwardly pristine, sharply faceted crystals become rough and lose these facets when passing the transition temperature. These new, highly defective structures cannot be restored through thermal cycling; morphological changes from this transition are only reversed by dissolving and recasting crystals.

This dramatic unit cell contraction also produces violent cracking behavior in annealed films. During a complete phase cycle—heating from room temperature to a melt, then cooling back to room temperature—otherwise continuous films with severe cracking are produced. These cracks, in some cases, open with such force as to propel segments on opposite sides of the crack.

The stresses leading to this cracking behavior are likely a consequence of the substitution stacking. At elevated temperatures, when the material is fluid, molecules pack closely together as dictated by the effective volume of the substitutions. As they cool, these close packed substitutions develop large stresses as they revert to an extended conformation.

Both C8 and C12 exhibit a single liquid crystal phase before clearing. This liquid crystal phase is smectic C, *i.e.* a tilted smectic phase. In both cases, this phase is characterized by a layer spacing smaller than the original c axis spacing, though larger than the contracted c axis of the first thermotropic phase. For C8, this layer spacing is 2.63 nm; for C12, this layer spacing is 3.20 nm.

7.1.3 Electron-Beam Induced Transitions in Substituted Thienoacenes

Bombardment of C8 and C12 crystals by high energy electrons produces unique phase behavior in both materials. Under modest total dose ($\approx$10 mC/cm^2), both crystals increase their symmetry order through a selective disordering process. This process involves the production of disorder in the substitutions of both materials, in the form of broken bonds and displaced atoms. While the precise mechanism for this transition—reordering of undamaged material, disordering of non-symmetric material or a mixture of both—are not clear from these data, this transition must be driven by disorder in the substitutions. At such low electron doses, linear segments—such as the alkyl substitutions on both C8 and C12—should be significantly disordered. The beam resilient, aromatic cores should, in contrast, be largely unfazed.

Under continued dose, both materials amorphize with comparable doses at rates well described by the critical dose (decaying exponential) model. For C8, the critical dose is 15.2 $\pm$ 2.4 mC/cm^2; for C12, critical dose is 13.3 $\pm$ 1.4 mC/cm^2. While C12 amorphizes directly from the higher symmetry phase, C8 instead passes through a long-lived, intermediately ordered phase. During the transition process, a expands

and b contracts, though both return to their initial values in the intermediately ordered phase. This structure has few diffraction spots, though these spots fade at a dramatically reduced rate ($Q_c = 52.0 \pm 14.5$ mC/cm^2) compared to the corresponding spots of the original phase. On the basis of electron dose required to produce the phase, the residual order—and its beam resilience—is due to the ability of the aromatic T5 cores to resist electron flux induced chemical changes.

There are important similarities to note between the transition to the intermediately ordered phase brought about by electron flux and the "side chain melting" transition induced by thermal means. Specifically, both transitions are driven by disorder in the substitutions. These transitions are distinct from one another, however, as the nature of this disorder is fundamentally different. In the case of the thermal transition, the substitutions adopt defective conformations, though remain intact. In the electron flux induced transition, bonds within the substitution are broken and substitution atoms are displaced.

Despite their similar structure and thermal behavior, no intermediately ordered phase is observed in C12. Evidently the extra substitution length is sufficient to inhibit the formation of such a phase.

7.1.4 Impedance Spectroscopy of TIPS-Pentacene Thin Film Transistors

IS of TFTs of TIPS reveals these devices behave as a parallel combination of a resistor and a capacitor. This capacitance, which shows almost no dependence on gate bias, comes from the drain-gate and source-gate capacitances formed by the electrodes and the gate dielectric. The resistance, on the other hand, shows significant dependence on gate voltage. The resistive behavior comes from the channel material, which shows gate-bias dependent conductivity due to the variations in mobile charge produced by gate bias.

By extension, these results imply that conduction in the channel of these TFTs

is frequency independent. Whole TFTs show frequency dependence because of the capacitor behavior of the gate dielectric; the TFT channel in isolation, however, shows no such dependence. A lack of frequency dependence implies conduction through the delocalized states available in identical, uniformly spaced wells, *i.e.* crystals. These results contravene the supposition that organic semiconductors are largely disordered at the dielectric interface, where transport largely takes place.

7.1.5 Variable Temperature Impedance Spectroscopy of PBTTT Thin Film Transistors

VT-IS of PBTTT TFTs reveals these devices are modeled by the same equivalent circuit used for TIPS TFTs: a Voigt model. This again implies transit through delocalized states available in crystalline regions. Temperature dependent measurements also permit investigation of the role of localized states produced by disordered regions of these films. These localized states act as immobile traps, reducing the effective mobility of devices. Annealing of these films in the liquid crystalline phase reduces this trap energy by an average of 30%. The increase of crystallinity and the decrease in impurity concentration link this trap energy to these defects.

While measurements of trap energy can be performed using spectroscopic or DC techniques, the AC techniques detailed in Chapter VI offer several advantages. Spectroscopic techniques are limited by the spatial selectivity of the measurements. Trap energies can be readily measured, though without ability to discriminate between traps in the channel and the non-conductive parts of the film. DC measurements of this energy have the benefit of examining only the conductive channel, though are complicated by the field dependence of the measurement. As AC experiments only probe the channel, as DC experiments do, without the complicating factor of the bias dependence, they present a simple method for directly measuring this trap energy in PBTTT and other organic semiconductors.

7.2 Possible Future Directions

7.2.1 Substituted Thienoacene Thin Film Transistors

Sufficient crystallographic and thin-film characterization has been performed that thin film devices from these substituted T5s can be fabricated with knowledge of molecular orientations. Slowly grown films produce single crystals of high quality and very large size but with little control over crystal location or orientation. With control over nucleation site, however, single crystal devices can be readily fabricated from these promising materials.

7.2.2 Electron Flux Induced Phase Transition

Characterization of the electron flux induced transition observed in C8 and C12 revealed that substitution length determines whether the phase exists in a given substituted T5. Unclear from these results, however, is the minimum substitution length at which this transition first appears and the maximum length at which it does not. Clearly this transition should not exist in unsubstituted T5, as the transition could not exist without both linear and aromatic segments. At the same time, there is a maximum substitution length—12 or less—where this transition can no longer be observed. Further study of materials with varied substitution length should reveal the substitution length needed to produce and extinguish this phase. Other LC materials with similar structures, such as dioctyl-terthiophene, could be investigated for the presence of this phase. By broadening the scope of these experiments, a clearer picture for the properties that give rise to such a phase could be determined.

7.2.3 Extended Range Impedance Spectroscopy

Potential future uses for IS in the study of organic TFTs can be found by consulting the literature. Especially interesting are studies of polycrystalline, ceramic

ion conductors. In such materials, IS has been used to resolve transport parameters unique to grain interiors, grain boundaries and interfaces with electrodes (*Bauerle*, 1969; *Beekmans and Heyne*, 1976; *Bruce and West*, 1983). For such materials, 2–3 distinct arcs in impedance plots are observed. By correlating changes in microstructure and ion concentrations with IS transport data, clear connections between individual arcs and transport through/across individual grains, grain boundaries and interfaces have been drawn.

Such results, were they produced for organic TFTs, could be extremely beneficial for material and device characterization. As discussed in Chapter I, there is significant difficulty elucidating the precise structure of the active layer of an organic TFT channel. Similar IS results for transport in the channels of TFTs would then give clear information about the structure of this important layer at the dielectric interface. Results presented here show no such frequency dependence. However, such data may exist at frequencies not tested. Impedance spectroscopy techniques can be extended to much higher and lower frequencies, where such data may be found.

An additional possibility is that the samples tested—TIPS and PBTTT—may have lacked the sort of grain boundaries that elicit this behavior. TIPS TFTs, while polycrystalline, were composed of many single crystals long enough to span the channel with no grain boundaries. PBTTT TFTs are also composed of polycrystalline films, though the interconnected nature of polymer crystals would limit the effects of grain boundaries on transport (*Street et al.*, 2005). Polycrystalline Pn TFTs would make excellent samples for these experiments, as the high angle grain boundaries observed are more likely to affect transport (*Kalihari et al.*, 2009).

APPENDICES

APPENDIX A

Heating Stage Construction and Modification

The heater plate used for VT-XRD of C12 is composed of a 3” × 3.5” × 0.5” plate of steel with a 0.5” diameter hole through the center of the large face. A J-type, surface mount thermocouple was affixed to the surface of the plate with a small screw. Heat was supplied from a pair of 200 W cartridge heaters placed inside the steel plate. An Omega 79000 process controller was used to provide heating control. Sample temperatures were calibrated relative to measured temperatures by use of standards. Vanillin, sulfapyridine and phenacetin melting point standards were obtained from US Pharmacopeia and used as directed.

Temperature control of C8 was achieved through use of a modified Linkam THS1500 heating stage. The stock glass windows from a the stage were removed and replaced with 6 µm thick Mylar films supplied by Chemplex. 1 mm OD, 0.01 mm wall thickness XRD capillaries were filled C8 powder and placed into an aluminum collar. Mounted capillaries were then placed inside the heating stage and secured in place with bundles of PBO fiber from Toyobo. The stage was then sealed shut. During heating, the stage was continuously purged with dry nitrogen at a rate of 0.5 L/min.

APPENDIX B

Experimental Parameters for Impedance Spectroscopy of TIPS and PBTTT

Experimental parameters for IS of TIPS Pn are summarized in Table B.1. Parameters for PBTTT TFTs are summarized in Table B.2. Overlap data points and Kramers-Kronig analysis were utilized to ensure linearity was maintained as AC amplitude increased.

Frequency Range (Hz)	AC Amplitude (mV)	Integrations
10^3–10^5	10	1 second
10–10^3	20	2 seconds
1–10	100	20 cycles

Table B.1: Experimental parameters for IS of TIPS TFTs

Frequency Range (Hz)	AC Amplitude (mV)	Integrations
10^3–10^5	10	1 second
10–10^3	40	2 seconds
1–10	60	20 cycles

Table B.2: Experimental parameters for IS of PBTTT TFTs

APPENDIX C

Special Concerns for Impedance Spectroscopy of Organic Thin Film Transistors

At high test frequencies, the impedance of all tested devices is predominantly capacitive. With the low output impedance of modern potentiostats, frequency-dependent filters are often formed—inadvertently—from the potentiostat's output resistance and sample capacitance. As such filters alter the feedback signal to the potentiostat, stability problems may result from driving highly capacitive loads (such as organic TFTs).

To counteract this effect, the low output resistance of the potentiostat was bolstered by use of a discrete 20 kΩ resistor. This resistor was connected in series with the TFT under test by inserting it between the drain electrode and the counter/reference electrode of the potentiostat. As evidenced by the lack of current crowding, this resistor is sufficiently small—compared to the resistance of the channel—as to not affect operating characteristics significantly. The high values of resistance determined by equivalent circuit modeling of IS data further validate the assumption that 20 kΩ is sufficiently small as to minimally affect collected data.

This resistor, along with other stray resistances from the sample probes, cable leads, *etc.* were modeled differently in TIPS and PBTTT TFT chapters. In the

TIPS work, this contribution was modeled as a parallel combination of a CPE and a resistor. This is because the variable resistor used for stability demonstrated some mild CPE behavior at high frequency. The resistor used for PBTTT measurements showed no such behavior. As such, the resistor, probes, *etc.* were modeled as a simple resistor for these experiments.

To enhance the ability of the Linkam hot stage to reject EM noise present in the lab, the metal body of the hot stage was connected to the ground point of the Modulab potentiostat. Short cable runs of driven shielded cable were used exclusively for data collection.

BIBLIOGRAPHY

BIBLIOGRAPHY

Abelard, P., and J. Baumard (1984), Dielectric relaxation in alkali silicate glasses: A new intepretation, *Solid State Ionics*, *14*(1), 61–65, doi:10.1016/0167-2738(84)90012-2.

Almond, D. P., G. K. Duncan, and A. R. West (1983), The Determination of Hopping Rates and Carrier Concentrations in Ionic Conductors By a New Analysis of AC Conductivity, *Solid State Ionics*, *8*(2), 159–164.

Anderson, B. L., and R. L. Anderson (2004), *Fundamentals of Semiconductor Devices*, 816 pp., McGraw-Hill.

Anthony, J. E., D. L. Eaton, and S. R. Parkin (2002), A Road Map to Stable , Soluble , Easily Crystallized Pentacene Derivatives, *Organic Letters*, *4*(1), 15–18, doi:10.1021/ol0167356.

Bao, Z., A. Dodabalapur, and A. J. Lovinger (1996), Soluble and processable regioregular poly(3-hexylthiophene) for thin film field-effect transistor applications with high mobility, *Applied Physics Letters*, *69*(26), 4108, doi:10.1063/1.117834.

Baranovski, S. (Ed.) (2006), *Charge Transport in Disordered Solids with Applications in Electronics*, 1st ed., 479 pp., John Wiley & Sons, Ltd., Chichester.

Barsoukov, E., and J. R. Macdonald (Eds.) (2005), *Impedance Spectroscopy: Theory, Experiment, and Applications*, 2nd ed., 595 pp., John Wiley & Sons, Hoboken, NJ.

Bauerle, J. E. (1969), Study of Solid Electrolyte By a Complex Admittance Method, *J. Phys. Chem. Solids*, *30*, 2657–2670.

Beekmans, N., and L. Heyne (1976), Correlation between impedance, microstructure and composition of calcia-stabilized zirconia, *Electrochimica Acta*, *21*(4), 303–310, doi:10.1016/0013-4686(76)80024-2.

Benor, a., D. Knipp, J. Northrup, a. Volkel, and R. Street (2008), Influence of gap states on the electrical stability of pentacene thin film transistors, *Journal of Non-Crystalline Solids*, *354*(19-25), 2875–2878, doi:10.1016/j.jnoncrysol.2007.10.093.

Bernasconi, J., H. U. Beyeler, and S. Strassler (1979), Anomalous Frequency-Dependent Conductivity in Disordered One-Dimensional Systems, *Physical Review Letters*, *42*(13), 819—-822.

Brinkmann, M., and P. Rannou (2009), Molecular Weight Dependence of Chain Packing and Semicrystalline Structure in Oriented Films of Regioregular Poly(3-hexylthiophene) Revealed by High-Resolution Transmission Electron Microscopy, *Macromolecules*, *42*(4), 1125–1130, doi:10.1021/ma8023415.

Briseno, A. L., et al. (2006), Patterning organic single-crystal transistor arrays., *Nature*, *444*(7121), 913–7, doi:10.1038/nature05427.

Brown, P., D. Thomas, A. Köhler, J. Wilson, J.-S. Kim, C. Ramsdale, H. Sirringhaus, and R. Friend (2003), Effect of interchain interactions on the absorption and emission of poly(3-hexylthiophene), *Physical Review B*, *67*(6), 1–16, doi:10.1103/PhysRevB.67.064203.

Bruce, P. G., and A. R. West (1983), The A-C Conductivity of Polycrystalline LISICON , Li2 + Zn , xGe04 , and a Model for Intergranular Constriction Resistances, *J. Electrochem Soc.*, *130*(3), 662–669.

Byron, D., A. Matharu, R. Wilson, and G. Wright (1995), The synthesis and liquid crystal properties of certain 5,5"-disubstituted 2,2':5',2"-terthiophenes, *Molecular Crystals and Liquid Crystals Science and Technology Section A-Molecular Crystals and Liquid Crystals*, *265*, 61, doi:10.1080/10587259508041679.

Campbell, R. B., J. M. Robertson, and J. Trotter (1961), The crystal and molecular structure of pentacene, *Acta Crystallographica*, *14*(7), 705–711, doi:10.1107/S0365110X61002163.

Chabinyc, M. L. (2008), Characterization of semiconducting polymers for thin film transistors, *Journal of Vacuum Science & Technology B: Microelectronics and Nanometer Structures*, *26*(2), 445, doi:10.1116/1.2889407.

Chabinyc, M. L., A. Salleo, Y. Wu, P. Liu, B. S. Ong, M. Heeney, and I. McCulloch (2004), Lamination method for the study of interfaces in polymeric thin film transistors., *Journal of the American Chemical Society*, *126*(43), 13,928–9, doi:10.1021/ja044884o.

Chabinyc, M. L., R. a. Street, and J. E. Northrup (2007a), Effects of molecular oxygen and ozone on polythiophene-based thin-film transistors, *Applied Physics Letters*, *90*(12), 123,508, doi:10.1063/1.2715445.

Chabinyc, M. L., M. F. Toney, R. J. Kline, I. McCulloch, and M. Heeney (2007b), X-ray scattering study of thin films of poly(2,5-bis(3-alkylthiophen-2-yl)thieno[3,2-b]thiophene)., *Journal of the American Chemical Society*, *129*(11), 3226–37, doi:10.1021/ja0670714.

Chang, J.-F., B. Sun, D. W. Breiby, M. M. Nielsen, T. I. Sölling, M. Giles, I. McCulloch, and H. Sirringhaus (2004), Enhanced Mobility of Poly(3-hexylthiophene) Transistors by Spin-Coating from High-Boiling-Point Solvents, *Chemistry of Materials*, *16*(23), 4772–4776, doi:10.1021/cm049617w.

Chen, J. (2006), Structure, Processing and Properties of the Organic Molecular Semiconductor Triisopropylsilylethnyl (TIPS) Pentacene, Ph.D. thesis, University of Michigan.

Chen, X. L., A. J. Lovinger, Z. Bao, and J. Sapjeta (2001), Morphological and Transistor Studies of Organic Molecular Semiconductors with Anisotropic Electrical Characteristics, *Chemistry of Materials*, *13*(4), 1341–1348, doi:10.1021/cm0008563.

Chou, W.-Y., and H.-L. Cheng (2004), An Orientation-Controlled Pentacene Film Aligned by Photoaligned Polyimide for Organic Thin-Film Transistor Applications, *Advanced Functional Materials*, *14*(8), 811–815, doi:10.1002/adfm.200305047.

Curtis, M. D., J. I. Nanos, H. Moon, and W. S. Jahng (2007), Side chain disorder and phase transitions in alkyl-substituted, conjugated oligomers. Relation to side-chain melting in P3ATs., *Journal of the American Chemical Society*, *129*(48), 15,072–84, doi:10.1021/ja076235t.

DeLongchamp, D., R. Kline, E. Lin, D. Fischer, L. Richter, L. Lucas, M. Heeney, I. McCulloch, and J. Northrup (2007), High Carrier Mobility Polythiophene Thin Films: Structure Determination by Experiment and Theory, *Advanced Materials*, *19*(6), 833–837, doi:10.1002/adma.200602651.

DeLongchamp, D. M., et al. (2008), Molecular Basis of Mesophase Ordering in a Thiophene-Based Copolymer, *Macromolecules*, *41*(15), 5709–5715, doi:10.1021/ma800440f.

Dewijs, G., C. Mattheus, R. Degroot, and T. Palstra (2003), Anisotropy of the mobility of pentacene from frustration, *Synthetic Metals*, *139*(1), 109–114, doi:10.1016/S0379-6779(03)00020-1.

Dierking, I. (2003), *Textures of Liquid Crystals*, 230 pp., WILEY-VCH Verlag GmbH and Co.

Dimitrakopoulos, C. D., and P. R. L. Malenfant (2002), Organic thin film transistors for large area electronics, *ADVANCED MATERIALS*, *14*(2), 99+.

Dinelli, F., M. Murgia, P. Levy, M. Cavallini, F. Biscarini, and D. de Leeuw (2004), Spatially Correlated Charge Transport in Organic Thin Film Transistors, *Physical Review Letters*, *92*(11), 90–93, doi:10.1103/PhysRevLett.92.116802.

Drummy, L., C. Kübel, D. Lee, a. White, and D. Martin (2002), Direct Imaging of Defect Structures in Pentacene Nanocrystals, *Advanced Materials*, *14*(1), 54–57, doi:10.1002/1521-4095(20020104)14:1¡54::AID-ADMA54¿3.0.CO;2-I.

Drummy, L. F. (2003), Crystal Structure, Defects and Plasticity in Pentacene Thin Films, Ph.D. thesis, University of Michigan.

Drummy, L. F., and D. C. Martin (2005), Thickness-Driven Orthorhombic to Triclinic Phase Transformation in Pentacene Thin Films, *Advanced Materials*, *17*(7), 903–907, doi:10.1002/adma.200400189.

Durst, H., and I. G. Voigt-martin (1986), Direct imaging of smectic layers in side-chain liquid crystal polymers by high resolution electron microscopy, *Makromol. Chem. Rapid Commun.*, *7*, 785 – 790.

Finch, D. S., and D. Vesely (1987), The Evaluation of Polymers for Electron Resists by Mass Loss Measurements, *Polymer*, pp. 675–679.

Forrest, S. R. (2004), electronic appliances on plastic, *Nature*, *428*, 911–918.

Funahashi, M., and J.-i. Hanna (1997a), Fast ambipolar carrier transport in smectic phases of phenylnaphthalene liquid crystal, *Applied Physics Letters*, *71*(5), 602, doi:10.1063/1.119806.

Funahashi, M., and J.-i. Hanna (1997b), Fast Hole Transport in a New Calamitic Liquid Crystal of 2-(4-Heptyloxyphenyl)-6-Dodecylthiobenzothiazole, *Physical Review Letters*.

Funahashi, M., and J.-i. Hanna (2000), High ambipolar carrier mobility in self-organizing terthiophene derivative, *Applied Physics Letters*, *76*(18), 2574, doi:10.1063/1.126412.

Funahashi, M., F. Zhang, and N. Tamaoki (2007), High Ambipolar Mobility in a Highly Ordered Smectic Phase of a Dialkylphenylterthiophene Derivative That Can Be Applied to Solution-Processed Organic Field-Effect Transistors, *Advanced Materials*, *19*(3), 353–358, doi:10.1002/adma.200602319.

Gelinck, G. H., et al. (2004), Flexible active-matrix displays and shift registers based on solution-processed organic transistors., *Nature materials*, *3*(2), 106–10, doi:10.1038/nmat1061.

Gonzalez Ronda, L., and D. C. Martin (1997), Lattice Imaging of Electro-Optically Active Poly(nonylbithiazole) (PNBT), *Macromolecules*, *30*, 1524–1526.

Golzhauser, A., W. Geyer, V. Stadler, W. Eck, M. Grunze, K. Edinger, T. Weimann, and P. Hinze (2000), Nanoscale patterning of self-assembled monolayers with electrons, *Journal of Vacuum Science & Technology B: Microelectronics and Nanometer Structures*, *18*(6), 3414, doi:10.1116/1.1319711.

Grosso, G., and G. P. Parravicini (2000), *Solid State Physics*, first ed., 727 pp., Elsevier Science USA.

Hamadani, B. H., C. a. Richter, D. J. Gundlach, R. J. Kline, I. McCulloch, and M. Heeney (2007), Influence of source-drain electric field on mobility and charge transport in organic field-effect transistors, *Journal of Applied Physics*, *102*(4), 044,503, doi:10.1063/1.2769782.

Hanna, J. (2005), Towards a new horizon of optoelectronic devices with liquid crystals, *Opto-Electronics Review*, *13*(4), 259–267.

Hendrickx, E., D. Van Steenwinckel, A. Persoons, C. Samyn, D. Beljonne, and J.-L. Bredas (2000), Effect of the chromophore donor group and ferrocene doping on the dynamic range, gain, and phase shift in photorefractive polymers, *The Journal of Chemical Physics*, *113*(13), 5439, doi:10.1063/1.1289763.

Hill, R., and A. Jonscher (1979), DC and AC Conductivity In Hopping Electronic Systems, *Journal of Non-Crystalline Solids*, *32*(1-3), 53–69, doi:10.1016/0022-3093(79)90064-4.

Horowitz, G. (2004), Organic thin film transistors: From theory to real devices, *JOURNAL OF MATERIALS RESEARCH*, *19*(7), 1946–1962, doi:10.1557/JMR.2004.0266.

Horowitz, G., and M. E. Hajlaoui (2000), Mobility in Polycrystalline Oligothiophene Field-Effect Transistors Dependent on Grain Size, *Advanced Materials*, *12*(14), 1046–1050, doi:10.1002/1521-4095(200007)12:14¡1046::AID-ADMA1046¿3.3.CO;2-N.

Horowitz, P., and W. Hill (1989), *The Art of Electronics*, 1152 pp., Cambridge University Press.

Jonscher, A. K. (1977), The "Universal" Dielectric Response, *Group*, *267*(5613), 673—-679.

Jonscher, a. K. (1981), A New Understanding of the Dielectric Relaxation of Solids, doi:10.1007/BF00542364.

Kalihari, V., E. B. Tadmor, G. Haugstad, and C. D. Frisbie (2008), Grain Orientation Mapping of Polycrystalline Organic Semiconductor Films by Transverse Shear Microscopy, *Advanced Materials*, *20*(21), 4033–4039, doi:10.1002/adma.200801834.

Kalihari, V., D. J. Ellison, G. Haugstad, and C. D. Frisbie (2009), Observation of Unusual Homoepitaxy in Ultrathin Pentacene Films and Correlation with Surface Electrostatic Potential, *Advanced Materials*, *21*(30), 3092–3098, doi:10.1002/adma.200900362.

Kim, E.-G., V. Coropceanu, N. E. Gruhn, R. S. Sanchez-Carrera, R. Snoeberger, A. J. Matzger, and J.-L. Brédas (2007), Charge transport parameters of the pentathienoacene crystal., *Journal of the American Chemical Society*, *129*(43), 13,072–81, doi:10.1021/ja073587r.

Klauk, H. (Ed.) (2006), *Organic Electronics*, 1st ed., 428 pp., WILEY-VCH Verlag GmbH and Co., Weinheim.

Kléman, M., and O. D. Lavrentovich (2003), *Soft Matter Physics: An Introduction*, Springer-Verlag, New York.

Kumar, S. (1990), Electron beam damage in high temperature polymers, *Polymer*, *31*(1), 15–19, doi:10.1016/0032-3861(90)90341-U.

Kumar, S. (Ed.) (2001), *Liquid Crystals: Experimental Study of Physical Properties and Phase Transitions*, 1st ed., 518 pp., Cambridge University Press, New York.

Kuller, a., M. a. El-Desawy, V. Stadler, W. Geyer, W. Eck, and a. Golzhauser (2004), Electron-beam lithography with aromatic self-assembled monolayers on silicon surfaces, *Journal of Vacuum Science & Technology B: Microelectronics and Nanometer Structures*, *22*(3), 1114, doi:10.1116/1.1715083.

Laquindanum, J. G., H. E. Katz, and A. J. Lovinger (1998), Synthesis, Morphology, and Field-Effect Mobility of Anthradithiophenes, *Journal of the American Chemical Society*, *120*(4), 664–672, doi:10.1021/ja9728381.

Liao, J., and D. C. Martin (1993), Direct imaging of the diacetylene solid-state monomer-polymer phase transformation., *Science (New York, N.Y.)*, *260*(5113), 1489–91, doi:10.1126/science.260.5113.1489.

Lin, Y.-Y., D. Gundlach, S. Nelson, and T. Jackson (1997), Stacked pentacene layer organic thin-film transistors with improved characteristics, *IEEE Electron Device Letters*, *18*(12), 606–608, doi:10.1109/55.644085.

Ling, M., C. Reese, A. Briseno, and Z. Bao (2007), Non-destructive probing of the anisotropy of field-effect mobility in the rubrene single crystal, *Synthetic Metals*, *157*(6-7), 257–260, doi:10.1016/j.synthmet.2007.02.004.

Liu, S., W. M. Wang, A. L. Briseno, S. C. B. Mannsfeld, and Z. Bao (2009), Controlled Deposition of Crystalline Organic Semiconductors for Field-Effect-Transistor Applications, *Advanced Materials*, *21*(12), 1217–1232, doi:10.1002/adma.200802202.

Lovinger, A. J. (1985), Polymorphic transformations in ferroelectric copolymers of vinylidene fluoride induced by electron irradiation, *Macromolecules*, *18*(5), 910–918, doi:10.1021/ma00147a016.

Mannsfeld, S., a.L. Briseno, S. Liu, C. Reese, M. Roberts, and Z. Bao (2007), Selective Nucleation of Organic Single Crystals from Vapor Phase on Nanoscopically Rough Surfaces, *Advanced Functional Materials*, *17*(17), 3545–3553, doi:10.1002/adfm.200700330.

Mannsfeld, S. C. B., A. Sharei, S. Liu, M. E. Roberts, I. McCulloch, M. Heeney, and Z. Bao (2008), Highly Efficient Patterning of Organic Single-Crystal Transistors from the Solution Phase, *Advanced Materials*, *20*(21), 4044–4048, doi:10.1002/adma.200703244.

Martin, D. C., and E. L. Thomas (1995), Experimental High-Resolution Electron Microscopy of Polymers, *Polymer*, *36*(9), 1743—-1759.

Martin, D. C., J. Chen, J. Yang, L. F. Drummy, and C. Kübel (2005), High resolution electron microscopy of ordered polymers and organic molecular crystals: Recent developments and future possibilities, *Journal of Polymer Science Part B: Polymer Physics*, *43*(14), 1749–1778, doi:10.1002/polb.20419.

McCulloch, I., et al. (2006), Liquid-crystalline semiconducting polymers with high charge-carrier mobility., *Nature materials*, *5*(4), 328–33, doi:10.1038/nmat1612.

McCulloch, I., et al. (2009), Semiconducting Thienothiophene Copolymers: Design, Synthesis, Morphology, and Performance in Thin-Film Organic Transistors, *Advanced Materials*, *21*(10-11), 1091–1109, doi:10.1002/adma.200801650.

Menard, E., V. Podzorov, S.-H. Hur, a. Gaur, M. E. Gershenson, and J. a. Rogers (2004), High-Performance n- and p-Type Single-Crystal Organic Transistors with Free-Space Gate Dielectrics, *Advanced Materials*, *16*(23-24), 2097–2101, doi:10.1002/adma.200401017.

Northrup, J. (2007), Atomic and electronic structure of polymer organic semiconductors: P3HT, PQT, and PBTTT, *Physical Review B*, *76*(24), 1–6, doi: 10.1103/PhysRevB.76.245202.

Northrup, J., and M. Chabinyc (2003), Gap states in organic semiconductors:Hydrogen- and oxygen-induced states in pentacene, *Physical Review B*, *68*(4), 8–11, doi:10.1103/PhysRevB.68.041202.

Northrup, J. E., M. L. Chabinyc, R. Hamilton, I. McCulloch, and M. Heeney (2008), Theoretical and experimental investigations of a polyalkylated-thieno[3,2-b]thiophene semiconductor, *Journal of Applied Physics*, *104*(8), 083,705, doi: 10.1063/1.2996262.

O'Neill, M., and S. Kelly (2003), Liquid Crystals for Charge Transport, Luminescence, and Photonics, *Advanced Materials*, *15*(14), 1135–1146, doi: 10.1002/adma.200300009.

O'Neill, M., and S. M. Kelly (2011), Ordered materials for organic electronics and photonics., *Advanced materials (Deerfield Beach, Fla.)*, *23*(5), 566–84, doi: 10.1002/adma.201002884.

Orazem, M. E., and B. Tribollet (2008), *Electrochemical Impedance Specrtroscopy*, 1st ed., 523 pp., John Wiley & Sons, Inc., Hoboken, NJ.

Park, Y. D., J. A. Lim, H. S. Lee, and K. Cho (2007), Interface engineering in organic transistors, *Materials Today*, *10*(3), 46—-54, doi:10.1002/adma.201003673.

Rogers, J. a., et al. (2001), Paper-like electronic displays: large-area rubber-stamped plastic sheets of electronics and microencapsulated electrophoretic inks., *Proceedings of the National Academy of Sciences of the United States of America*, *98*(9), 4835–40, doi:10.1073/pnas.091588098.

Rotzoll, R., S. Mohapatra, V. Olariu, R. Wenz, M. Grigas, K. Dimmler, O. Shchekin, and A. Dodabalapur (2006), Radio frequency rectifiers based on organic thin-film transistors, *Applied Physics Letters*, *88*(12), 123,502, doi:10.1063/1.2186384.

Salaneck, W. R., O. Inganas, B. Themans, J. O. Nilsson, B. Sjogren, J.-E. Osterholm, J. L. Bredas, and S. Svensson (1988), Thermochromism in poly(3-hexylthiophene) in the solid state: A spectroscopic study of temperature-dependent conformational defects, *The Journal of Chemical Physics*, *89*(8), 4613, doi:10.1063/1.454802.

Salleo, A., M. L. Chabinyc, M. S. Yang, and R. A. Street (2002), Polymer thin-film transistors with chemically modified dielectric interfaces, *Applied Physics Letters*, *81*(23), 4383, doi:10.1063/1.1527691.

Salleo, A., R. J. Kline, D. M. DeLongchamp, and M. L. Chabinyc (2010), Microstructural characterization and charge transport in thin films of conjugated polymers., *Advanced materials (Deerfield Beach, Fla.)*, *22*(34), 3812–38, doi:10.1002/adma.200903712.

Scher, H., and M. Lax (1973), Stochastic Transport in a Disordered Solid. I. Theory, *Physical Review B*, *7*(10), 4491–4502.

Schroeder, P. G., C. B. France, J. B. Park, and B. a. Parkinson (2002), Energy level alignment and two-dimensional structure of pentacene on Au(111) surfaces, *Journal of Applied Physics*, *91*(5), 3010, doi:10.1063/1.1445286.

Shtein, M., P. Peumans, J. B. Benziger, and S. R. Forrest (2004), Direct mask-free patterning of molecular organic semiconductors using organic vapor jet printing, *Journal of Applied Physics*, *96*(8), 4500, doi:10.1063/1.1791760.

Sirringhaus, H., T. Kawase, R. H. Friend, T. Shimoda, M. Inbasekaran, W. Wu, and E. P. Woo (2000), High-resolution inkjet printing of all-polymer transistor circuits., *Science (New York, N.Y.)*, *290*(5499), 2123–6.

Stallinga, P. (2009), *Electrical Characterization of Organic Electronic Materials and Devices*, 303 pp., John Wiley & Sons, Ltd.

Stallinga, P., and H. Gomes (2006a), Modeling electrical characteristics of thin-film field-effect transistorsII: Effects of traps and impurities, *Synthetic Metals*, *156*(21-24), 1316–1326, doi:10.1016/j.synthmet.2006.09.008.

Stallinga, P., and H. Gomes (2006b), Thin-film field-effect transistors: The effects of traps on the bias and temperature dependence of field-effect mobility, including the MeyerNeldel rule, *Organic Electronics*, *7*(6), 592–599, doi:10.1016/j.orgel.2006.10.003.

Street, R., J. Northrup, and a. Salleo (2005), Transport in polycrystalline polymer thin-film transistors, *Physical Review B*, *71*(16), 1–13, doi:10.1103/PhysRevB.71.165202.

Street, R., W. Wong, S. Ready, M. Chabinyc, a. Arias, S. Limb, a. Salleo, and R. Lujan (2006), Jet printing flexible displays, *Materials Today*, *9*(4), 32–37, doi:10.1016/S1369-7021(06)71445-6.

Sundar, V. C., J. Zaumseil, V. Podzorov, E. Menard, R. L. Willett, T. Someya, M. E. Gershenson, and J. a. Rogers (2004), Elastomeric transistor stamps: reversible probing of charge transport in organic crystals., *Science (New York, N.Y.)*, *303*(5664), 1644–6, doi:10.1126/science.1094196.

Swiggers, M. L., G. Xia, J. D. Slinker, a. a. Gorodetsky, G. G. Malliaras, R. L. Headrick, B. T. Weslowski, R. N. Shashidhar, and C. S. Dulcey (2001), Orientation of pentacene films using surface alignment layers and its influence on thin-film transistor characteristics, *Applied Physics Letters*, *79*(9), 1300, doi:10.1063/1.1394952.

van Breemen, A. J. J. M., et al. (2006), Large area liquid crystal monodomain field-effect transistors., *Journal of the American Chemical Society*, *128*(7), 2336–45, doi:10.1021/ja055337l.

Virkar, A. a., S. Mannsfeld, Z. Bao, and N. Stingelin (2010), Organic semiconductor growth and morphology considerations for organic thin-film transistors., *Advanced materials (Deerfield Beach, Fla.)*, *22*(34), 3857–75, doi:10.1002/adma.200903193.

Voigt-Martin, I. G., and H. Durst (1989), High-resolution images of defects in liquid crystalline polymers in the smectic and crystalline phases, *Macromolecules*, *22*(1), 168–173, doi:10.1021/ma00191a033.

Voss, D. (2000), Cheap and cheerful circuits, *NATURE*, *407*(6803), 442–444.

Wallace, G. G., T. E. Campbell, and P. C. Innis (2007), Putting Function into Fashion: Organic Conducting Polymer Fibres and Textiles, *Fibers and Polymers*, *8*(2), 135–142.

Waragai, K., H. Akimichi, S. Hotta, and H. Kano (1995), Charge Transport in Thin Films of Semiconducting Oligothiophenes, *Physical Review B*, *52*(3).

Wiegeleben, A., and D. Demus (1988), METHODICAL ASPECTS IN THERMAL ANALYSIS OF LIQUID CRYSTALLINE SUBSTANCES, *Journal of Therma Analysis*, *33*, 1207–1211.

Williams, D. B., and C. B. Carter (1996), *Transmission Electron Microscopy: A Textbook for Materials Science*, 703 pp., Springer Science.

Xiao, K., et al. (2005), A highly pi-stacked organic semiconductor for field-effect transistors based on linearly condensed pentathienoacene., *Journal of the American Chemical Society*, *127*(38), 13,281–6, doi:10.1021/ja052816b.

Yamada, M., I. Ikemoto, and H. Kuroda (1988), Photooxidation of the Evaporated Films of Polycyclic Aromatic Hydrocarbons Studied By X-Ray Photoelectron Spectroscopy, *Bull. Chem. Soc. Japan.*, *61*, 1057—-1062.

Yang, C., F. P. Orfino, and S. Holdcroft (1996), A Phenomenological Model for Predicting Thermochromism of Regioregular and Nonregioregular Poly(3-alkylthiophenes), *Macromolecules*, *29*(20), 6510–6517, doi:10.1021/ma9604799.

Yazawa, K., Y. Inoue, T. Yamamoto, and N. Asakawa (2006), Twist glass transition in regioregulated poly(3-alkylthiophene), *Physical Review B*, *74*(9), 1–12, doi:10.1103/PhysRevB.74.094204.

Young, R. J., and P. A. Lovell (1991), *Introduction to Polymers*, 2nd ed., 443 pp., Chapman and Hall, London.

Yuan, G. C., et al. (2009), High performance organic thin film transistor with phenyltrimethoxysilane-modified dielectrics, *Applied Physics Letters*, *94*(15), 153,308, doi:10.1063/1.3115828.

Zhang, B. X., S. D. Hudson, D. M. Delongchamp, D. J. Gundlach, and I. Mcculloch (2010), In-plane Liquid Crystalline Texture of High Performance Thienothiophene Copolymer Thin Films, *Advanced Functional Materials*, *20*, 4098–4106, doi:10.1002/adfm.)).

Zhang, X. (2006), Fused-Ring Poly- and Oligothiophenes: Designed Electronic Materials, Ph.D. thesis, University of Michigan.

Zhang, X. (2011), Unpublished work.

Zhang, X., A. P. Côté, and A. J. Matzger (2005), Synthesis and structure of fused alpha-oligothiophenes with up to seven rings., *Journal of the American Chemical Society*, *127*(30), 10,502–3, doi:10.1021/ja053326m.

Zhang, X., J. P. Johnson, J. W. Kampf, and A. J. Matzger (2006), Ring Fusion Effects on the Solid-State Properties of α-Oligothiophenes, *Chemistry of Materials*, *18*(15), 3470–3476, doi:10.1021/cm0609348.

Zheng, Z., K.-H. Yim, M. S. M. Saifullah, M. E. Welland, R. H. Friend, J.-S. Kim, and W. T. S. Huck (2007), Uniaxial alignment of liquid-crystalline conjugated polymers by nanoconfinement., *Nano letters*, *7*(4), 987–92, doi:10.1021/nl070022k.